NASA/TP—2002-210783

The Statistical Mechanics of Ideal Homogeneous Turbulence

John V. Shevalin
NASA Johnson Space Center
Houston, Texas

May 2002

The NASA STI Program Office . . . in Profile

Since its founding, NASA has been dedicated to the advancement of aeronautics and space science. The NASA Scientific and Technical Information (STI) Program Office plays a key part in helping NASA maintain this important role.

The NASA STI Program Office is operated by Langley Research Center, the lead center for NASA's scientific and technical information. The NASA STI Program Office provides access to the NASA STI Database, the largest collection of aeronautical and space science STI in the world. The Program Office is also NASA's institutional mechanism for disseminating the results of its research and development activities. These results are published by NASA in the NASA STI Report Series, which includes the following report types:

- TECHNICAL PUBLICATION. Reports of completed research or a major significant phase of research that present the results of NASA programs and include extensive data or theoretical analysis. Includes compilations of significant scientific and technical data and information deemed to be of continuing reference value. NASA's counterpart of peer-reviewed formal professional papers but has less stringent limitations on manuscript length and extent of graphic presentations.

- TECHNICAL MEMORANDUM. Scientific and technical findings that are preliminary or of specialized interest, e.g., quick release reports, working papers, and bibliographies that contain minimal annotation. Does not contain extensive analysis.

- CONTRACTOR REPORT. Scientific and technical findings by NASA-sponsored contractors and grantees.

- CONFERENCE PUBLICATION. Collected papers from scientific and technical conferences, symposia, seminars, or other meetings sponsored or cosponsored by NASA.

- SPECIAL PUBLICATION. Scientific, technical, or historical information from NASA programs, projects, and mission, often concerned with subjects having substantial public interest.

- TECHNICAL TRANSLATION. English-language translations of foreign scientific and technical material pertinent to NASA's mission.

Specialized services that complement the STI Program Office's diverse offerings include creating custom thesauri, building customized databases, organizing and publishing research results . . . even providing videos.

For more information about the NASA STI Program Office, see the following:

- Access the NASA STI Program Home Page at ***http://www.sti.nasa.gov***

- E-mail your question via the Internet to help@sti.nasa.gov

- Fax your question to the NASA Access Help Desk at (301) 621-0134

- Telephone the NASA Access Help Desk at (301) 621-0390

- Write to:
  NASA Access Help Desk
  NASA Center for AeroSpace Information
  7121 Standard
  Hanover, MD 21076-1320

NASA/TP—2002-210783

The Statistical Mechanics of Ideal Homogeneous Turbulence

John V. Shebalin
NASA Johnson Space Center
Houston, Texas

National Aeronautics and
Space Administration

Johnson Space Center
Houston, Texas 77058-3696

May 2002

Available from:

NASA Center for AeroSpace Information
7121 Standard
Hanover, MD 21076-1320

National Technical Information Service
5285 Port Royal Road
Springfield, VA 22161

This report is also available in electronic form at http://techreports.larc.nasa.gov/cgi-bin/NTRS

PREFACE

As far as the laws of mathematics refer to reality, they are not certain; and as far as they are certain, they do not refer to reality. – A. Einstein

Plasmas, such as those found in the space environment or in fusion energy devices, are often modeled as electrically conducting fluids. Fluids, and thus plasmas, when energetically stirred, have regions of highly nonlinear, chaotic behavior known as turbulence. Although turbulence in fluids and plasmas is often the critical factor in determining overall long-term behavior, a general theory of turbulence has been elusive. Establishing such a general theory is a 'grand challenge' to modern science.

The present work describes a statistical theory concerning a certain class of nonlinear, finite dimensional, dynamical models of turbulence. These models arise when the partial differential equations describing incompressible, ideal (*i.e.*, non-dissipative) homogeneous fluid and magnetofluid (*i.e.*, plasma) turbulence are Fourier transformed into a very large set of ordinary differential equations. These equations define a divergenceless flow in a high-dimensional phase space, which allows for the existence of a Liouville theorem, guaranteeing a distribution function based on constants of the motion (integral invariants). The novelty of these particular dynamical systems is that there are integral invariants other than the energy, and that some of these invariants behave like pseudoscalars under two of the discrete symmetry transformations of physics, parity and charge conjugation.

In this work, we show that the 'rugged invariants' of ideal homogeneous turbulence are, in fact, the only significant scalar and pseudoscalar invariants. Furthermore, we show that the existence of pseudoscalar invariants causes the symmetry of the original equations to be dynamically broken, inducing a nonergodic structure on the associated phase space. Although realistic turbulence is non-ideal, it also has no existing viable statistical or kinetic theory to describe it. In lieu of this, and perhaps as a remote precursor, what is presented here is the complement: a statistical mechanics of ideal homogeneous turbulence. This, in turn, may bring us closer to meeting the 'grand challenge.'

This work began two decades ago, when the author noticed that canonical ensemble predictions did not match the results of numerical experiments by a small but significant amount. Following this lead, an interesting story unfolded, leading to an understanding of what caused the initial mismatch, and the development of the statistical mechanics of an intriguing class of conservative, nonlinear dynamical systems. What is presented here is not

an extension of chaos theory, which deals with motion in low-dimensional phase spaces, but rather a statistical theory of conservative dynamical systems with relatively large, but finite, dimensional phase spaces.

A note on references: The references given here are mainly the ones that have been useful to the author in his research. No attempt has been made to be thorough in the citing of references that might be concerned with the general topic of ideal homogeneous turbulence. History shows us that many people work in parallel on any given research topic, and that essentially identical results are often independently produced. However, the modern age has the advantage of electronic search and communication systems, and in using these, the author has found no similar work addressing the central subjects presented herein: Broken symmetry and nonergodicty in ideal homogeneous turbulence.

I would like to thank David Montgomery for introducing me to this subject. I thank Robert Rubinstein for his review of this document and for catching some errors. Of course, any errors that remain are mine alone. (I would appreciate being informed of any errors, either typographical or conceptual.) Finally, I would like to thank all the other individuals and institutions that have helped support this work over the past two decades.

John V. Shebalin

j.shebalin@jsc.nasa.gov

Advanced Space Propulsion Laboratory
National Aeronautics & Space Administration
Lyndon B. Johnson Space Center
Houston, Texas 77058

Contents

List of Tables

List of Figures

Chapter 1

The Problem of Turbulence

1.1 Introduction

Turbulence in fluids appears to be a ubiquitous phenomenon, occurring in astrophysical, geophysical, and engineering flows. The historical course of fluid analysis, however, was to initially concentrate on the examination of laminar flow problems, as exact solutions were often possible. This allowed fluid dynamicists and mathematicians to gain analytical practice by using tools established in other fields, such as potential and complex variable theory, and to build a base from which to gain further understanding of the more complicated motions of fluids. Although this practice was useful and necessary, observation of real fluids indicates that there are often regions where the flow seems convoluted, unsteady, and prone to apparent randomness, involving the generation of fluctuating structures termed 'eddies' whose instantaneous sizes vary over a wide range.

As the energy being input into a fluid increases, there is typically a transition from laminar to turbulent flow, and this occurrence can be analyzed by assuming that a small perturbation to laminar flow occurs, linearizing the relevant equations in terms of this small perturbation, and studying its subsequent growth. This step produced and still produces valuable insights into fluid and magnetofluid mechanics and establishes a bridge between laminar and turbulent flow. In the past, it also allowed research to proceed, as the study of fluids could still be approached analytically, with quill and parchment, as it were, in the era before the widespread availability of high-speed electronic computing machines.

Turbulence, the final step and most general state of an energetic fluid, has proved, however, to be far more resilient to detailed mathematical analysis than the preceding two steps. Even with the advent of modern computing, a full and detailed study is still difficult, if not currently impossible, due to the extremely large number of degrees of freedom in any realistic turbulent flow, in comparison to the capacity of either available or envisioned computers to simulate fluid motion. Computers with their limited memories can only capture an exceedingly small fraction of the degrees of freedom inherent in a fully turbulent, 'high Reynolds number' flow. To move beyond this impasse, various analytical theories of turbulence have been put forward, based on intelligent guesswork. The most successful of these is the rela-

tively simple dimensional analysis of Kolmogorov, leading to the famed energy spectral index of -5/3 for the so-called inertial range. Other, more detailed, analytical theories have been built on seemingly logical hypotheses, coupled with perturbation techniques, but have not been generally successful.

Turbulence in the physical universe is found in the flow of ionized gases (*i.e.*, plasmas viewed as magnetofluids) within the sun, the solar wind, and planetary magnetospheres, as well as in the fluids found in planetary atmospheres and oceans, and in the myriad engineering systems devised by human ingenuity. Turbulence is a flow of energy, from its injection at relatively large scales, to its transfer through an inertial range, to its dissipation at relatively small scales. This may be thought of as a transfer of energy from larger eddies to smaller eddies to smaller ones still, until, at the end of the cascade, flow energy becomes simply molecular heat. The challenge is to discover a 'law of turbulence' that describes the details of this energy transfer. This challenge continues to await the intrepid explorer, who may need to invent new theories and mathematical techniques, perhaps building on what is known, perhaps making a radical departure.

The main characteristic of turbulence is that it is a non-equilibrium dynamical process in which energy is ultimately dissipated. If energy input is abated at some point, the phenomenon becomes 'decaying turbulence,' and if energy is continually injected into the flow, it may be called 'driven turbulence.' Realistically, turbulence contains a dissipation mechanism, which, for fluids, is provided by viscosity, and for plasmas, by electrical resistivity as well as viscosity. Once heat is produced, thermal conductivity also comes into play, and will be important if compressibility is a factor in the dynamics of the fluid. However, since density variation is often not a critical factor in turbulent flow, particularly for those of low Mach number, then assuming at the outset that turbulent flows are incompressible leads to a simpler set of basic equations, while still retaining the essential nonlinear interactions which cause turbulence. This approximation will be adopted here.

Although turbulence involves a large number of interacting degrees of freedom, which suggests that statistical mechanics be applied, the presence of dissipation, and the transfer of energy generally towards the smaller length scales, requires instead that something like kinetic theory be used. Thus, many analytical theories of turbulence have at their heart a hierarchy of integral equations, which have been treated by expansions similar to those found in quantum field theory, so that such approaches are often called 'field-theoretic.' In contrast, classical statistical mechanics has conservative systems in equilibrium as its domain of applicability, or at least systems that can be approximated in such a way. In the real world, it is not possible to turn dissipation off in an astrophysical or geophysical fluid (although this does occur in one component of a superfluid). In the world of analytical and computational models, however, it is possible to set viscosity and resistivity identically equal to zero. Mathematically, this is an example of a *singular perturbation problem* - setting a small parameter multiplying the highest derivative in an equation equal to zero changes the fundamental nature of the equation and its solutions. Although this may have its uses, it must be remembered that this introduces a layer of approximation that formally disconnects real and ideal turbulence.

1.2 Ideal Flow

Neglecting dissipation creates the mathematical entities called ideal fluids and ideal magnetofluids. The advantage gained is that standard equilibrium statistical mechanics can be applied (as will be shown), albeit only to model systems. Furthermore, if the flow volume of interest is far removed from bounding surfaces, then statistical characteristics can be assumed independent of spatial position. Such (real or ideal) turbulence is termed *homogeneous*, and is often also *isotropic*, unless there is some mechanism imposing a preferred direction on the system, such as a constant magnetic field in a magnetofluid, in which case it may be *anisotropic*. Ideal turbulent systems are purely mathematical entities whose governing equations contain nonlinear terms identical to those found in the equations of real turbulence. Ideal equations lack only the linear dissipative term found in real equations, and though this may seem a negligible difference, it is not – it is an essential difference. Nevertheless, ideal turbulence has its own attraction and the search for ideal statistical solutions has an instructive purpose.

Since either real or ideal turbulence is highly nonlinear, exact analytical solutions do not exist and numerical techniques must be utilized to integrate the equations of motion. This introduces further approximation, as computers are finite machines, so that round-off errors and finite time-integration steps provide another layer between physical reality and computational results. Here, we will use finite Fourier expansions to represent spatial variation, which has the benefit of allowing for the exact evaluation of spatial derivatives, albeit only down to some minimum wavelength. Although computer models can approximate turbulent systems, it must be remembered that their efficacy in representing either real or ideal turbulent flows is determined only to the extent that they match physical observations in the case of real flows, or some independent statistical theory in the case of ideal flows.

The purpose of the present work is to develop the statistical mechanics of ideal homogeneous, incompressible, fluid and magnetofluid turbulence. It will turn out that this statistical mechanics is an interesting and non-trivial extension of standard canonical ensemble theory, due to the presence of significant invariant integrals of the motion, in addition to the energy. Some of these additional invariant integrals are pseudoscalars under various symmetry transformations of the equations of motion, and this will lead to what has been called *broken ergodicity*. The systems to which this statistical theory is applied are computer models of ideal turbulence, and these computer models allow us to run numerical experiments. Since these models are highly nonlinear, we do not know in advance, nor can we predict, any precise details of the flow, which is highly stochastic. Instead, we can make predictions of ideal statistical behavior and compare these with time averages determined through numerical integration, thereby testing the statistical theory.

The development of a statistical theory for ideal turbulence is expedited by the fact that the various integral invariants can be expressed as expectation values of quadratic forms, which leads to *Gaussian* distribution functions in the phase spaces under consideration, thus allowing a relatively straightforward evaluation of expectation values. Since all fundamental interactions in nature are describable by nonlinear partial differential equations, the theory

developed here has obvious analogies in other areas of physics and applied mathematics where dissipation is either not present or can be ignored. (However, in these other areas, the integral invariants are related to forms that may not be quadratic, leading to non-Gaussian distribution functions that make expectation values more difficult to evaluate.) Finally, there is a remote theoretical possibility that ideal results might be extended into a non-ideal domain, and this will be briefly discussed, following the primary item of interest: the development of a statistical theory for ideal turbulence.

1.3 References for Further Reading

A classic text on turbulence is [Batchelor 53].

A more modern text that gives a good overview and critique of the current status of turbulence research is [Frisch 95].

Analytical theories, although they do not provide a solution to the 'problem of turbulence,' indicate the inherent difficulty of this problem by showing the forests of complication into which researchers have been forced to enter. A detailed discussion of these theories, following a good preliminary overview of the basics of turbulence, is found in [McComb 95].

Chapter 2

The Equations of Motion

First, we will establish the basic equations of fluids and magnetofluids, and then reduce them to those needed for the study of incompressible ideal homogeneous turbulence. We begin by assuming that a continuous, electrically conducting fluid exists, although it is possible to start from an underlying set of discrete particles, and use kinetic theory to derive a single fluid continuum approximation. In the physics of plasmas, this is a common procedure, and moves the perspective from microscopic kinetics to macroscopic continua. In the continuum approximation, characteristic length scales are much greater than inter-particle distances, and charge separation and associated quasi-static electric fields are assumed to be dynamically unimportant. However, electrical conductivity is generally still present, so that magnetic fields may arise due to self-induced or externally imposed electrical currents. The study of such fluids is often termed *magnetohydrodynamics* (MHD) or *magnetofluid mechanics*, and it contains, as a subset, (nonconducting) fluid mechanics.

The state of a magnetofluid in a given volume V and interval of time T is completely specified if its density ρ, velocity $\mathbf{u}$, magnetic field $\mathbf{B}$, and pressure p are known at all points $\mathbf{x}$ of the volume V at all times t within the interval T. Thus, density, velocity, magnetic field, and pressure are generally functions of $\mathbf{x}$ and t, and may be denoted by $\rho(\mathbf{x},t)$, $\mathbf{u}(\mathbf{x},t)$, $\mathbf{B}(\mathbf{x},t)$, and $p(\mathbf{x},t)$, respectively. (However, in what follows, one or both of the arguments $\mathbf{x}$ and t may be omitted for brevity.) There are, of course, other assumptions that can be made, resulting in various levels of complexity. For our purpose, the stated assumptions, along with incompressibility, will suffice, and the resulting system of equations will be sufficiently challenging.

2.1 The Continuity Equation

Consider now a small volume δV within the fluid. If the bounding surface of δV moves with the fluid, then the mass $\delta m = \rho \delta V$ within δV is constant:

$$\frac{d\delta m}{dt} = \rho \frac{d\delta V}{dt} + \delta V \frac{d\rho}{dt} = 0. \tag{2.1}$$

Now, assume that δV is an infinitesimal cube, which can be represented in Cartesian coordinates as $\delta V = \delta x \delta y \delta z$, where $\delta x = x_2 - x_1$, etc. Neglecting terms of higher order than δx, we have, using $\dot{x} = dx/dt = u_x$,

$$\frac{d\delta x}{dt} = \dot{x}_2 - \dot{x}_1 = \frac{\partial u_x}{\partial x}\delta x. \tag{2.2}$$

Since analogous results hold for δy and δz, we have

$$\begin{aligned} \frac{d\delta V}{dt} &= \delta y \delta z \frac{d\delta x}{dt} + \delta x \delta z \frac{d\delta y}{dt} + \delta x \delta y \frac{d\delta z}{dt} \\ &= \delta x \delta y \delta z \left(\frac{\partial u_x}{\partial x} + \frac{\partial u_y}{\partial y} + \frac{\partial u_z}{\partial z} \right) \\ &= \delta V \nabla \cdot \mathbf{u}. \end{aligned} \tag{2.3}$$

Combining (2.1) with (2.3) gives

$$\delta V \left(\frac{d\rho}{dt} + \rho \nabla \cdot \mathbf{u} \right) = 0. \tag{2.4}$$

Here, we use the chain rule of differentiation to expand the total time derivative into partial derivatives with respect to position and time:

$$\begin{aligned} \frac{d\rho}{dt} &= \frac{\partial \rho}{\partial t} + \frac{dx}{dt}\frac{\partial \rho}{\partial x} + \frac{dy}{dt}\frac{\partial \rho}{\partial y} + \frac{dz}{dt}\frac{\partial \rho}{\partial z} \\ &= \frac{\partial \rho}{\partial t} + \mathbf{u} \cdot \nabla \rho. \end{aligned} \tag{2.5}$$

Since ρ in (2.5) can represent any scalar function or component of a vector function, the *convective derivative* can be generally defined as

$$\frac{d}{dt} \equiv \frac{\partial}{\partial t} + \mathbf{u} \cdot \nabla. \tag{2.6}$$

Note that the total time derivative refers to the changes occurring in a fluid element as we follow it in its motion, and when it is used explicitly in the equations of motion, such a formulation is called *Lagrangian* fluid mechanics. In Lagrangian fluid mechanics, an individual velocity is attached to each fluid element as it moves about. Alternatively, if (2.6) is used to convert all total time-derivatives to partial differential form, then we have *Eulerian* fluid mechanics, in which we focus on the behavior of a fluid as it moves past fixed points of space. In Eulerian fluid mechanics, velocity is a field that has values identified with points in space, rather than to individual particles of fluid. In Lagrangian fluid mechanics, one may consider the small volume δV as being attached to the fluid element, while in the Eulerian view, the small volume δV is associated with a fixed location in space, and fluid elements move

through it. It is this latter viewpoint that is most common and will be generally adopted here (although the Lagrangian viewpoint has its occasional uses).

Finally, after combining (2.4) (omitting the non-zero factor δV) with (2.5), we get the *continuity equation*:

$$\frac{\partial \rho}{\partial t} + \nabla \cdot (\rho \mathbf{u}) = 0. \tag{2.7}$$

This is the first of the basic equations of fluid mechanics, and defines how density is related to velocity in a compressible fluid.

Here, however, we wish to consider *incompressible* flow. In this case, the density $\rho =$ constant, and (2.7) becomes

$$\nabla \cdot \mathbf{u} = 0. \tag{2.8}$$

If (2.8) holds, the velocity field $\mathbf{u}$ is often said to be *solenoidal*, drawing on magnetic terminology.

2.2 The Navier-Stokes Equation

The next basic equation determines the evolution of fluid momentum density. The momentum of an infinitesimal fluid element, of mass $\delta m = \rho \delta V =$ constant, is $\mathbf{p} = \delta m \mathbf{u}$. Applying Newton's second law, the time rate of change of $\mathbf{p}$ is due to whatever forces $\mathbf{F}$ are imposed: $d\mathbf{p}/dt = \mathbf{F}$. Upon using (2.6), this becomes

$$\rho \delta V \left(\frac{\partial \mathbf{u}}{\partial t} + \mathbf{u} \cdot \nabla \mathbf{u} \right) = \mathbf{F}. \tag{2.9}$$

Now, the various forces that make up $\mathbf{F}$, and thereby affect fluid motion, must be determined.

First, there is the *pressure* p in the fluid, which is a force per unit area applied to the six faces of the cube of volume $\delta V = \delta x \delta y \delta z$, and the difference in pressure between opposing faces will give the net force due to pressure in the direction normal to those faces. For example, let the two faces with area $\delta y \delta z$ and normal along the x-direction have x-coordinates x and $x + \delta x$. The component of force in the x-direction due to pressure points from high to low pressure; this has the limiting form:

$$\begin{aligned} F_{p,x} &= \lim_{\delta x \to 0} -\left[p\left(x + \delta x\right) - p\left(x\right) \right] \delta y \delta z \\ &= -\frac{\partial p}{\partial x} \delta V. \end{aligned} \tag{2.10}$$

The components of the pressure force along the y- and z-directions, $F_{p,y}$ and $F_{p,z}$, respectively, can be determined in a similar manner. Thus, the total force on δV due to pressure is

$$\mathbf{F}_p = -\nabla p \ \delta V. \tag{2.11}$$

The pressure p is an example of a *stress* on the surfaces of a fluid element, whose (negative) gradient produces a net force.

Another force may arise due to *shear stresses*, which are also forces per unit area and which occur when neighboring fluid elements move at different velocities. This may be thought of as a frictional force between the surfaces of adjoining faces of fluid volumes. Consider a cubical fluid volume δV centered at $\mathbf{x} = (x, y, z)$ and an adjoining one δV_1 of the same volume centered at $\mathbf{x}' = (x + \delta x, y, z)$. The shear stress $\boldsymbol{\sigma}_x$ is proportional to the velocity difference between $\mathbf{x}'$ and $\mathbf{x}$ (the shear) divided by the distance δx, with a proportionality constant μ (the *dynamic viscosity*):

$$\boldsymbol{\sigma}_x(\mathbf{x}_1) \;=\; \lim_{\delta x \to 0} \mu \frac{\mathbf{u}(\mathbf{x}') - \mathbf{u}(\mathbf{x})}{\delta x} \;=\; \mu \frac{\partial \mathbf{u}}{\partial x}. \tag{2.12}$$

The shear stress can be visualized as manifesting itself on the surface between δV and δV_1, such that a force acts at the position $\mathbf{x}_1 = (x + \delta x/2, y, z)$. Similarly, consider another volume δV_2 located at $\mathbf{x}'' = (x - \delta x, y, z)$; by changing $+\delta x$ to $-\delta x$ in (2.12), and defining $\mathbf{x}_2 = (x - \delta x/2, y, z)$, we have

$$\boldsymbol{\sigma}_x(\mathbf{x}_2) \;=\; \lim_{\delta x \to 0} \mu \frac{\mathbf{u}(\mathbf{x}'') - \mathbf{u}(\mathbf{x})}{\delta x} \;=\; -\mu \frac{\partial \mathbf{u}}{\partial x}. \tag{2.13}$$

The net shear force $\mathbf{F}_{s,x}$ acting on the x-directed faces (of area $\delta y \delta z$) of the fluid volume δV, is

$$\begin{aligned} \mathbf{F}_{s,x}(\mathbf{x}) &= \lim_{\delta x \to 0} \left[\boldsymbol{\sigma}_x(\mathbf{x}_1) + \boldsymbol{\sigma}_x(\mathbf{x}_2) \right] \delta y \delta z \\ &= \frac{\partial \boldsymbol{\sigma}_x}{\partial x} \, \delta x \delta y \delta z \\ &= \frac{\partial}{\partial x} \left(\mu \frac{\partial \mathbf{u}}{\partial x} \right) \delta V. \end{aligned} \tag{2.14}$$

Although μ may, in general, be a function of position, here we will assume $\mu =$ constant. In this case,

$$\mathbf{F}_{s,x}(\mathbf{x}) \;=\; \mu \frac{\partial^2 \mathbf{u}}{\partial x^2} \, \delta V. \tag{2.15}$$

Since the procedure for finding $\mathbf{F}_{s,x}$ can similarly be applied to find the shear forces $\mathbf{F}_{s,y}$ and $\mathbf{F}_{s,z}$ due to viscous stresses acting on the faces of δV normal to the y- and z-directions, we see immediately from (2.15) that $x \to y$ produces $\mathbf{F}_{s,y}$ and $x \to z$ produces $\mathbf{F}_{s,z}$. Adding all these shear forces together yields the total force $\mathbf{F}_s$ due to viscous shear on a fluid element δm:

$$\mathbf{F}_s \;=\; \mathbf{F}_{s,x} + \mathbf{F}_{s,y} + \mathbf{F}_{s,z} \;=\; \mu \nabla^2 \mathbf{u} \; \delta V. \tag{2.16}$$

Thus we have found the second of two forces that act on the surfaces of an incompressible fluid element, and thereby affect its motion.

Putting (2.11) and (2.16) into (2.9), we arrive at the *Navier-Stokes equation*:

$$\rho\left(\frac{\partial \mathbf{u}}{\partial t} + \mathbf{u}\cdot\nabla\mathbf{u}\right) = -\nabla p + \mu\nabla^2\mathbf{u} + \mathbf{f}. \tag{2.17}$$

Here $\mathbf{f}$ denotes any additional force densities related to body forces $\mathbf{F} = \mathbf{f}\delta V$ that may be acting on a fluid element. In classical physics, the only available candidates for $\mathbf{F}$ are gravitational or electromagnetic forces. Gravity is only important when compressibility is, so it is not of concern here. The electromagnetic force is important in a magnetofluid, and is due to the presence of electrical currents and magnetic fields. It will be discussed presently.

The pressure p appears to be a new independent fluid variable in (2.17), and would require another time-evolution equation to describe it, if the fluid were compressible. However, for incompressible flow, p can be determined by taking the divergence of (2.17), using (2.8) to produce

$$\nabla^2 p = \nabla\cdot\left(\mathbf{f} - \rho\mathbf{u}\cdot\nabla\mathbf{u}\right). \tag{2.18}$$

Thus, p is found for incompressible flow by solving the Poisson equation (2.18), which depends only on the instantaneous values of $\mathbf{f}$ and $\mathbf{u}$ (since ρ is constant).

As Helmholz's theorem tells us, a vector field is determined by its divergence, curl and boundary values, and we can apply this to further define the equations for $\mathbf{u}$. Here, periodic boundary conditions will be in effect, and the divergence of $\mathbf{u}$ is zero, by (2.8), so what remains is to find an equation for the curl of $\mathbf{u}$, which is called the *vorticity*: $\boldsymbol{\omega} = \nabla\times\mathbf{u}$. Taking the curl of (2.17), and using some well known vector identities, produces the *vorticity equation*:

$$\frac{\partial \boldsymbol{\omega}}{\partial t} = \nabla\times\left(\mathbf{u}\times\boldsymbol{\omega} + \frac{\mathbf{f}}{\rho}\right) + \nu\nabla^2\boldsymbol{\omega}. \tag{2.19}$$

Here, the *kinematic viscosity* is $\nu = \mu/\rho$ and is also a constant. Electromagnetic forces are represented through the introduction of the appropriate $\mathbf{f}$ in (2.19), which is our next topic.

2.3 Magnetohydrodynamics

When a fluid is able to conduct electricity, the subject of fluid mechanics expands into what is known as MHD or magnetofluid dynamics. Since electromagnetism is now included, perhaps a good place to start a discussion is with *Maxwell's equations*, the governing equations of all electric fields $\mathbf{E}$ and magnetic fields $\mathbf{B}$. In SI units, and in free space, these equations are

$$\nabla\cdot\mathbf{B} = 0 \tag{2.20}$$

$$\nabla \cdot \mathbf{E} = \frac{\rho_e}{\epsilon_o} \tag{2.21}$$

$$\nabla \times \mathbf{B} = \mu_o \mathbf{j} + \frac{1}{c^2}\frac{\partial \mathbf{E}}{\partial t} \tag{2.22}$$

$$\nabla \times \mathbf{E} = -\frac{\partial \mathbf{B}}{\partial t}. \tag{2.23}$$

The constants ϵ_o and μ_o are the electric permittivity and magnetic permeability, respectively, of free space, while c is the speed of light, ρ_e is the electric charge density and $\mathbf{j}$ is the electric current density. The last term on the right side of (2.22), divided by μ_o, is called the *displacement current.*

For incompressible fluid mechanics, characteristic flow velocities U_o are small with respect to the speed of sound, and thus very small with respect to the speed of light c. If L_o is a characteristic length, and $T_o = L_o/U_o$ is a characteristic time, then (2.23) tells us that nominal magnitudes of $\mathbf{E}$ and $\mathbf{B}$ (call them E_o and B_o, respectively) are related by $E_o \sim B_o U_o$. Using this, the relative value of the last term on the right side of (2.22) is

$$\frac{|c^{-2}\,\partial \mathbf{E}/\partial t|}{|\nabla \times \mathbf{B}|} \sim \frac{U_o^2}{c^2}. \tag{2.24}$$

Thus, the term $c^{-2}\partial \mathbf{E}/\partial t$ is negligible compared to the other terms in (2.22). The equation (2.22) then reduces to a defining relation between current and field:

$$\mu_o \mathbf{j} = \nabla \times \mathbf{B}. \tag{2.25}$$

[As a historical aside, Maxwell generalized (2.22) from the known time-independent relationship (2.25), so that taking the divergence of (2.22) and using (2.21) would lead to a continuity equation for electric charge. This discovery of the 'displacement current' completed the mathematical foundations of electromagnetism, which were thereafter called, in his honor, *Maxwell's equations.*]

While (2.24) indicates that the time rate of change of $\mathbf{E}$ is negligible in MHD, this is not necessarily true for $\mathbf{E}$ itself. In fact, we can find an expression for $\mathbf{E}$, and through this, an expression for the charge density ρ_e. First, we can introduce a *vector potential* $\mathbf{A}$ because of (2.20):

$$\nabla \cdot \mathbf{B} = 0 \quad \rightarrow \quad \mathbf{B} = \nabla \times \mathbf{A}. \tag{2.26}$$

Here we may choose a condition (called a *gauge condition*) on the divergence of $\mathbf{A}$. We choose

$$\nabla \cdot \mathbf{A} = 0. \tag{2.27}$$

Second, we use (2.23) and (2.26) to introduce a *scalar potential* φ:

$$\nabla \times \mathbf{E} = -\frac{\partial \mathbf{B}}{\partial t} \quad \rightarrow \quad \nabla \times \left(\mathbf{E} + \frac{\partial \mathbf{A}}{\partial t}\right) = 0$$

$$\rightarrow \quad \mathbf{E} + \frac{\partial \mathbf{A}}{\partial t} = -\nabla \varphi. \tag{2.28}$$

The electric field $\mathbf{E}$ is therefore determined by φ and $\mathbf{A}$:

$$\mathbf{E} = -\nabla\varphi - \frac{\partial \mathbf{A}}{\partial t}. \tag{2.29}$$

Finally, taking the divergence of (2.29), then using (2.21) and (2.27), yields

$$\nabla \cdot \mathbf{E} = -\nabla^2\varphi = \frac{\rho_e}{\epsilon_o}. \tag{2.30}$$

To reiterate, although $\partial\mathbf{E}/\partial t$ is neglected in the MHD approximation, $\mathbf{E}$ and ρ_e are generally nonzero.

Now we determine the form of $\mathbf{E}$. Let the fields which are seen in the Lagrangian reference frame attached to a moving fluid element be denoted by $\mathbf{E}'$ and $\mathbf{B}'$, and the (Eulerian) fields as seen at fixed points of space by $\mathbf{E}$ and $\mathbf{B}$. These fields are connected by *Lorentz transformations* which, for the low velocities of interest here, become

$$\mathbf{E}' = \mathbf{E} + \mathbf{u} \times \mathbf{B} \quad \text{and} \quad \mathbf{B}' = \mathbf{B}. \tag{2.31}$$

In addition, the current $\mathbf{j}$ in the reference frame attached to a moving fluid element can be given by the simple Ohm's law: $\mathbf{j} = \sigma\mathbf{E}'$, where σ is the electrical conductivity of the fluid (which will be assumed constant here). Upon using (2.31), Ohm's law becomes

$$\mathbf{j} = \sigma(\mathbf{E} + \mathbf{u} \times \mathbf{B}). \tag{2.32}$$

Solving (2.32) for $\mathbf{E}$ and using (2.25) for $\mathbf{j}$ produces

$$\mathbf{E} = \eta\nabla \times \mathbf{B} - \mathbf{u} \times \mathbf{B}. \tag{2.33}$$

The constant η is the *resistivity*: $\eta = (\mu_o\sigma)^{-1}$. Combining (2.33) and (2.29) gives the evolution equation for the vector potential:

$$\frac{\partial \mathbf{A}}{\partial t} = -\nabla\varphi + \mathbf{u} \times \mathbf{B} - \eta\nabla \times \mathbf{B}. \tag{2.34}$$

Taking the divergence of (2.34), and using (2.27) and (2.30), gives the MHD expression for charge density:

$$\frac{\rho_e}{\epsilon_o} = -\nabla^2\varphi = -\nabla \cdot (\mathbf{u} \times \mathbf{B}). \tag{2.35}$$

Note that (2.35) and (2.18) are similar in the way they define electrostatic potential φ and static pressure p, respectively.

Putting (2.33) into (2.23), or equivalently, taking the curl of (2.34), gives the *magnetic field evolution equation*:

$$\frac{\partial \mathbf{B}}{\partial t} = \nabla \times (\mathbf{u} \times \mathbf{B}) + \eta\nabla^2\mathbf{B}. \tag{2.36}$$

Note that this equation for the magnetic field $\mathbf{B}$ has a similar structure to (2.19). Since $\mathbf{B}$ is the evolving quantity, and $\mathbf{j}$ is defined by (2.25), it is important to recognize that, in the *MHD approximation*, $\mathbf{B}$ determines $\mathbf{j}$, rather than the reverse, which occurs in the more general case when (2.22) must be used instead of (2.25).

The electromagnetic force density $\mathbf{f}$ appearing in (2.19) is

$$\mathbf{f} \;=\; \mathbf{j} \times \mathbf{B}. \tag{2.37}$$

Here, this will be called the *magnetic force density*. It is essentially the vector sum of the *Lorentz forces* $q\mathbf{v} \times \mathbf{B}$ acting on the individual particles of charge q and velocity $\mathbf{v}$ which collectively constitute the 'fluid' in δV. Placing (2.37) into (2.19) gives the *vorticity equation*:

$$\frac{\partial \boldsymbol{\omega}}{\partial t} \;=\; \nabla \times \left(\mathbf{u} \times \boldsymbol{\omega} + \frac{1}{\rho}\, \mathbf{j} \times \mathbf{B} \right) + \nu \nabla^2 \boldsymbol{\omega}. \tag{2.38}$$

There are two dissipation coefficients in (2.38) and (2.36): the viscosity ν and the resistivity η. If no energy is input into the magnetofluid, the presence of ν and η ensures that any initial energy will decay towards zero, as will be shown in the next chapter. First, let us look at the non-dimensional form of the equations of motion.

2.4 Non-dimensional Equations

The formal procedure for producing non-dimensional equations begins with the following assignments:

$$\mathbf{u} = U_{\mathrm{o}} \mathbf{u}', \qquad \mathbf{B} = B_{\mathrm{o}} \mathbf{B}', \qquad \mathbf{x} = L_{\mathrm{o}} \mathbf{x}', \qquad t = \frac{L_{\mathrm{o}}}{U_{\mathrm{o}}} t'. \tag{2.39}$$

Furthermore let $B_{\mathrm{o}} = \sqrt{\mu_{\mathrm{o}} \rho}\, U_{\mathrm{o}}$, which equates characteristic velocity U_{o} with the so-called *Alfvén velocity*, $U_A = B_{\mathrm{o}} / \sqrt{\mu_{\mathrm{o}} \rho}$. Placing (2.39) along with $\rho =$ constant into (2.38) and (2.36) yields

$$\frac{\partial \boldsymbol{\omega}'}{\partial t'} \;=\; \nabla' \times (\mathbf{u}' \times \boldsymbol{\omega}' + \mathbf{j}' \times \mathbf{B}') + \frac{1}{R_e} \nabla'^2 \boldsymbol{\omega}' \tag{2.40}$$

$$\frac{\partial \mathbf{B}'}{\partial t'} \;=\; \nabla' \times (\mathbf{u}' \times \mathbf{B}') + \frac{1}{R_M} \nabla'^2 \mathbf{B}'. \tag{2.41}$$

The *Reynolds number* R_e, *magnetic Reynolds number* R_M, and ∇' are

$$R_e \equiv \frac{U_{\mathrm{o}} L_{\mathrm{o}}}{\nu}, \qquad R_M \equiv \frac{U_{\mathrm{o}} L_{\mathrm{o}}}{\eta}, \qquad \nabla' \equiv \frac{\partial}{\partial \mathbf{x}'}. \tag{2.42}$$

The dimensionless numbers R_e and R_M characterize the magneto-flow, and any two systems, independent of relative physical size, with the same values of R_e and R_M are said to have *similar* flow.

We will always work with the equations in non-dimensional form. In this case, it is convenient to remove all the primes in (2.40) and (2.41), and also to set $R_e^{-1} = \nu$ and $R_M^{-1} = \eta$, for brevity, where ν and η are now dimensionless numbers. The result is a set of non-dimensional equations for the time development of the fields $\mathbf{u}$ and $\mathbf{B}$:

$$\frac{\partial \boldsymbol{\omega}}{\partial t} = \nabla \times (\mathbf{u} \times \boldsymbol{\omega} + \mathbf{j} \times \mathbf{B}) + \nu \nabla^2 \boldsymbol{\omega} \tag{2.43}$$

$$\frac{\partial \mathbf{B}}{\partial t} = \nabla \times (\mathbf{u} \times \mathbf{B}) + \eta \nabla^2 \mathbf{B}. \tag{2.44}$$

In addition to these, we also have the non-dimensional relations:

$$\nabla \cdot \mathbf{u} = 0, \qquad \boldsymbol{\omega} = \nabla \times \mathbf{u}$$

$$\nabla \cdot \mathbf{B} = 0, \qquad \mathbf{j} = \nabla \times \mathbf{B}. \tag{2.45}$$

The equations (2.43), (2.44), and (2.45) define the basic equations needed here. If we set $\eta = \nu = 0$, we obtain the equations of *ideal* magnetofluid turbulence. (The equations of simple fluid turbulence arise if we set $\mathbf{B} = 0$.)

Finally, boundary conditions remain to be specified. In general, if solid surfaces S with local normal $\hat{\mathbf{n}}$ are present, then $\hat{\mathbf{n}} \cdot \mathbf{u}|_S = 0$ for inviscid flow, while $\mathbf{u}|_S = 0$ for viscous flow. The magnetic boundary conditions depend on the conductivity and permeability of any surface, and also require specification. However, we need not go into boundary conditions any further, since we assume here and henceforth that any flow under consideration occurs in a periodic box. Periodic boundary conditions will be satisfied using spatial Fourier expansions of $\mathbf{u}$ and $\mathbf{B}$, as will be seen in the next chapter.

2.5 References for Further Reading

Perhaps the best all-round book on fluids (with separate chapters on ideal fluids and turbulence) is [Landau 87].

MHD is discussed by the same authors in [Landau 84, Chap. VIII].

A derivation of the MHD equations from the underlying plasma kinetic equation is found in [Nicholson 83].

Boundary conditions on electromagnetic fields are discussed in [Jackson 75].

Suggestions for references on the subject of turbulence have been given at the end of the previous chapter.

There are many more books that deal with various aspects of fluids, magnetofluids, and turbulence, as a library or net search will show. Some of these will be mentioned in the chapters ahead.

Finally, a good mathematical reference, on Helmholz's theorem, among other topics, is [Arfken 00].

Chapter 3

Fourier Representation

Here, it is assumed that the basic character of a given turbulent flow is invariant with respect to spatial translation; such flow is termed *homogeneous*. Our principle concern is with the behavior of the flow within an arbitrary region, far removed from any boundaries, somewhere in a large extent of fluid. In particular, we assume the large region can be divided into boxes and is periodic from one box to any adjoining ones. Alternatively, one can consider the flow as occurring in an unbounded but finite space called a *2-torus*, for 2-dimensional (2-D) flow, or a *3-torus*, for 3-dimensional (3-D) flow. In either case we have a finite area or volume of space whose points are defined by position vectors $\mathbf{x}$, where $\mathbf{x} = x\hat{\mathbf{x}} + y\hat{\mathbf{y}}$ for two dimensions, and $\mathbf{x} = x\hat{\mathbf{x}} + y\hat{\mathbf{y}} + z\hat{\mathbf{z}}$ for three dimensions ($\hat{\mathbf{x}}$, $\hat{\mathbf{y}}$, $\hat{\mathbf{z}}$ are unit vectors in the x, y, z directions, respectively). The components of $\mathbf{x}$ take on values mod(2π), so that their domains are $0 \le x < 2\pi$, $0 \le y < 2\pi$, and $0 \le z < 2\pi$, which are suitable for examining spatially periodic solutions of the non-dimensional equations of motion.

For brevity, we will set $x_1 = x$, $x_2 = y$, and $x_3 = z$, as well as $\hat{\mathbf{e}}_1 = \hat{\mathbf{x}}$, $\hat{\mathbf{e}}_2 = \hat{\mathbf{y}}$, and $\hat{\mathbf{e}}_3 = \hat{\mathbf{z}}$. Then we can write

$$\mathbf{x} = \sum_{i=1}^{D} x_i \, \hat{\mathbf{e}}_i . \tag{3.1}$$

Here, $D = 2$ or 3, signifying a vector in a 2-D or 3-D space, respectively. Also, $\mathbf{0} = (0, 0)$ or $(0, 0, 0)$, respectively, in 2-D or 3-D.

3.1 Discrete Fourier Transforms

Since there is periodicity in each spatial direction, we can represent the magnetofluid variables $\boldsymbol{\omega}$ and $\mathbf{B}$, assuming sufficient smoothness, in terms of discrete Fourier series. We begin by defining a finite set K_D^N of wave-vectors $\mathbf{k}$ (where I is the set of all integers):

$$\begin{aligned} \mathbf{k} &= \sum_{i=1}^{D} k_i \, \hat{\mathbf{e}}_i, \quad k_i \in I, \quad D = 2 \text{ or } 3 \\ K_D^N &\equiv \{\mathbf{k} \mid -N/2 \le k_j \le N/2, \; j = 1, \ldots, D\} . \end{aligned} \tag{3.2}$$

(Typically, N will be a power of 2: $N = 2^m$.)

Next, we define a finite set X_D^N of position vectors $\mathbf{x}$ with discrete coefficients $x_i = 2\pi n_i/N$:

$$\begin{aligned} \mathbf{x} &= \frac{2\pi}{N}\sum_{i=1}^{D} n_i\,\hat{\mathbf{e}}_i, \quad n_i \in I, \quad D = 2 \text{ or } 3 \\ X_D^N &\equiv \{\mathbf{x} \mid 0 \le n_j \le N-1,\ j = 1,\ldots,D\}\,. \end{aligned} \tag{3.3}$$

The sets X_D^N and K_D^N enable the definition of finite, discrete Fourier transformations:

$$\boldsymbol{\omega}(\mathbf{x}) = \sum_{\mathbf{k}\in K_D^N} \tilde{\boldsymbol{\omega}}(\mathbf{k})\, e^{i\mathbf{k}\cdot\mathbf{x}}, \quad \mathbf{x} \in X_D^N \tag{3.4}$$

$$\mathbf{B}(\mathbf{x}) = \sum_{\mathbf{k}\in K_D^N} \tilde{\mathbf{B}}(\mathbf{k})\, e^{i\mathbf{k}\cdot\mathbf{x}}, \quad \mathbf{x} \in X_D^N. \tag{3.5}$$

The inverse transformations are

$$\tilde{\boldsymbol{\omega}}(\mathbf{k}) = \frac{1}{N^3}\sum_{\mathbf{x}\in X_D^N} \boldsymbol{\omega}(\mathbf{x})\, e^{-i\mathbf{k}\cdot\mathbf{x}}, \quad \mathbf{k} \in K_D^N \tag{3.6}$$

$$\tilde{\mathbf{B}}(\mathbf{k}) = \frac{1}{N^3}\sum_{\mathbf{x}\in X_D^N} \mathbf{B}(\mathbf{x})\, e^{-i\mathbf{k}\cdot\mathbf{x}}, \quad \mathbf{k} \in K_D^N. \tag{3.7}$$

Relations (3.4) and (3.5) are said to transform the variables from *k-space* to *x-space*, and (3.6) and (3.7) reverse this transformation.

In the above, it will be noticed that the number of discrete x-space points $\mathbf{x} \in X_D^N$ is N^D, while the number of discrete k-space points $\mathbf{k} \in K_D^N$ appears to be $(N+1)^D$. However, from (3.6) and (3.7) (and suppressing explicit time-dependence for brevity), it is clear that

$$\tilde{\boldsymbol{\omega}}(\mathbf{k}_+^i) = \tilde{\boldsymbol{\omega}}(\mathbf{k}_-^i) \quad \text{and} \quad \tilde{\mathbf{B}}(\mathbf{k}_+^i) = \tilde{\mathbf{B}}(\mathbf{k}_-^i), \quad i = 1,\ldots,D \tag{3.8}$$

where the $\mathbf{k}_\pm^i$ are defined for $D = 3$ by

$$\mathbf{k}_\pm^1 = \pm\frac{N}{2}\hat{\mathbf{e}}_1 + k_2\hat{\mathbf{e}}_2 + k_3\hat{\mathbf{e}}_3 \tag{3.9}$$

$$\mathbf{k}_\pm^2 = k_1\hat{\mathbf{e}}_1 \pm \frac{N}{2}\hat{\mathbf{e}}_2 + k_3\hat{\mathbf{e}}_3 \tag{3.10}$$

$$\mathbf{k}_\pm^3 = k_1\hat{\mathbf{e}}_1 + k_2\hat{\mathbf{e}}_2 \pm \frac{N}{2}\hat{\mathbf{e}}_3. \tag{3.11}$$

For $D = 2$, we use only (3.9) and (3.10), with $k_3 = 0$.

Thus, due to (3.8) we have equivalent points $\mathbf{k}_+^i \sim \mathbf{k}_-^i,\ i = 1,\ldots,D$, in the set K_D^N, so that the number of independent points in k-space is decreased by one in each dimension. The total number of points needed for invertible Fourier transformation is therefore N^D in

both x-space and k-space. Note that (3.8) explicitly shows that the k-space representations of the magnetofluid variables, as well as those in x-space, are periodic.

Also, it is important to note that values of $\mathbf{x}$ other than those defined by (3.3) can be used in the Fourier transformations. Shifting all the $\mathbf{x} \in X_D^N$ by the same amount $\mathbf{x} \to \mathbf{x}+\boldsymbol{\delta}$ merely multiplies the complex Fourier coefficient associated with $\mathbf{k}$ by a factor $\alpha(\mathbf{k}) = \exp(i\mathbf{k}\cdot\boldsymbol{\delta})$, thereby changing the phase of the coefficient. Conversely, multiplying coefficients by $\alpha(\mathbf{k})$ allows the values of $\mathbf{x}$ not in X_D^N to be determined. Thus, a truncated discrete Fourier transformation is actually a *continuum* representation of a physical variable, although only to the level of resolution allowed by the discrete number of $\mathbf{k} \in K_D^N$. The $\mathbf{x} \in X_D^N$ may be viewed as a set of sampling points of the continuum, sufficient to reproduce the values at any point in the periodic space. The continuum nature of the representation also means that spatial derivatives can be evaluated exactly: $\nabla f(\mathbf{x}) \to i\mathbf{k}\,\tilde{f}(\mathbf{k})$. This makes numerical methods based on Fourier representations (whenever they can be applied) inherently more accurate than finite difference methods, which have no underlying continuum nature.

In k-space, (2.45) becomes

$$\begin{aligned} \mathbf{k}\cdot\tilde{\mathbf{u}}(\mathbf{k}) &= 0, \qquad \tilde{\boldsymbol{\omega}}(\mathbf{k}) = i\mathbf{k}\times\tilde{\mathbf{u}}(\mathbf{k}) \\ \mathbf{k}\cdot\tilde{\mathbf{B}}(\mathbf{k}) &= 0, \qquad \tilde{\mathbf{j}}(\mathbf{k}) = i\mathbf{k}\times\tilde{\mathbf{B}}(\mathbf{k}). \end{aligned} \tag{3.12}$$

Also, from the above, we may write

$$\tilde{\mathbf{u}}(\mathbf{k}) = ik^{-2}\mathbf{k}\times\tilde{\boldsymbol{\omega}}(\mathbf{k}) \quad \text{and} \quad \tilde{\mathbf{B}}(\mathbf{k}) = ik^{-2}\mathbf{k}\times\tilde{\mathbf{j}}(\mathbf{k}). \tag{3.13}$$

Obviously, $\mathbf{k}\cdot\tilde{\boldsymbol{\omega}}(\mathbf{k}) = 0$ and $\mathbf{k}\cdot\tilde{\mathbf{j}}(\mathbf{k}) = 0$, because of (3.12).

Next, we consider information content in the real-valued variables $\mathbf{u}(\mathbf{x})$ and $\mathbf{B}(\mathbf{x})$, and complex-valued variables $\tilde{\mathbf{u}}(\mathbf{k})$ and $\tilde{\mathbf{B}}(\mathbf{k})$. In 3-D x-space, there appear to be $6N^3$ real values (the 3 components of $\mathbf{u}$ and the 3 components of $\mathbf{B}$ at each discrete value of $\mathbf{x}$), while in 3-D k-space, there appear to be $12N^3$ real values (the 3 complex components of $\tilde{\mathbf{u}}$ and the 3 complex components of $\tilde{\mathbf{B}}$ at each discrete value of $\mathbf{k}$, taking (3.8) into account). Similarly, in 2-D x-space, there appear to be $4N^2$ real values (the 2 components of $\mathbf{u}$ and the 2 components of $\mathbf{B}$ at each discrete value of $\mathbf{x}$), while in 2-D k-space, there appear to be $8N^2$ real values (the 2 complex components of $\tilde{\mathbf{u}}$ and the 2 complex components of $\tilde{\mathbf{B}}$ at each discrete value of $\mathbf{k}$, again taking (3.8) into account). However, since $\mathbf{u}(\mathbf{x})$ [or equivalently, $\boldsymbol{\omega}(\mathbf{x})$] and $\mathbf{B}(\mathbf{x})$ are real-valued, it is evident from (3.6) and (3.7) that

$$\tilde{\boldsymbol{\omega}}^*(\mathbf{k}) = \tilde{\boldsymbol{\omega}}(-\mathbf{k}) \quad \text{and} \quad \tilde{\mathbf{B}}^*(\mathbf{k}) = \tilde{\mathbf{B}}(-\mathbf{k}). \tag{3.14}$$

This *reality condition* reduces the number of components (real and imaginary) which may be *independent* by half in 3-D k-space, to $6N^3$, which is commensurate with the $6N^3$ real components in 3-D x-space. Similarly, the number of components (real and imaginary) in 2-D k-space is also reduced by half, so that only $4N^2$ are independent, which is commensurate with the $4N^2$ real components in 2-D x-space. In fact, the relations (3.14) are used to minimize computer storage in subroutines which perform Fourier transformations of real

variables, so that (3.14) are (almost) explicitly enforced in any computer simulation of homogeneous turbulence that uses Fourier transforms. (Almost, because for a small number of $\mathbf{k}$, coefficients for $-\mathbf{k}$ are also utilized in Fast Fourier Transform, or FFT, subroutines.)

There are further reductions possible in information content, which are easier to see in k-space, than in x-space. First, a reduction is brought about by the solenoidal relations $\mathbf{k}\cdot\tilde{\mathbf{u}}(\mathbf{k})=0$ and $\mathbf{k}\cdot\tilde{\mathbf{B}}(\mathbf{k})=0$ in (3.12). These *solenoidality* conditions reduce the number of dynamically independent components of $\tilde{\mathbf{u}}(\mathbf{k})$ and $\tilde{\mathbf{B}}(\mathbf{k})$ by an additional factor of 2/3 for $D=3$ and by a factor of 1/2 for $D=2$. The 2-D vectors $\tilde{\mathbf{u}}(\mathbf{k})$ and $\tilde{\mathbf{B}}(\mathbf{k})$ can be represented by exactly one complex function each, thereby explicitly incorporating the 1/2 reduction, while in 3-D, the vectors $\tilde{\mathbf{u}}(\mathbf{k})$ and $\tilde{\mathbf{B}}(\mathbf{k})$ generally have three complex components each. However, these three complex components are kimematically linked by (3.12), so that of the three, only two are independent.

Using these observations, we see that in 3-D the number of independent real and imaginary parts of either $\tilde{\mathbf{u}}(\mathbf{k})$ or $\tilde{\mathbf{B}}(\mathbf{k})$ is $2N^3$ rather than $3N^3$, for the N^3 independent $\mathbf{k}\in K_3^N$, while for 2-D, this number is N^2, equal to the N^2 independent $\mathbf{k}\in K_2^N$. However, we do not need to use all of the possible $\mathbf{k}\in K_D^N$; we can instead algorithmically include only those $\pm\mathbf{k}$ from a chosen subset $\mathcal{S}\subset K_D^N$. The structure of possible subsets $\mathcal{S}\subset K_D^N$ will be further discussed after an examination of the form of the dynamical equations in k-space.

3.2 Evolution Equations in k-Space

3.2.1 Three-Dimensional Equations

The evolution equations of vorticity and magnetic field in k-space are found by placing (3.4) and (3.5) into (2.43) and (2.44). The result is, using the independence of the $e^{i\mathbf{k}\cdot\mathbf{x}}$,

$$\frac{d\,\tilde{\boldsymbol{\omega}}(\mathbf{k})}{dt} = \tilde{\mathbf{S}}(\tilde{\mathbf{u}},\tilde{\boldsymbol{\omega}};\mathbf{k})+\tilde{\mathbf{S}}(\tilde{\mathbf{j}},\tilde{\mathbf{B}};\mathbf{k})-\nu k^2\tilde{\boldsymbol{\omega}}(\mathbf{k}) \tag{3.15}$$

$$\frac{d\,\tilde{\mathbf{B}}(\mathbf{k})}{dt} = \tilde{\mathbf{S}}(\tilde{\mathbf{u}},\tilde{\mathbf{B}};\mathbf{k})-\eta k^2\tilde{\mathbf{B}}(\mathbf{k}). \tag{3.16}$$

Here, the nonlinear terms denoted by $\tilde{\mathbf{S}}$ are vector convolutions:

$$\tilde{\mathbf{S}}(\tilde{\mathbf{u}},\tilde{\mathbf{B}};\mathbf{k}) \equiv i\mathbf{k}\times\sum_{\mathbf{k},\,\mathbf{p},\,\mathbf{q}\in\mathcal{S}}^{\mathbf{p}+\mathbf{q}=\mathbf{k}}\left[\tilde{\mathbf{u}}(\mathbf{p})\times\tilde{\mathbf{B}}(\mathbf{q})\right]. \tag{3.17}$$

The double summation $\sum_{\mathbf{k},\,\mathbf{p},\,\mathbf{q}\in\mathcal{S}}^{\mathbf{p}+\mathbf{q}=\mathbf{k}}$ in (3.17) is over all wave-vectors $\mathbf{p}$ and $\mathbf{q}$ that satisfy $\mathbf{p}+\mathbf{q}=\mathbf{k}$, where $\pm\mathbf{k},\pm\mathbf{p},\pm\mathbf{q}\in\mathcal{S}\subset K_D^N$.

Thus, Fourier coefficients, such as $\tilde{\mathbf{u}}(\mathbf{k})$, are associated only with a finite number of $\mathbf{k}\in\mathcal{S}\subset K_D^N$, and not with all $\mathbf{k}\in K_D^N$. Notice that, using (3.17), the right sides of (3.15) and (3.16) are identically zero for $\mathbf{k}=\mathbf{0}$. Thus, we may set $\tilde{\mathbf{u}}(\mathbf{0})=\mathbf{0}$ by Galilean invariance (a value it holds for all t), while the constant value of $\tilde{\mathbf{B}}(\mathbf{0})$ may be chosen to be zero or

nonzero to reflect the absence or presence of an externally imposed mean magnetic field. In order to ensure homogeneity, we set $\tilde{\boldsymbol{\omega}}(\mathbf{0}) = \mathbf{0}$ to reflect no overall rotation in the fluid. Also, since $\mathbf{k} \cdot \tilde{\mathbf{S}}(\tilde{\mathbf{u}}, \tilde{\mathbf{B}}; \mathbf{k}) = \mathbf{0}$, then, if (3.12) holds initially, (3.15) and (3.16) show that it will hold for $t > 0$.

The right side of (3.17) contains a vector triple-product that can be expanded as

$$\begin{aligned} \tilde{\mathbf{S}}(\tilde{\mathbf{u}}, \tilde{\mathbf{B}}; \mathbf{k}) &= i \sum_{\mathbf{k},\, \mathbf{p},\, \mathbf{q} \in \mathcal{S}}^{\mathbf{p}+\mathbf{q}=\mathbf{k}} \mathbf{k} \times \Big[\tilde{\mathbf{u}}(\mathbf{p}) \times \tilde{\mathbf{B}}(\mathbf{q}) \Big] \\ &= i \sum_{\mathbf{k},\, \mathbf{p},\, \mathbf{q} \in \mathcal{S}}^{\mathbf{p}+\mathbf{q}=\mathbf{k}} \Big[\mathbf{p} \cdot \tilde{\mathbf{B}}(\mathbf{q})\, \tilde{\mathbf{u}}(\mathbf{p}) - \mathbf{q} \cdot \tilde{\mathbf{u}}(\mathbf{p})\, \tilde{\mathbf{B}}(\mathbf{q}) \Big]. \end{aligned} \tag{3.18}$$

The last step follows from $\mathbf{k} = \mathbf{p} + \mathbf{q}$ and the solenoidality (3.12) of $\tilde{\mathbf{u}}$ and $\tilde{\mathbf{B}}$. If $\mathbf{p}$ and $\mathbf{q}$ are collinear, then, for example, $\mathbf{q} \cdot \tilde{\mathbf{u}}(\mathbf{p}) \sim \mathbf{p} \cdot \tilde{\mathbf{u}}(\mathbf{p}) = 0$, and these wave vectors do not contribute to the right side of (3.18). Thus, in order to have a nonlinear interaction between modes with wave vectors $\mathbf{p}, \mathbf{q} \in \mathcal{S}$, we must have $\mathbf{p} \times \mathbf{q} \neq \mathbf{0}$.

The 3-D vector convolution sums $\tilde{\mathbf{S}}$ defined in (3.17) can also be written as

$$\tilde{\mathbf{S}}(\tilde{\mathbf{u}}, \tilde{\mathbf{B}}; \mathbf{k}) = \mathsf{C}(\mathbf{k}) \cdot \tilde{\mathbf{Q}}(\tilde{\mathbf{u}}, \tilde{\mathbf{B}}; \mathbf{k}), \tag{3.19}$$

where the dyadic $\mathsf{C}(\mathbf{k})$ and the vector $\tilde{\mathbf{Q}}$ are defined by

$$\hat{\mathbf{e}}_i \cdot \mathsf{C}(\mathbf{k}) \cdot \hat{\mathbf{e}}_j = \mathsf{C}_{ij}(\mathbf{k}) = i \epsilon_{imj} k_m \tag{3.20}$$

$$\tilde{\mathbf{Q}}(\tilde{\mathbf{u}}, \tilde{\mathbf{B}}; \mathbf{k}) = \sum_{\mathbf{k},\, \mathbf{p},\, \mathbf{q} \in \mathcal{S}}^{\mathbf{p}+\mathbf{q}=\mathbf{k}} \tilde{\mathbf{u}}(\mathbf{p}) \times \tilde{\mathbf{B}}(\mathbf{q}). \tag{3.21}$$

Here, the *summation convention* is used: $\epsilon_{imj} k_m \equiv \sum_{m=1}^{3} \epsilon_{imj} k_m$, so that repeated indices imply a summation. The ϵ_{ijm} are the components of the *completely alternating tensor*, or *Levi-Civita symbol*, which is defined by

$$\epsilon_{ijk} = \begin{cases} 1, & \text{if } (i,j,k) \text{ are cyclic permutations of } (1,2,3) \\ -1, & \text{if } (i,j,k) \text{ are anticyclic permutations of } (1,2,3) \\ 0, & \text{otherwise.} \end{cases} \tag{3.22}$$

In addition to the *curl operator* $\mathsf{C}(\mathbf{k})$, there are several other important dyadics. The first of these will be denoted by $\mathsf{P}(\mathbf{k})$. It arises when we use (3.13) together with (3.12), to get

$$\begin{aligned} \tilde{\mathbf{u}}(\mathbf{k}) &= i k^{-2} \mathbf{k} \times \tilde{\boldsymbol{\omega}}(\mathbf{k}) \\ &= -k^{-2} \mathbf{k} \times [\mathbf{k} \times \tilde{\mathbf{u}}(\mathbf{k})] \\ &= -k^{-2} \Big[\mathbf{k}\mathbf{k} \cdot \tilde{\mathbf{u}}(\mathbf{k}) - k^2 \tilde{\mathbf{u}}(\mathbf{k}) \Big] \\ &= \mathsf{P}(\mathbf{k}) \cdot \tilde{\mathbf{u}}(\mathbf{k}). \end{aligned} \tag{3.23}$$

This *projection operator* $\mathsf{P}(\mathbf{k})$ is the dyadic defined by

$$\mathsf{P}(\mathbf{k}) \equiv \mathsf{I} - \frac{\mathbf{k}\mathbf{k}}{k^2} \quad \rightarrow \quad \mathsf{P}_{ij} = \delta_{ij} - \frac{k_i k_j}{k^2}. \tag{3.24}$$

Here, the second important dyadic is I, which is the *identity operator*. Next, we define the *adjoint curl* (or 'uncurl') operator $\bar{\mathsf{C}}(\mathbf{k})$:

$$\bar{\mathsf{C}}(\mathbf{k}) \equiv k^{-2}\mathsf{C}(\mathbf{k}). \tag{3.25}$$

The projection, curl and adjoint curl operators satisfy

$$\begin{aligned}
\mathbf{k}\cdot\mathsf{P}(\mathbf{k}) &= \mathsf{P}(\mathbf{k})\cdot\mathbf{k} = \mathbf{0} \\
\mathbf{k}\cdot\mathsf{C}(\mathbf{k}) &= \mathsf{C}(\mathbf{k})\cdot\mathbf{k} = \mathbf{0} \\
\mathbf{k}\cdot\bar{\mathsf{C}}(\mathbf{k}) &= \bar{\mathsf{C}}(\mathbf{k})\cdot\mathbf{k} = \mathbf{0} \\
\mathsf{P}(\mathbf{k})\cdot\mathsf{P}(\mathbf{k}) &= \mathsf{P}(\mathbf{k}) \\
\mathsf{C}(\mathbf{k})\cdot\mathsf{P}(\mathbf{k}) &= \mathsf{P}(\mathbf{k})\cdot\mathsf{C}(\mathbf{k}) = \mathsf{C}(\mathbf{k}) \\
\bar{\mathsf{C}}(\mathbf{k})\cdot\mathsf{P}(\mathbf{k}) &= \mathsf{P}(\mathbf{k})\cdot\bar{\mathsf{C}}(\mathbf{k}) = \bar{\mathsf{C}}(\mathbf{k}) \\
\bar{\mathsf{C}}(\mathbf{k})\cdot\mathsf{C}(\mathbf{k}) &= \mathsf{C}(\mathbf{k})\cdot\bar{\mathsf{C}}(\mathbf{k}) = \mathsf{P}(\mathbf{k}) \\
\mathsf{C}(\mathbf{k})\cdot\mathsf{C}(\mathbf{k}) &= k^2\mathsf{P}(\mathbf{k}) \\
\bar{\mathsf{C}}(\mathbf{k})\cdot\bar{\mathsf{C}}(\mathbf{k}) &= k^{-2}\mathsf{P}(\mathbf{k}).
\end{aligned} \tag{3.26}$$

Note that $\bar{\mathsf{C}}(\mathbf{k})$ is not quite the inverse of $\mathsf{C}(\mathbf{k})$.

We can use the operators just defined, to rewrite (3.13) as

$$\tilde{\mathbf{u}}(\mathbf{k}) = \bar{\mathsf{C}}(\mathbf{k})\cdot\tilde{\boldsymbol{\omega}}(\mathbf{k}) = -\tilde{\boldsymbol{\omega}}(\mathbf{k})\cdot\bar{\mathsf{C}}(\mathbf{k}) \tag{3.27}$$

$$\tilde{\mathbf{B}}(\mathbf{k}) = \bar{\mathsf{C}}(\mathbf{k})\cdot\tilde{\mathbf{j}}(\mathbf{k}) = -\tilde{\mathbf{j}}(\mathbf{k})\cdot\bar{\mathsf{C}}(\mathbf{k}) \tag{3.28}$$

and also to rewrite (3.15) and (3.16) as

$$\frac{d\,\tilde{\boldsymbol{\omega}}(\mathbf{k})}{dt} = \mathsf{C}(\mathbf{k})\cdot\left[\tilde{\mathbf{Q}}(\tilde{\mathbf{u}},\tilde{\boldsymbol{\omega}};\mathbf{k}) + \tilde{\mathbf{Q}}(\tilde{\mathbf{j}},\tilde{\mathbf{B}};\mathbf{k})\right] - \nu k^2\tilde{\boldsymbol{\omega}}(\mathbf{k}) \tag{3.29}$$

$$\frac{d\,\tilde{\mathbf{B}}(\mathbf{k})}{dt} = \mathsf{C}(\mathbf{k})\cdot\tilde{\mathbf{Q}}(\tilde{\mathbf{u}},\tilde{\mathbf{B}};\mathbf{k}) - \eta k^2\tilde{\mathbf{B}}(\mathbf{k}). \tag{3.30}$$

Now, we can apply $\bar{\mathsf{C}}(\mathbf{k})$ to (3.28) to arrive at a definition of the k-space *stream vector* $\tilde{\boldsymbol{\psi}}$ and magnetic *vector potential* $\tilde{\mathbf{A}}$:

$$\tilde{\boldsymbol{\psi}}(\mathbf{k}) = \bar{\mathsf{C}}(\mathbf{k})\cdot\tilde{\mathbf{u}}(\mathbf{k}) = k^{-2}\tilde{\boldsymbol{\omega}}(\mathbf{k}) \tag{3.31}$$

$$\tilde{\mathbf{A}}(\mathbf{k}) = \bar{\mathsf{C}}(\mathbf{k})\cdot\tilde{\mathbf{B}}(\mathbf{k}) = k^{-2}\tilde{\mathbf{j}}(\mathbf{k}). \tag{3.32}$$

Using (3.32 and (3.28), along with (3.21) and (3.26), and applying $\bar{\mathsf{C}}(\mathbf{k})$ to (3.29) and (3.30) gives

$$\frac{d\,\tilde{\mathbf{u}}(\mathbf{k})}{dt} = \mathsf{P}(\mathbf{k}) \cdot \left[\tilde{\mathbf{Q}}(\tilde{\mathbf{u}}, \tilde{\boldsymbol{\omega}}; \mathbf{k}) + \tilde{\mathbf{Q}}(\tilde{\mathbf{j}}, \tilde{\mathbf{B}}; \mathbf{k})\right] - \nu k^2 \tilde{\mathbf{u}}(\mathbf{k}) \tag{3.33}$$

$$\frac{d\,\tilde{\mathbf{A}}(\mathbf{k})}{dt} = \mathsf{P}(\mathbf{k}) \cdot \tilde{\mathbf{Q}}(\tilde{\mathbf{u}}, \tilde{\mathbf{B}}; \mathbf{k}) - \eta k^2 \tilde{\mathbf{A}}(\mathbf{k}). \tag{3.34}$$

Equations for $\tilde{\boldsymbol{\psi}}$ and $\tilde{\mathbf{j}}$ could be similarly generated, if desired.

It has already been mentioned that the magnetic field may contain a nonzero component $\tilde{\mathbf{B}}(\mathbf{k})$ for $\mathbf{k} = \mathbf{0}$. Let the constant *mean magnetic field* be $\mathbf{B}_\mathrm{o} = \tilde{\mathbf{B}}(\mathbf{0})$, and let $\tilde{\mathbf{b}}(\mathbf{k}) = \tilde{\mathbf{B}}(\mathbf{k})$ for $\mathbf{k} \neq \mathbf{0}$, with $\tilde{\mathbf{b}}(\mathbf{0}) = \mathbf{0}$, so that (3.21) becomes

$$\tilde{\mathbf{Q}}(\tilde{\mathbf{u}}, \tilde{\mathbf{B}}; \mathbf{k}) = \tilde{\mathbf{Q}}(\tilde{\mathbf{u}}, \tilde{\mathbf{b}}; \mathbf{k}) + \tilde{\mathbf{u}}(\mathbf{k}) \times \mathbf{B}_\mathrm{o}. \tag{3.35}$$

Also, we will define $\tilde{\mathbf{a}}(\mathbf{k}) = ik^{-2}\mathbf{k} \times \tilde{\mathbf{b}}(\mathbf{k}) = k^{-2}\tilde{\mathbf{j}}(\mathbf{k})$. Since $\tilde{\mathbf{j}}(\mathbf{0}) = \mathbf{0}$, then $\tilde{\mathbf{Q}}(\tilde{\mathbf{j}}, \tilde{\mathbf{B}}; \mathbf{k})$ can be obtained by letting $\tilde{\mathbf{u}} \to \tilde{\mathbf{j}}$ in (3.35). These results allow the evolution equations (3.29), (3.30), (3.33), and (3.34) to be written

$$\frac{d\,\tilde{\boldsymbol{\omega}}(\mathbf{k})}{dt} = \mathsf{C}(\mathbf{k}) \cdot \left[\tilde{\mathbf{Q}}(\tilde{\mathbf{u}}, \tilde{\boldsymbol{\omega}}; \mathbf{k}) + \tilde{\mathbf{Q}}(\tilde{\mathbf{j}}, \tilde{\mathbf{b}}; \mathbf{k})\right] + i(\mathbf{k} \cdot \mathbf{B}_\mathrm{o})\,\tilde{j}(\mathbf{k}) - \nu k^2 \tilde{\boldsymbol{\omega}}(\mathbf{k}) \tag{3.36}$$

$$\frac{d\,\tilde{\mathbf{b}}(\mathbf{k})}{dt} = \mathsf{C}(\mathbf{k}) \cdot \tilde{\mathbf{Q}}(\tilde{\mathbf{u}}, \tilde{\mathbf{b}}; \mathbf{k}) + i(\mathbf{k} \cdot \mathbf{B}_\mathrm{o})\,\tilde{\mathbf{u}}(\mathbf{k}) - \eta k^2 \tilde{\mathbf{b}}(\mathbf{k}). \tag{3.37}$$

$$\frac{d\,\tilde{\mathbf{u}}(\mathbf{k})}{dt} = \mathsf{P}(\mathbf{k}) \cdot \left[\tilde{\mathbf{Q}}(\tilde{\mathbf{u}}, \tilde{\boldsymbol{\omega}}; \mathbf{k}) + \tilde{\mathbf{Q}}(\tilde{\mathbf{j}}, \tilde{\mathbf{b}}; \mathbf{k})\right] + i(\mathbf{k} \cdot \mathbf{B}_\mathrm{o})\,\tilde{\mathbf{b}}(\mathbf{k}) - \nu k^2 \tilde{\mathbf{u}}(\mathbf{k}) \tag{3.38}$$

$$\frac{d\,\tilde{\mathbf{a}}(\mathbf{k})}{dt} = \mathsf{P}(\mathbf{k}) \cdot \tilde{\mathbf{Q}}(\tilde{\mathbf{u}}, \tilde{\mathbf{b}}; \mathbf{k}) + i(\mathbf{k} \cdot \mathbf{B}_\mathrm{o})\,\tilde{\boldsymbol{\psi}}(\mathbf{k}) - \eta k^2 \tilde{\mathbf{a}}(\mathbf{k}). \tag{3.39}$$

Many more equations can be generated through the application of $\mathsf{C}(\mathbf{k})$ and $\bar{\mathsf{C}}(\mathbf{k})$ to these equations. However, for our purposes here, the above will be sufficient.

3.2.2 Two-Dimensional Equations

The equations (3.36), (3.37), (3.38), and (3.39) are fully three-dimensional but can be reduced to a 2-D form as follows. In 2-D x-space, (2.45) allows us to write vorticity and current as

$$\boldsymbol{\omega}(\mathbf{x}) = \omega(\mathbf{x})\hat{\mathbf{z}} \quad \text{and} \quad \mathbf{j}(\mathbf{x}) = j(\mathbf{x})\hat{\mathbf{z}}, \tag{3.40}$$

where $\mathbf{x} = x\hat{\mathbf{x}} + y\hat{\mathbf{y}}$. In 2-D k-space, using (3.12), (3.31), and (3.32) leads to the following relation between Fourier coefficients:

$$\tilde{\boldsymbol{\omega}}(\mathbf{k}) \;=\; \tilde{\omega}(\mathbf{k})\hat{\mathbf{z}} \;=\; k^2\tilde{\psi}(\mathbf{k})\hat{\mathbf{z}} \;=\; k^2\tilde{\boldsymbol{\psi}}(\mathbf{k}) \tag{3.41}$$

$$\tilde{\mathbf{j}}(\mathbf{k}) \;=\; \tilde{j}(\mathbf{k})\hat{\mathbf{z}} \;=\; k^2\tilde{a}(\mathbf{k})\hat{\mathbf{z}} \;=\; k^2\tilde{\mathbf{a}}(\mathbf{k}) \tag{3.42}$$

where $\mathbf{k} = k_x\hat{\mathbf{x}} + k_y\hat{\mathbf{y}}$, $\tilde{\psi}$ is the scalar stream function and $\tilde{a}$ is the scalar magnetic potential. In the 2-D case, (3.13), along with (3.41) and (3.42), leads to the following expressions for the velocity and magnetic fields in k-space:

$$\tilde{\mathbf{u}}(\mathbf{k}) = i\,\mathbf{k}\times\hat{\mathbf{z}}\,\tilde{\psi}(\mathbf{k}) \quad\text{and}\quad \tilde{\mathbf{b}}(\mathbf{k}) = i\,\mathbf{k}\times\hat{\mathbf{z}}\,\tilde{a}(\mathbf{k}). \tag{3.43}$$

Thus there is exactly only one independent complex component in $\tilde{\mathbf{u}}(\mathbf{k})$ and one in $\tilde{\mathbf{b}}(\mathbf{k})$, a reflection of the fact that they are 2-D solenoidal vector fields. A 2-D magnetofluid can thus be described by $\tilde{\psi}(\mathbf{k})$ and $\tilde{a}(\mathbf{k})$, whose evolution equations follow from equations (3.43), (3.36), and (3.39):

$$\begin{aligned}\frac{d\,\tilde{\omega}(\mathbf{k})}{dt} \;=\; & i\sum_{\mathbf{k},\,\mathbf{p},\,\mathbf{q}\,\in\mathcal{S}}^{\mathbf{p}+\mathbf{q}=\mathbf{k}} \hat{\mathbf{z}}\cdot\mathbf{p}\times\mathbf{q}\left[\tilde{\psi}(\mathbf{p})\,\tilde{\omega}(\mathbf{q}) + \tilde{j}(\mathbf{p})\,\tilde{a}(\mathbf{q})\right] \\ & + i(\mathbf{k}\cdot\mathbf{B}_{\rm o})\,\tilde{j}(\mathbf{k}) - \nu k^2\tilde{\omega}(\mathbf{k})\end{aligned} \tag{3.44}$$

$$\begin{aligned}\frac{d\,\tilde{a}(\mathbf{k})}{dt} \;=\; & -i\sum_{\mathbf{k},\,\mathbf{p},\,\mathbf{q}\,\in\mathcal{S}}^{\mathbf{p}+\mathbf{q}=\mathbf{k}} \hat{\mathbf{z}}\cdot\mathbf{p}\times\mathbf{q}\;\tilde{\psi}(\mathbf{p})\,\tilde{a}(\mathbf{q}) \\ & + i(\mathbf{k}\cdot\mathbf{B}_{\rm o})\,\tilde{\psi}(\mathbf{k}) - \eta k^2\tilde{a}(\mathbf{k}).\end{aligned} \tag{3.45}$$

Here, we have used $\tilde{\omega}(\mathbf{k}) = k^2\tilde{\psi}(\mathbf{k})$ and $\tilde{j}(\mathbf{k}) = k^2\tilde{a}(\mathbf{k})$, as given in (3.41) and (3.42). Since $\mathbf{p}$ and $\mathbf{q}$ are 2-D vectors, $\mathbf{p}\times\mathbf{q} = (p_xq_y - p_yq_x)\hat{\mathbf{z}}$ and $\hat{\mathbf{z}}\cdot\mathbf{p}\times\mathbf{q} = p_xq_y - p_yq_x$. Also, remember that the double sum in (3.45) is over all $\mathbf{p}$ and $\mathbf{q}$ such that $\mathbf{p}+\mathbf{q} = \mathbf{k}$ and $\mathbf{k},\mathbf{p},\mathbf{q}\in\mathcal{S}\subset K_2^N$. As in the 3-D case, equations (3.44) and (3.45) clearly indicate that only wave vectors $\mathbf{p}$ and $\mathbf{q}$ such that $\mathbf{p}\times\mathbf{q}\neq 0$ can interact nonlinearly and thereby affect the time-evolution of the Fourier mode $\mathbf{k}$.

3.2.3 Alfvén Waves

Here we consider the dynamical equations when $B_{\rm o}$ is relatively large. Let us define the *Alfvén frequency* for a mode $\mathbf{k}$ as

$$\zeta(\mathbf{k}) \;\equiv\; \mathbf{k}\cdot\mathbf{B}_{\rm o}. \tag{3.46}$$

In the 3-D case, if all the terms on the right sides of equations (3.37) and (3.38) except the terms containing $\zeta(\mathbf{k})$ are dropped, these equations become

$$\frac{d\,\tilde{\mathbf{b}}(\mathbf{k})}{dt} \;=\; i\,\zeta(\mathbf{k})\,\tilde{\mathbf{u}}(\mathbf{k}) \tag{3.47}$$

$$\frac{d\,\tilde{\mathbf{u}}(\mathbf{k})}{dt} = i\,\zeta(\mathbf{k})\,\tilde{\mathbf{b}}(\mathbf{k}). \tag{3.48}$$

These can be combined into one linear, second-order differential equation:

$$\frac{d^2\,\tilde{\mathbf{b}}(\mathbf{k})}{dt^2} = -\,\zeta^2(\mathbf{k})\,\tilde{\mathbf{b}}(\mathbf{k}), \tag{3.49}$$

which has two solutions:

$$\tilde{\mathbf{b}}^{(\pm)}(\mathbf{k}) = \tilde{\mathbf{b}}_{\mathrm{o}}^{(\pm)}(\mathbf{k})\,\exp[\pm i\zeta(\mathbf{k})t]. \tag{3.50}$$

Using (3.47) produces the corresponding velocity coefficient solutions:

$$\tilde{\mathbf{u}}^{(\pm)}(\mathbf{k}) = \pm\tilde{\mathbf{b}}^{(\pm)}(\mathbf{k}). \tag{3.51}$$

The x-space waves corresponding to these Fourier coefficients are

$$\mathbf{b}^{(\pm)}(\mathbf{x},t) = \pm\mathbf{u}^{(\pm)}(\mathbf{x},t) = \tilde{\mathbf{b}}_{\mathrm{o}}^{(\pm)}(\mathbf{k})\,\exp[i\mathbf{k}\cdot(\mathbf{x}\pm\mathbf{B}_{\mathrm{o}}t)]. \tag{3.52}$$

The linear waves $\mathbf{b}^{(\pm)}(\mathbf{x},t) = \pm\mathbf{u}^{(\pm)}(\mathbf{x},t)$ are called *Alfvén waves*. Furthermore, the waves $\mathbf{b}^{(-)}(\mathbf{x},t)$ and $\mathbf{u}^{(-)}(\mathbf{x},t)$ propagate in the direction of the corresponding $\mathbf{k}$, with speed B_{o}, while $\mathbf{b}^{(+)}(\mathbf{x},t)$ and $\mathbf{u}^{(+)}(\mathbf{x},t)$ propagate in the opposite direction at the same speed. In the linear approximation, Alfvén waves do not interact, but if B_{o} is no longer 'large,' then they do interact, in which case Alfvén waves may lose their individual identities.

The linear analysis above produces pairs of solutions $\mathbf{b}^{(\pm)}(\mathbf{x},t)$ and $\mathbf{u}^{(\pm)}(\mathbf{x},t)$, which are coplanar. Thus, these results go over directly into the 2-D case, where the equations corresponding to (3.47) and (3.48) come from the linearization of (3.44) and (3.45), with $\nu = \eta = 0$. Using (3.43), (3.50), and (3.51), along with and (3.41), yields the ideal 2-D MHD Alfvén wave solutions in k-space:

$$\tilde{a}^{(\pm)}(\mathbf{k}) = \pm\tilde{\psi}^{(\pm)}(\mathbf{k}) = \tilde{a}_{\mathrm{o}}^{(\pm)}(\mathbf{k})\,\exp[\pm i\zeta(\mathbf{k})t]. \tag{3.53}$$

The corresponding x-space equations are

$$a^{(\pm)}(\mathbf{x},t) = \pm\psi^{(\pm)}(\mathbf{x},t) = \tilde{a}_{\mathrm{o}}^{(\pm)}(\mathbf{k})\,\exp[i\mathbf{k}\cdot(\mathbf{x}\pm\mathbf{B}_{\mathrm{o}}t)]. \tag{3.54}$$

Although, in general, Alfvén waves may lose their individual identities in the presence of nonlinearity, some remnants of Alfvén wave-like behavior may persist in MHD turbulence. In fact, this will be apparent when numerical results are presented in a later chapter.

3.3 Interacting Fourier Modes

In the previous section, nonlinear evolution equations for the Fourier modes $\tilde{\boldsymbol{\omega}}(\mathbf{k})$ and $\tilde{\mathbf{b}}(\mathbf{k})$ were developed, for both the 2-D and 3-D cases. Once we choose a grid size for a numerical simulation, we have a finite number of $\mathbf{k} \in K_D^N$ to choose from; in fact, we choose $\pm\mathbf{k} \in \mathcal{S} \subset K_D^N$, and the choice of $\mathcal{S}$ is essentially arbitrary. For example we could choose to work with only one $\mathbf{k} = \mathbf{k}_1 \neq \mathbf{0}$ (and $-\mathbf{k}$, of course), setting the Fourier modes associated with all other $\mathbf{k} \in \mathcal{S} \subset K_D^N$ equal to zero. In this case, only the mode associated with $\pm\mathbf{k}_1$ is time advanced, but there is no nonlinear evolution, since all other modes are frozen with zero values. This is, of course, a trivial case, but there are many other possible subsets $\mathcal{S}$ of K_D^N that can be chosen. The simplest nonlinearly interacting system is one associated with a subset of K_D^N containing three wave vectors (and their negatives). All other interacting subsets of K_D^N will be unions of these basic *interacting triads*.

However, choosing one or an arbitrary union of interacting triads may impose an unwanted anisotropy on the model system, if what is really desired is to have a set of wave vectors which give no intrinsic directionality to the model system. Restricting the choice of a subset $\mathcal{S}$ of K_D^N so that no particular direction in space is favored is called an *isotropic truncation*. In what follows, we specifically discuss these two choices: interacting triads and isotropic truncation.

3.3.1 Interacting Triads

The basic nonlinear interaction in ideal turbulence is quadratic, as was seen explicitly in the last section. In terms of nonzero wave vectors $\mathbf{k}, \mathbf{p}, \mathbf{q} \in K_D^N$, $D = 2, 3$, Fourier modes associated with nonzero wave vectors $\pm\mathbf{k}, \pm\mathbf{p}, \pm\mathbf{q}$ can nonlinearly interact only if they form a fundamental *interacting triad*: $\mathbf{k} = \mathbf{p} + \mathbf{q}$, where $\mathbf{p} \times \mathbf{q} \neq 0$. These are the *minimal interacting subsets* of the K_D^N (any other interacting subset is a union of these fundamental subsets).

An interacting triad $\mathcal{T} \subset K_D^N$ thus consists of three independent wave vectors $\mathbf{k}, \mathbf{p}, \mathbf{q} \in K_D^N$:

$$\begin{aligned} \mathcal{T} &= \{\pm\mathbf{k}, \pm\mathbf{p}, \pm\mathbf{q}\} \\ \mathbf{k} &= \mathbf{p} + \mathbf{q}, \quad \mathbf{p} \times \mathbf{q} \neq \mathbf{0}. \end{aligned} \tag{3.55}$$

Note that, because of (3.14), we must have both a wave vector and its negative in $\mathcal{T}$ (however, remember that $\mathbf{k}$ and $-\mathbf{k}$ identify the same mode). Also, note that although $\mathcal{T}$ has wave vectors that satisfy $\mathbf{k} = \mathbf{p} + \mathbf{q}$, it does not contain $\mathbf{k}' = \mathbf{p} - \mathbf{q}$. If a model system were to include only modes associated with wave vectors in $\mathcal{T}$, then only these would advance in time and all other modes would remain zero, having been set so initially. (In atmospheric science, truncation of a buoyant fluid model to three modes led to the well-known *Lorenz attractor*.)

Using the definition, (3.55), consider the two sets of interacting triads $\mathcal{T}_1$ and $\mathcal{T}_2$:

$$\mathcal{T}_1 = \{\pm\mathbf{k}_1, \pm\mathbf{p}_1, \pm\mathbf{q}_1\}$$

$$\mathcal{T}_2 \;=\; \{\pm\mathbf{k}_2, \pm\mathbf{p}_2, \pm\mathbf{q}_2\}. \tag{3.56}$$

If $\mathcal{T}_1 \cap \mathcal{T}_2 = \emptyset$, then the subsets $\mathcal{T}_1$ and $\mathcal{T}_2$ do not interact with one another. However, assuming that at least one independent wave vector in $\mathcal{T}_1$ is equal to one in $\mathcal{T}_2$ (for example, $\mathbf{p}_1 = \mathbf{p}_2$), then the subset $\mathcal{S} = \mathcal{T}_1 \cup \mathcal{T}_2$ is also a set of interacting wave vectors which contains $\mathcal{T}_1$ and $\mathcal{T}_2$:

$$\mathcal{S} \;=\; \{\pm\mathbf{k}_i, \pm\mathbf{p}_i, \pm\mathbf{q}_i \mid i = 1, 2\} \tag{3.57}$$

For example, consider the following interacting triads of 2-D wave vectors:

$$\begin{aligned}
\mathcal{T}_1 &= \{\pm(1,0), \pm(0,1), \pm(1,1)\} \\
\mathcal{T}_2 &= \{\pm(1,0), \pm(0,1), \pm(1,-1)\} \\
\mathcal{T}_3 &= \{\pm(2,1), \pm(1,1), \pm(1,0)\} \\
\mathcal{T}_4 &= \{\pm(2,0), \pm(0,2), \pm(2,2)\}
\end{aligned} \tag{3.58}$$

The first three triads, $\mathcal{T}_i,\ i = 1, 2, 3$, share common elements and pair-wise unions of any two of them will yield larger subsets of interacting wave vectors. However, $\mathcal{T}_4 \cap \mathcal{T}_i = \emptyset,\ i = 1, 2, 3$, so that any union $\mathcal{S}_i = \mathcal{T}_4 \cup \mathcal{T}_i,\ i = 1, 2, 3$ will consist of two non-interacting triads, rather than a fully interacting subset. In this last case, $\mathcal{T}_4$ and any of the $\mathcal{T}_i,\ i = 1, 2, 3$, though formally united, evolve independently of one another.

We can thus use the subsets $\mathcal{T}_i \subset K_D^N$ (with $N \geq 2$) of interacting triads to define larger sets, $\mathcal{S}_1$ and $\mathcal{S}_2$, such that $\mathcal{S}_1 \cap \mathcal{S}_2 = \emptyset$. These two sets $\mathcal{S}_1$ and $\mathcal{S}_2$ do not interact with one another, and if there are no other interacting sets allowed in the numerical simulation which would link them, then they will evolve independent of one another. For $N \geq 2$, any nonzero $\mathbf{k} \in K_D^N$ can always be written as $\mathbf{k} = \mathbf{p} + \mathbf{q}$, with nonzero $\mathbf{p}, \mathbf{q} \in K_D^N$, where $\mathbf{p}$ and $\mathbf{q}$ satisfy $\mathbf{p} \times \mathbf{q} \neq 0$.

To show this, consider a nonzero, 3-D wave vector: $\mathbf{k} = k_x\hat{\mathbf{x}} + k_y\hat{\mathbf{y}} + k_z\hat{\mathbf{z}}$. If at least two of the k_i, $i = x, y, z$, are definitely nonzero, say k_x and k_y, then we can immediately write:

$$\mathbf{p} = k_x\hat{\mathbf{x}}, \quad \mathbf{q} = k_y\hat{\mathbf{y}} + k_z\hat{\mathbf{z}} \quad \rightarrow \quad \mathbf{k} = \mathbf{p} + \mathbf{q}. \tag{3.59}$$

Here we have $p^2, q^2 < k^2$ and $\mathbf{p} \times \mathbf{q} = -k_x k_z \hat{\mathbf{x}} + k_x k_y \hat{\mathbf{z}} \neq 0$.

If only one of the k_i, $i = x, y, z$, is nonzero, and the other two are zero, say $k_x = \pm\kappa$ ($\kappa > 0$) and $k_y = k_z = 0$, so that $\mathbf{k} = \pm\kappa\hat{\mathbf{x}}$, then we have two cases:

$$\begin{aligned}
&\mathbf{p} = \;\; (\kappa - 1)\hat{\mathbf{x}} + \hat{\mathbf{y}}, \quad \mathbf{q} = \;\; \hat{\mathbf{x}} - \hat{\mathbf{y}} \rightarrow \mathbf{k} = \mathbf{p} + \mathbf{q} \quad (k_x = \;\; \kappa > 0) \\
&\mathbf{p} = (-\kappa + 1)\hat{\mathbf{x}} - \hat{\mathbf{y}}, \quad \mathbf{q} = -\hat{\mathbf{x}} + \hat{\mathbf{y}} \rightarrow \mathbf{k} = \mathbf{p} + \mathbf{q} \quad (k_x = -\kappa < 0).
\end{aligned} \tag{3.60}$$

In both cases ($k_x = \pm\kappa$), we have $p^2 = k^2 - 2(\kappa - 1)$, $q^2 = 2$, and $\mathbf{p} \times \mathbf{q} = -\kappa\hat{\mathbf{z}} \neq 0$. Here, if $\kappa > 1$, then $p^2, q^2 < k^2 = \kappa^2$, while if $\kappa = 1$, we have $p^2 = k^2 = 1 < q^2 = 2$.

3.3.2 Isotropic Truncation

If we were to pick an upper limit to the magnitude of a wave vector, say k_{max}, where $k_{max}^2 > 2$, then the results (3.59) and (3.60) indicate that any vector $\mathbf{k}$ that satisfies $k^2 \leq k_{max}^2 < (N/2)^2$, can be decomposed into two wave vectors $\mathbf{p}$ and $\mathbf{q}$, such that $\mathbf{k} = \mathbf{p} + \mathbf{q}$, with $p^2, q^2 \leq k_{max}^2$. This gives us another type of subset, $\mathcal{K} \subset K_D^N$ ($N = 2^M > 2$), which also has all triads linked together. Thus, the *isotropic truncation* of K_D^N produces

$$\mathcal{K} = \{\mathbf{k} \mid \mathbf{k} \in K_D^N,\ k^2 \leq k_{max}^2 < (N/2)^2\}. \tag{3.61}$$

In defining $\mathcal{K}$ by (3.61), we have constrained the number of dynamically important $\mathbf{k}$ so as to avoid imposing any initial anisotropy. We have *isotropically truncated* the domain of $\mathbf{k}$ by using only those Fourier components with wave-vectors $\mathbf{k}$ lying on or inside the sphere defined by $k \leq k_{max} < N/2$. All coefficients with $k > k_{max}$ are set to zero and kept there during numerical simulation (*i.e.*, after every time-step). Only coefficients with $k \leq k_{max}$ are allowed to evolve according to the algorithm used to define the numerical simulation.

The fact that we set $k_{max} < N/2$ is a small but important point. Consider the Fourier modes corresponding to $\mathbf{k}_1 = (N/2, 0, 0)$ (and to $\mathbf{k}_2 = (0, N/2, 0)$ and $\mathbf{k}_3 = (0, 0, N/2)$). Using $\mathbf{x}$ as given by (3.3), we have $e^{i\mathbf{k}_j \cdot \mathbf{x}} = (-1)^{n_j}$, $j = 1, 2, 3$, so that modes determined by (3.6) and (3.7) are purely real for $\mathbf{k} = \mathbf{k}_j$, $j = 1, 2, 3$. A spatial derivative of such a component corresponds to multiplication by $i\mathbf{k}$, which transforms the real part of the component into an imaginary one, and the imaginary part (which is zero, in this case) into a real part. Thus, the Fourier mode of a derivative associated with one of the $\mathbf{k}_j$, which is also purely real, is identically zero. Since the evolution of Fourier components is a function of their spatial derivatives, any interacting set of wave-vectors should exclude the $\mathbf{k}_j$, $j = 1, 2, 3$ (as well as such wave vectors as $\mathbf{k}_4 = (N/2, N/2, 0)$, etc.).

The number of $\mathbf{k}$ within an 'isotropic' 2-D circle is approximately equal to $M_2 \approx \pi k_{max}^2$, and within an 'isotropic' 3-D sphere is approximately equal to $M_3 \approx 4\pi k_{max}^3/3$. More precisely, M_2 and M_3 are given by

$$M_D = \sum_{\mathbf{k} \in K_D^N} H(k_{max} - k), \quad D = 2, 3, \quad H(\sigma) = \begin{array}{ll} 1, & \text{if } \sigma \geq 0 \\ 0, & \text{if } \sigma < 0. \end{array} \tag{3.62}$$

Since M_D is the total number of Fourier vector modes actually utilized, and since there is one independent component per $\mathbf{k}$ in 2-D and two in 3-D, then the total number of independent components per physical field ($\mathbf{u}$ or $\mathbf{B}$) is, in 2-D, M_2, and, in 3-D, $2M_3$.

Clearly, the *total number of independent components* in the Fourier modes $\mathbf{k} \in K_D^N$ used to represent each physical field is reduced by isotropic truncation (3.62). In 2-D k-space,

this reduction is to F_2, and in 3-D k-space, to F_3, where

$$F_2 = M_2 \approx \pi k_{max}^2 < \frac{\pi}{4} N^2 \tag{3.63}$$

$$F_3 = 2M_3 \approx \frac{8}{3} \pi k_{max}^3 < \frac{\pi}{3} N^3. \tag{3.64}$$

The actual value of F_D depends on the choice of k_{max}, which is set by computational constraints. However, note that the sums (3.4) and (3.5) can still be taken over all N^D modes $\mathbf{k}$ because those coefficients with $k > k_{max}$ have values defined algorithmically as zero.

3.4 Ideal Integral Invariants

If $\nu = \eta = 0$ in the evolution equations, then there exist certain *integral invariants* which are analytical constants of the motion. They are termed 'integral invariants' because they are integrals over the physical space of various bilinear forms. For example, an integral that may be invariant is

$$(\mathbf{u}, \mathbf{b}) \equiv \frac{1}{(2\pi)^D} \int \mathbf{u}(\mathbf{x}) \cdot \mathbf{b}(\mathbf{x}) \, d^D x, \quad D = 2, 3. \tag{3.65}$$

If we use Fourier transforms similar to (3.5) for $\mathbf{u}$ and $\mathbf{b}$, then (3.65) becomes

$$\begin{aligned}
(\mathbf{u}, \mathbf{b}) &= \frac{1}{(2\pi)^D} \int \left[\sum_{\mathbf{k}' \in K_D^N} \tilde{\mathbf{u}}(\mathbf{k}') \, e^{i\mathbf{k}' \cdot \mathbf{x}} \right] \cdot \left[\sum_{\mathbf{k} \in K_D^N} \tilde{\mathbf{b}}(\mathbf{k}) \, e^{i\mathbf{k} \cdot \mathbf{x}} \right] \, d^D x \\
&= \sum_{\mathbf{k}, \mathbf{k}' \in K_D^N} \tilde{\mathbf{u}}(\mathbf{k}') \cdot \tilde{\mathbf{b}}(\mathbf{k}) \, \frac{1}{(2\pi)^D} \int e^{i(\mathbf{k}' + \mathbf{k}) \cdot \mathbf{x}} \, d^D x \\
&= \sum_{\mathbf{k}, \mathbf{k}' \in K_D^N} \tilde{\mathbf{u}}(\mathbf{k}') \cdot \tilde{\mathbf{b}}(\mathbf{k}) \, \delta(\mathbf{k} + \mathbf{k}') \\
&= \sum_{\mathbf{k} \in K_D^N} \tilde{\mathbf{u}}(-\mathbf{k}) \cdot \tilde{\mathbf{b}}(\mathbf{k}) \\
&= \sum_{\mathbf{k} \in K_D^N} \tilde{\mathbf{u}}^*(\mathbf{k}) \cdot \tilde{\mathbf{b}}(\mathbf{k}), \quad D = 2, 3.
\end{aligned} \tag{3.66}$$

Above, the *Dirac delta function* is

$$\delta(\mathbf{k} + \mathbf{k}') = \frac{1}{(2\pi)^D} \int e^{i(\mathbf{k}' + \mathbf{k}) \cdot \mathbf{x}} \, d^D x. \tag{3.67}$$

Although we started from the integral (3.65) over a continuous x-space, we could also have started with a summation over the discrete x-space (3.3), and defined

$$(\mathbf{u}, \mathbf{b}) = \frac{1}{N^D} \sum_{\mathbf{x} \in X_D^N} \mathbf{u}(\mathbf{x}) \cdot \mathbf{b}(\mathbf{x}), \quad D = 2, 3. \tag{3.68}$$

Then, using transforms similar to (3.5) again, along with the *Krönecker delta*

$$\delta_{\mathbf{k},\mathbf{k}'} = \frac{1}{N^D} \sum_{\mathbf{x} \in X_D^N} e^{i(\mathbf{k}'+\mathbf{k})\cdot\mathbf{x}}, \quad D = 2, 3, \tag{3.69}$$

would have led once again to the result in (3.66). Although we could now use the term 'summation invariant,' we will stick to the more standard term of 'integral invariant.'

When $\nu = \eta = 0$, the integral invariants that are found in the magnetofluid equations depend on the specific type of flow that is under consideration. First, the flow may be 3-D or 2-D. Then, a flow with $\mathbf{B} \equiv 0$ for all time is called an *Euler flow*, and with $\mathbf{B} \neq 0$, it is called an *ideal MHD* flow. Finally, an ideal MHD flow may have $\mathbf{B}_o = 0$ or $\mathbf{B}_o \neq 0$. Thus, there are six different types of flow, and they have different sets of integral invariants. These six different cases will now be discussed.

3.4.1 3-D Invariants

There are three different cases here: 3-D Euler invariants, 3-D ideal MHD ($|\mathbf{B}_o| = B_o = 0$) invariants, and 3-D ideal MHD ($B_o = 1$) invariants. [Normalization: In the Euler cases, $\mathbf{u}$ is usually initialized so that $(\mathbf{u}, \mathbf{u}) = 1$, while in the ideal MHD cases, $\mathbf{u}$ and $\mathbf{b}$ are typically initialized so that $(\mathbf{u}, \mathbf{u}) + (\mathbf{b}, \mathbf{b}) = 2$, where $(\cdot, \cdot)$ is defined by (3.65), (3.66) or (3.68).]

3-D Euler Invariants

If we categorically set $\mathbf{B}(\mathbf{x}, t) = 0$ for all t, then we reduce the number of equations by half. In this case, (3.36) and (3.38) become the following:

$$\frac{d\,\tilde{\boldsymbol{\omega}}(\mathbf{k})}{dt} = \mathsf{C}(\mathbf{k}) \cdot \tilde{\mathbf{Q}}(\tilde{\mathbf{u}}, \tilde{\boldsymbol{\omega}}; \mathbf{k}) - \nu k^2 \tilde{\boldsymbol{\omega}}(\mathbf{k}) \tag{3.70}$$

$$\frac{d\,\tilde{\mathbf{u}}(\mathbf{k})}{dt} = \mathsf{P}(\mathbf{k}) \cdot \tilde{\mathbf{Q}}(\tilde{\mathbf{u}}, \tilde{\boldsymbol{\omega}}; \mathbf{k}) - \nu k^2 \tilde{\mathbf{u}}(\mathbf{k}). \tag{3.71}$$

If we take the dot product of (3.71) with $\tilde{\mathbf{u}}^*(\mathbf{k})$, we get

$$\tilde{\mathbf{u}}^*(\mathbf{k}) \cdot \frac{d\,\tilde{\mathbf{u}}(\mathbf{k})}{dt} = \tilde{\mathbf{u}}^*(\mathbf{k}) \cdot \tilde{\mathbf{Q}}(\tilde{\mathbf{u}}, \tilde{\boldsymbol{\omega}}; \mathbf{k}) - \nu k^2 |\tilde{\mathbf{u}}(\mathbf{k})|^2. \tag{3.72}$$

Now, if we change $\mathbf{k} \to -\mathbf{k}$ in (3.72), add the resulting equation to (3.72), and sum over $\mathbf{k}$, we get

$$\sum_{\mathbf{k} \in \mathcal{S}} \left[\frac{d\,|\tilde{\mathbf{u}}(\mathbf{k})|^2}{dt} + 2\,\nu\,k^2 |\tilde{\mathbf{u}}(\mathbf{k})|^2 \right] = T(\tilde{\mathbf{u}}, \tilde{\mathbf{u}}, \tilde{\boldsymbol{\omega}}). \tag{3.73}$$

Here, using (3.21), the *triple-product summation* T is defined by

$$\begin{aligned} T(\tilde{\mathbf{u}},\tilde{\mathbf{u}},\tilde{\boldsymbol{\omega}}) &= \sum_{\mathbf{k}\in\mathcal{S}} \left[\tilde{\mathbf{u}}^*(\mathbf{k})\cdot\tilde{\mathbf{Q}}(\tilde{\mathbf{u}},\tilde{\boldsymbol{\omega}};\mathbf{k}) + \tilde{\mathbf{u}}(\mathbf{k})\cdot\tilde{\mathbf{Q}}^*(\tilde{\mathbf{u}},\tilde{\boldsymbol{\omega}};\mathbf{k})\right] \\ &= 2\sum_{\mathbf{k}\in\mathcal{S}} \tilde{\mathbf{u}}(\mathbf{k})\cdot\tilde{\mathbf{Q}}^*(\tilde{\mathbf{u}},\tilde{\boldsymbol{\omega}};\mathbf{k}) \\ &= 2\sum_{\mathbf{k},\,\mathbf{p},\,\mathbf{q}\,\in\mathcal{S}}^{\mathbf{k}+\mathbf{p}+\mathbf{q}=\mathbf{0}} \tilde{\mathbf{u}}(\mathbf{k})\cdot\tilde{\mathbf{u}}(\mathbf{p})\times\tilde{\boldsymbol{\omega}}(\mathbf{q}) \\ &= \sum_{\mathbf{k},\,\mathbf{p},\,\mathbf{q}\,\in\mathcal{S}}^{\mathbf{k}+\mathbf{p}+\mathbf{q}=\mathbf{0}} [\tilde{\mathbf{u}}(\mathbf{k})\times\tilde{\mathbf{u}}(\mathbf{p}) + \tilde{\mathbf{u}}(\mathbf{p})\times\tilde{\mathbf{u}}(\mathbf{k})]\cdot\tilde{\boldsymbol{\omega}}(\mathbf{q}) \\ &= 0. \end{aligned} \tag{3.74}$$

The triple summation $\sum_{\mathbf{k},\,\mathbf{p},\,\mathbf{q}\,\in\mathcal{S}}^{\mathbf{k}+\mathbf{p}+\mathbf{q}=\mathbf{0}}$ is the summation over all wave-vectors $\mathbf{k},\mathbf{p},\mathbf{q}$ such that $\mathbf{k}+\mathbf{p}+\mathbf{q}=0$ and $\pm\mathbf{k},\pm\mathbf{p},\pm\mathbf{q}\in\mathcal{S}\subset K_3^N$. We have exercised the option of changing the dummy index $\mathbf{k}\to-\mathbf{k}$ in the second step above, and used the fact that the summation on the right side can be made symmetric over $\mathbf{k}$ and $\mathbf{p}$ (and $\mathbf{q}$ also, if necessary). Thus, from (3.73) and (3.74) we have, using the equivalence $k^2|\tilde{\mathbf{u}}(\mathbf{k})|^2 = |\tilde{\boldsymbol{\omega}}(\mathbf{k})|^2$,

$$\frac{d\,E_K}{dt} = -2\,\nu\,\Omega. \tag{3.75}$$

Here, *kinetic energy* E_K and the *enstrophy* Ω are defined using (3.66):

$$E_K \equiv \frac{1}{2}\,(\mathbf{u},\mathbf{u}) \tag{3.76}$$

$$\Omega \equiv \frac{1}{2}\,(\boldsymbol{\omega},\boldsymbol{\omega}). \tag{3.77}$$

If $\nu=0$, it is clear that E_K is a constant of the motion, *i.e.*, invariant. If $\nu\neq 0$, then, since $\Omega\geq 0$, E_K always decreases, unless $\Omega=0$, in which case $E_K=0$, also.

Next, if we take the dot product of (3.71) with $\tilde{\boldsymbol{\omega}}^*(\mathbf{k})$, and take the dot product of (3.70) (after changing $\mathbf{k}\to-\mathbf{k}$), with $\tilde{\mathbf{u}}(\mathbf{k})$, use $\tilde{\mathbf{u}}(\mathbf{k})\cdot\mathsf{C}(\mathbf{k})(-\mathbf{k}) = \tilde{\boldsymbol{\omega}}(\mathbf{k})$, add the two equations, and sum over $\mathbf{k}$, we get

$$\sum_{\mathbf{k}\in\mathcal{S}} \left[\frac{d\;\tilde{\mathbf{u}}(\mathbf{k})\cdot\tilde{\boldsymbol{\omega}}^*(\mathbf{k})}{dt} + 2\,\nu\,k^2\,\tilde{\mathbf{u}}(\mathbf{k})\cdot\tilde{\boldsymbol{\omega}}^*(\mathbf{k})\right] = T(\tilde{\boldsymbol{\omega}},\tilde{\mathbf{u}},\tilde{\boldsymbol{\omega}}). \tag{3.78}$$

Here, as we did in (3.74), we again partially symmetrize the triple-product sum on the right side:

$$\begin{aligned} T(\tilde{\boldsymbol{\omega}},\tilde{\mathbf{u}},\tilde{\boldsymbol{\omega}}) &= \sum_{\mathbf{k},\,\mathbf{p},\,\mathbf{q}\,\in\mathcal{S}}^{\mathbf{k}+\mathbf{p}+\mathbf{q}=\mathbf{0}} [\tilde{\boldsymbol{\omega}}(\mathbf{k})\times\tilde{\boldsymbol{\omega}}(\mathbf{q}) + \tilde{\boldsymbol{\omega}}(\mathbf{q})\times\tilde{\boldsymbol{\omega}}(\mathbf{k})]\cdot\tilde{\mathbf{u}}(\mathbf{p}) \\ &= 0. \end{aligned} \tag{3.79}$$

Thus, (3.78) becomes

$$\frac{d\,H_K}{dt} \;=\; -2\,\nu\,H_V. \tag{3.80}$$

The *kinetic helicity* H_K and (giving it a name) the *vortical helicity* H_V are defined, again using (3.66):

$$H_K \;\equiv\; \frac{1}{2}\,(\mathbf{u},\boldsymbol{\omega}) \tag{3.81}$$

$$H_V \;\equiv\; \frac{1}{2}\,(\boldsymbol{\omega},\nabla\times\boldsymbol{\omega}). \tag{3.82}$$

In the 3-D Euler case, H_K is the second integral invariant. (Neither H_K nor H_V are positive-definite.)

In the present case, there are no other bilinear integral invariants because, looking at (3.74) and (3.79), it is clear that in order for the triple-product summation

$$T(\mathbf{u},\mathbf{v},\boldsymbol{\omega}) \;=\; \sum_{\mathbf{k},\,\mathbf{p},\,\mathbf{q}\,\in\mathcal{S}}^{\mathbf{k}+\mathbf{p}+\mathbf{q}=\mathbf{0}} \tilde{\mathbf{u}}(\mathbf{k})\cdot\tilde{\mathbf{v}}(\mathbf{p})\times\tilde{\boldsymbol{\omega}}(\mathbf{q}) \tag{3.83}$$

to be equal to zero, at least two out of the three vectors $\tilde{\mathbf{u}}$, $\tilde{\mathbf{v}}$, $\tilde{\boldsymbol{\omega}}$ must be equal (up to a constant factor). Another way of saying this is to note that, by (3.83), $T(\mathbf{u},\mathbf{v},\boldsymbol{\omega})$ is antisymmetric in its arguments:

$$T(\mathbf{u},\mathbf{v},\boldsymbol{\omega}) \;=\; -T(\mathbf{v},\mathbf{u},\boldsymbol{\omega}) \;=\; -T(\mathbf{u},\boldsymbol{\omega},\mathbf{v}). \tag{3.84}$$

Thus, if $\tilde{\mathbf{u}}$ and $\tilde{\boldsymbol{\omega}}$ are fixed, there are only two choices for $\mathbf{v}$ such that $T(\mathbf{u},\mathbf{v},\boldsymbol{\omega})=0$: either $\tilde{\mathbf{v}}=\tilde{\mathbf{u}}$ or $\tilde{\mathbf{v}}=\tilde{\boldsymbol{\omega}}$. As we have just seen, these choices lead, respectively, to the two invariants E_K, defined in (3.76), and H_K, defined in (3.81).

3-D Ideal MHD Invariants

In this case, $\mathbf{B}\neq 0$, and we have 3-D ideal MHD flows when $\nu=\eta=0$. If we take the dot product of $\tilde{\mathbf{u}}^*(\mathbf{k})$ with (3.38), then the result of this, added to its complex conjugate, gives

$$\sum_{\mathbf{k}\in\mathcal{S}}\left[\frac{d\,|\tilde{\mathbf{u}}(\mathbf{k})|^2}{dt} + 2\,i\,(\mathbf{k}\cdot\mathbf{B}_{\rm o})\tilde{\mathbf{u}}^*(\mathbf{k})\cdot\tilde{\mathbf{b}}(\mathbf{k}) - 2\,\nu\,|\tilde{\boldsymbol{\omega}}(\mathbf{k})|^2\right] \;=\; T(\tilde{\mathbf{u}},\tilde{\mathbf{u}},\tilde{\boldsymbol{\omega}}) + T(\tilde{\mathbf{u}},\tilde{\mathbf{j}},\tilde{\mathbf{b}}). \tag{3.85}$$

Similarly, if we take the dot product of $\tilde{\mathbf{b}}^*(\mathbf{k})$ with (3.37), then the result of this, added to its complex conjugate, gives

$$\sum_{\mathbf{k}\in\mathcal{S}}\left[\frac{d\,|\tilde{\mathbf{b}}(\mathbf{k})|^2}{dt} - 2\,i\,(\mathbf{k}\cdot\mathbf{B}_{\rm o})\tilde{\mathbf{u}}^*(\mathbf{k})\cdot\tilde{\mathbf{b}}(\mathbf{k}) - 2\,\eta\,|\tilde{\mathbf{j}}(\mathbf{k})|^2\right] \;=\; T(\tilde{\mathbf{j}},\tilde{\mathbf{u}},\tilde{\mathbf{b}}). \tag{3.86}$$

Adding (3.85) and (3.86), and using (3.84), gives

$$\frac{d\,E}{dt} \;=\; -2\,(\nu\,\Omega + \eta\,J). \tag{3.87}$$

In the above equation, Ω is given by (3.77), the *total energy* E is a sum of kinetic energy E_K, given by (3.76), and *magnetic energy* E_M, while J is the *mean-square current*. We have

$$E \;=\; E_K + E_M \tag{3.88}$$

$$E_M \;\equiv\; \frac{1}{2}\,(\mathbf{b},\mathbf{b}) \tag{3.89}$$

$$J \;\equiv\; \frac{1}{2}\,(\mathbf{j},\mathbf{j}). \tag{3.90}$$

It is clear from (3.87) that E, as given by (3.88), is an integral invariant for $\nu = \eta = 0$.

Next, take the dot product of $\tilde{\mathbf{b}}^*(\mathbf{k})$ with (3.38), add this to the dot product of $\tilde{\mathbf{u}}(\mathbf{k})$ with the complex conjugate of (3.37), and use (3.84) to produce

$$\sum_{\mathbf{k}\in\mathcal{S}} \left[\frac{d}{dt} + (\nu+\eta)\,k^2\right]\,\tilde{\mathbf{u}}(\mathbf{k})\cdot\tilde{\mathbf{b}}^*(\mathbf{k}) \;=\; 0. \tag{3.91}$$

Defining the *cross helicity* H_C as

$$H_C \;\equiv\; \frac{1}{2}\,(\mathbf{u},\mathbf{b}) \tag{3.92}$$

allows (3.91) to be rewritten as

$$\frac{d\,H_C}{dt} \;=\; -\,(\nu+\eta)H_C. \tag{3.93}$$

The cross helicity is obviously an integral invariant for 3-D ideal MHD, where $\nu = \eta = 0$.

Notice that E in (3.88) and H_C in (3.92) are integral invariants for ideal MHD for both $B_\mathrm{o} = 0$ and $B_\mathrm{o} \neq 0$. Keeping this in mind, the result of taking the dot product of $\tilde{\mathbf{a}}^*(\mathbf{k})$ with (3.37), and adding this to its complex conjugate, again using (3.84), is

$$\sum_{\mathbf{k}\in\mathcal{S}} \left[\frac{d}{dt} + 2\,\eta\,k^2\right]\,\tilde{\mathbf{a}}(\mathbf{k})\cdot\tilde{\mathbf{b}}^*(\mathbf{k}) \;=\; -i\sum_{\mathbf{k}\in\mathcal{S}}(\mathbf{k}\cdot\mathbf{B}_\mathrm{o})\,\tilde{\mathbf{a}}(\mathbf{k})\cdot\tilde{\mathbf{u}}^*(\mathbf{k}). \tag{3.94}$$

Defining the *magnetic helicity* H_M as

$$H_M \;\equiv\; \frac{1}{2}\,(\mathbf{a},\mathbf{b}), \tag{3.95}$$

we see that H_M is an integral invariant in 3-D ideal MHD, but only if $\mathbf{B}_\mathrm{o} = 0$.

There are no other bilinear invariants for 3-D ideal MHD, and the absence or presence of a nonzero mean magnetic field splits 3-D ideal homogeneous MHD turbulence into two cases: If $\mathbf{B}_\mathrm{o} = 0$, E, H_C and H_M are ideal invariants, while if $\mathbf{B}_\mathrm{o} \neq 0$, only E and H_C are ideal invariants. We mention again that E, H_C, and H_M, as well as $\mathbf{k}\cdot\tilde{\mathbf{u}}(\mathbf{k})$ and $\mathbf{k}\cdot\tilde{\mathbf{B}}(\mathbf{k})$, are zero only to machine accuracy.

3.4.2 2-D Invariants

There are also three different cases here: 2-D Euler invariants, 2-D ideal MHD ($|\mathbf{B}_o| = B_o = 0$) invariants, and 2-D ideal MHD ($B_o = 1$) invariants.

2-D Euler Invariants

As in 3-D flow, there is no magnetic field present at all in this case. Let us examine (3.44) with $\tilde{\mathbf{j}} = \tilde{\mathbf{a}} = 0$:

$$\frac{d\,\tilde{\omega}(\mathbf{k})}{dt} \;=\; i \sum_{\mathbf{k},\,\mathbf{p},\,\mathbf{q}\,\in\mathcal{S}}^{\mathbf{p}+\mathbf{q}=\mathbf{k}} \hat{\mathbf{z}}\cdot\mathbf{p}\times\mathbf{q}\,\tilde{\psi}(\mathbf{p})\,\tilde{\omega}(\mathbf{q}) - \nu\,k^2\,\tilde{\omega}(\mathbf{k}). \tag{3.96}$$

If we multiply this equation by $\tilde{\phi}^*_n = k^n\,\tilde{\psi}^*(\mathbf{k})$, add the result to its own complex conjugate, and sum over $\mathbf{k}\in\mathcal{S}\subset K_2^N$, we get

$$\sum_{\mathbf{k}\in\mathcal{S}}\left[\frac{d}{dt} + 2\,\nu\,k^2\right]\,k^{n+2}\,|\tilde{\psi}(\mathbf{k})|^2 \;=\; \theta(\phi,\psi,\omega), \tag{3.97}$$

where

$$\theta(\phi,\psi,\omega) \;=\; 2\,i \sum_{\mathbf{k},\,\mathbf{p},\,\mathbf{q}\,\in\mathcal{S}}^{\mathbf{k}+\mathbf{p}+\mathbf{q}=\mathbf{0}} \hat{\mathbf{z}}\cdot\mathbf{p}\times\mathbf{q}\,\tilde{\phi}(\mathbf{k})\,\tilde{\psi}(\mathbf{p})\,\tilde{\omega}(\mathbf{q}). \tag{3.98}$$

In the summation above, the indices $\mathbf{k}$, $\mathbf{p}$, and $\mathbf{q}$ are dummies and can be interchanged freely to yield relations similar to (3.84):

$$\theta(\phi,\psi,\omega) \;=\; -\,\theta(\psi,\phi,\omega) \;=\; -\,\theta(\phi,\omega,\psi). \tag{3.99}$$

The triple summation $\theta(\phi,\psi,\omega) = 0$ if $\phi = \psi$ or $\phi = \omega$, that is, if $n = 0$ or $n = 2$, respectively. Then, for $\nu = 0$, (3.97) indicates that the following (and only the following) are ideal invariants for 2-D homogeneous Euler turbulence:

$$E_K \;=\; \frac{1}{2}\sum_{\mathbf{k}\in\mathcal{S}} k^2\,|\tilde{\psi}(\mathbf{k})|^2 \;=\; \frac{1}{2}\sum_{\mathbf{k}\in\mathcal{S}} |\tilde{\mathbf{u}}(\mathbf{k})|^2 \tag{3.100}$$

$$\Omega \;=\; \frac{1}{2}\sum_{\mathbf{k}\in\mathcal{S}} k^4\,|\tilde{\psi}(\mathbf{k})|^2 \;=\; \frac{1}{2}\sum_{\mathbf{k}\in\mathcal{S}} |\tilde{\omega}(\mathbf{k})|^2. \tag{3.101}$$

Again, E_K is the kinetic energy and Ω is the enstrophy.

Kelvin's Theorem

The x-space equation corresponding to (3.96) with $\nu = 0$ is

$$\frac{d\omega}{dt} \;=\; \frac{\partial\omega}{\partial t} + \mathbf{u}\cdot\nabla\omega \;=\; 0. \tag{3.102}$$

This equation tells us that the vorticity of each fluid element is conserved in 2-D ideal flow as it is convected about the flow region. This is *Kelvin's circulation theorem.* Since $d\omega/dt = 0$, we also have

$$\omega^{\alpha-1}\frac{d\omega}{dt} \quad = \quad \frac{d\omega^{\alpha}}{dt} \quad = \quad 0, \quad \alpha \geq 1, \tag{3.103}$$

so that any non-negative power of ω associated with a fluid element is also conserved as that element moves around. (We require $\alpha \geq 1$ so that (3.103) is defined for all finite ω, including $\omega = 0$.) Thus, the integral of ω^{α} over the flow region (here, a periodic box), is also conserved, for any $\alpha \geq 1$:

$$I_{\alpha} \quad = \quad \iint \omega^{\alpha}\, dx\, dy \quad = \quad const. \tag{3.104}$$

If α is drawn from the set of real numbers greater than or equal to one, (3.104) appears to imply that there are an *uncountable* infinity of integral invariants for 2-D Euler flow. However, if we restrict ourselves to a periodic domain, then α must be a positive integer, so that the number of invariants is, in fact, denumerable. As we have just seen, only the case with $\alpha = 2$ actually leads to a non-trivial invariant in a finite Fourier representation. Such a quantity is often referred to as a 'rugged invariant.'

The reason that Kelvin's theorem does not appear to carry over is three-fold. First, Kelvin's theorem essentially states that the vorticity of each fluid point, and thus all powers of vorticity of each fluid point, are conserved in a 2-D ideal fluid. This is a statement concerning the continuum and is not commensurate with the fundamental nature of a discrete Fourier representation. Second, Parseval's identity guarantees only the equality of Ω, as defined in k-space by (3.101), and I_2, as defined in x-space by (3.104). Third, as will be seen in the next chapter, the $\boldsymbol{\omega}(\mathbf{k})$, in a numerical simulation, essentially comprise a set of random variables with a normal probability distribution. For such a set of random variables, the expectation values $\langle I_{2n-1} \rangle = 0$, while $\langle I_{2n} \rangle = (2n-1)!!\, \langle I_2 \rangle^n$, for $n = 1, 2, 3, \ldots$. Also, as $n \to \infty$, fluctuations in I_{2n} are found to grow exponentially. Thus, only $\Omega = I_2$ can be expected to behave like an invariant, either analytically or computationally – a truly *rugged* invariant. In a sense, the $\langle I_{2n} \rangle$, $n > 1$, are also 'invariant,' since they are proportional to $\langle I_2 \rangle^n$, but their fluctuations are so great that they cannot be considered 'rugged.'

2-D Ideal MHD Invariants

In order to determine the integral invariants for 2-D ideal MHD, multiply (3.44) by $\tilde{\phi}_1^*(\mathbf{k})$, multiply the complex conjugate of (3.45) by $\tilde{\phi}_2(\mathbf{k})$, add the resulting equations, and sum over $\mathbf{k} \in K_2^N$ to get

$$\sum_{\mathbf{k}\in\mathcal{S}} \left[\tilde{\phi}_1^*(\mathbf{k})\, \frac{d\,\tilde{\omega}(\mathbf{k})}{dt} + \tilde{\phi}_2(\mathbf{k})\, \frac{d\,\tilde{a}^*(\mathbf{k})}{dt} \right]$$

$$= \quad \frac{1}{2}\, [\, \theta(\phi_1, \psi, \omega) + \theta(\phi_1, j, a) + \theta(\phi_2, \psi, a)]$$

$$+\sum_{\mathbf{k}\in\mathcal{S}} i\mathbf{k}\cdot\mathbf{B}_o\left[\tilde{j}(\mathbf{k})\,\tilde{\phi}_1^*(\mathbf{k})-\tilde{\phi}_2(\mathbf{k})\,\tilde{\psi}^*(\mathbf{k})\right]$$
$$-\sum_{\mathbf{k}\in\mathcal{S}} k^2\,\left[\nu\,\tilde{\omega}(\mathbf{k})\,\tilde{\phi}_1^*(\mathbf{k})+\eta\,\tilde{\phi}_2(\mathbf{k})\,\tilde{a}^*(\mathbf{k})\right]. \tag{3.105}$$

A choice of functions ϕ_1 and ϕ_2 will produce an invariant only if the left side of this equation is a perfect differential and if the right side vanishes for $\nu=\eta=0$.

There are only three choices: 1) $\phi_1=\psi$, $\phi_2=j$; 2) $\phi_1=a$, $\phi_2=\omega$; and 3) $\phi_1=0$, $\phi_2=a$. The first choice ($\phi_1=\psi$, $\phi_2=j$) yields (3.87), so that the total energy $E=E_K+E_M$ is an ideal invariant for 2-D MHD. Here, E_K and Ω are defined by (3.100) and (3.101), while E_M and J are defined by

$$E_M = \frac{1}{2}\sum_{\mathbf{k}\in\mathcal{S}} k^2\,|\tilde{a}(\mathbf{k})|^2 = \frac{1}{2}\sum_{\mathbf{k}\in\mathcal{S}} |\tilde{\mathbf{b}}(\mathbf{k})|^2 \tag{3.106}$$

$$J = \frac{1}{2}\sum_{\mathbf{k}\in\mathcal{S}} k^4\,|\tilde{a}(\mathbf{k})|^2 = \frac{1}{2}\sum_{\mathbf{k}\in\mathcal{S}} |\tilde{j}(\mathbf{k})|^2. \tag{3.107}$$

The second choice ($\phi_1=a$, $\phi_2=\omega$) yields (3.93), so that the cross helicity H_C is also an ideal invariant for 2-D MHD:

$$H_C = \frac{1}{2}\sum_{\mathbf{k}\in\mathcal{S}} \tilde{\omega}^*(\mathbf{k})\,\tilde{a}(\mathbf{k}) = \frac{1}{2}\sum_{\mathbf{k}\in\mathcal{S}} \tilde{\psi}^*(\mathbf{k})\tilde{j}(\mathbf{k}). \tag{3.108}$$

The third choice ($\phi_1=0$, $\phi_2=a$) yields

$$\frac{d\,A}{dt} = \sum_{\mathbf{k}\in\mathcal{S}} i\mathbf{k}\cdot\mathbf{B}_o\tilde{a}^*(\mathbf{k})\,\tilde{\psi}_1(\mathbf{k})-2\,\eta\,E_M, \tag{3.109}$$

where A is the *mean square magnetic potential*:

$$A = \frac{1}{2}\sum_{\mathbf{k}\in\mathcal{S}} |\tilde{a}(\mathbf{k})|^2. \tag{3.110}$$

It is clear from (3.109) that A is an ideal invariant in 2-D MHD, but only if $\mathbf{B}_o=0$.

To summarize the results for ideal 2-D MHD, E, H_C and A are integral invariants when $\mathbf{B}_o=0$, but only E and H_C are ideal invariants when $\mathbf{B}_o\neq 0$. We now have at hand the integral invariants for the six different types of ideal, incompressible, homogeneous turbulence, and we will use these in the development of the associated statistical theory. Again, it must be stressed that these integral invariants are 'constant' only to machine accuracy during a numerical simulation. Although fluctuations may be slight, they allow the development of a useful statistical mechanics, which describes the behavior of computer models of ideal homogeneous turbulence, and hopefully has some relevance to more realistic models of turbulence and ultimately to real-world turbulence itself. It is the basics of this statistical mechanics that we develop in the next chapter.

3.5 References for Further Reading

Discrete Fourier transforms are covered in detail in [Hamming 86] and in [Bracewell 86].

The energy is a well-known classical invariant for any conservative physical system. Other invariants for ideal homogeneous fluid and magnetofluid turbulence were recognized more recently: Ω [Kraichnan 75], H_K [Betchov 61], H_C [Woltjer 58], H_M [Elsässer 56], and A [Fyfe 76].

Chapter 4

Statistical Mechanics

The evolution of the Fourier modes introduced in the last chapter is determined by sets of first-order, nonlinear ordinary differential equations which couple components of different wave vectors $\mathbf{k}$ to one another. The coupling is highly nonlinear, the various Fourier components are observed to behave stochastically and so must be considered *random variables*. This suggests that a statistical description of the multidimensional dynamics of turbulence is required. Although a statistical theory has been elusive for real, dissipative turbulence, it is possible for computer models of ideal turbulence and follows rather straightforwardly from the principles of classical equilibrium statistical physics. The novelty of ideal turbulent flows is that several integral invariants exist and must be utilized, whereas in classical statistics only the energy is needed.

Our particular goal is to develop a statistical mechanics that allows us to analytically predict expectation values of moments of random variables and to compare these predictions with the results of a numerical solution of the equations of motion. In fact, our statistical theory must take into account the approximations inherent in computer simulation, specifically fluctuations during a numerical solution due to time-step size and round-off error. These fluctuations actually bring the statistical behavior of a computer model closer to that of a realistic physical system. A mesoscale physical system may be generally thought of as a small part of a larger 'heat bath,' and a computer model may similarly be viewed as a small system embedded in a computer, which serves as its heat bath. In equilibrium, the interaction between a 'small system' and 'heat bath' is only through fluctuations, and the statistics of such a small system are best described in terms of *canonical*, rather than *microcanonical* ensembles. In addition to being the most appropriate, a canonical ensemble distribution function can be more readily used for actual calculations. Historically, the use of canonical ensembles to give a statistical explanation of ideal homogeneous turbulence was given the name *absolute equilibrium ensemble theory*. It is this theory that we develop in this chapter.

4.1 Turbulence as a Dynamical System

Each of the independent real and imaginary parts of the velocity and magnetic field components $\tilde{\mathbf{u}}(\mathbf{k})$ and $\tilde{\mathbf{B}}(\mathbf{k})$ can be associated with the components of a single, time-dependent vector $\mathbf{v}(t)$ in a higher dimensional space, called a *phase space* and denoted by Γ. The *phase vector* $\mathbf{v}$ defines the location of a *phase point*, which completely describes the instantaneous state of the system under investigation. (Although this could have been done using x-space grid point values, along with the equations of motion in finite difference form, here we choose to work in k-space, as the essential dimension of the phase space is manifest, among other benefits.) In the last chapter, we transformed the equations of motion of a magnetofluid, from x-space into k-space. This effectively created a nonlinear *dynamical system* to serve as a mathematical model of a magnetofluid.

For homogeneous turbulence, the dimension n_d of the dynamical system follows from (3.63) for 2-D flows, and from (3.64) for 3-D flows. In 2-D, we use the complex scalar functions $\tilde{\omega}(\mathbf{k})$ and $\tilde{a}(\mathbf{k})$ to define the phase space, while in 3-D, we use three complex components of each of the vectors $\tilde{\mathbf{u}}(\mathbf{k})$ and $\tilde{\mathbf{b}}(\mathbf{k})$ to define the phase space. However, in 3-D, the three components are kinematically linked by solenoidality (3.12), so that only two are independent. Thus, not all of the phase space axes for 3-D turbulence are independent and the number of phase space dimensions is larger than n_d, but this redundancy is tolerable since there is no inherent reason to prefer any two of the components over a third. The dimension of the phase space is determined by grid size, for either 2-D or 3-D turbulence and also whether $\mathbf{B} \equiv 0$ or not. In the 2-D Euler case, the dimension of the phase space is $n = n_d = F_2$, while in the 2-D MHD case, the dimension is $n = n_d = 2F_2$, where F_2 is given by (3.63). In the 3-D Euler case, the dimension of the phase space is $n = 3\ over 2n_d = 3\ over 2F_3$, while in the 3-D MHD case, the dimension is $n = 3\ over 2n_d = 3F_3$, where F_3 is given by (3.64). In planning a numerical implementation, the argument can be reversed, since computational speed and available core memory dictate the value of the grid size N^D, thereby setting the largest practical n and n_d.

The equations of the dynamical systems created using isotropically truncated Fourier expansions all have the following appearance:

$$\frac{d\,v_j}{dt} \;=\; f_j(\mathbf{v}) - \kappa_j v_j. \tag{4.1}$$

(Above, there is no sum over the repeated indices.) The n-dimensional vector $\mathbf{v}$ has components v_j, $j = 1, \ldots, n$, each of which represent a different independent component, for example, drawn from the 3-D Fourier vectors $\tilde{\mathbf{u}}(\mathbf{k})$ and $\tilde{\mathbf{b}}(\mathbf{k})$, or from the 2-D scalars $\tilde{\omega}(\mathbf{k})$ and $\tilde{a}(\mathbf{k})$. The constant κ_j is either νk^2 or ηk^2, as appropriate for the particular v_j. The term f_j contains the nonlinear coupling of the different v_j. Thus, (4.1) can represent any of the 2-D or 3-D evolution equations discussed in the last chapter. Since (4.1) has no external driving force on its right side, it is termed *autonomous*, so that we are dealing here with an autonomous, nonlinear dynamical system.

4.2 Canonical Ensembles

Thus far, we have abstracted the various 2-D and 3-D finite Fourier models of fluid and magnetofluid turbulence that appeared in the last chapter into the form of an n_d-dimensional dynamical system contained in an n dimensional phase space and represented by a phase vector $\mathbf{v}$ that satisfies (4.1). Effectively, we have the whole system identified with a single point in the n-dimensional phase space Γ ($n \gg 1$), whose trajectory $\mathbf{v}(t)$, we assume, follows some *phase path*, beginning at some initial point $\mathbf{v}(0)$, and satisfies certain constraints. Here we will specify some of these constraints by initially assigning specific, self-consistent values to the ideal integral invariants associated with whichever one of the six different cases of homogeneous turbulence we are studying. Each ideal invariant is essentially an equation that defines a hypersurface of dimension $n-1$ in Γ. In addition, the solenoidal constraints (3.12) define a host of other hypersurfaces for cases of 3-D turbulence. The intersection of all hypersurfaces is the *invariant subspace* or *manifold* for the particular case being studied.

If the integral invariants were strictly conserved and known to infinite accuracy, the invariant manifold would have either $n_d - 2$ or $n_d - 3$ independent dimensions, depending on whether the dynamical system has two or three ideal integral invariants. In the case of strict conservation, the probability that a phase point was on the invariant manifold would be unity and the probability that it was off the invariant manifold would be zero.

As an example, in 3-D ideal Euler turbulence the invariants are the energy $E = E_K$ (3.76) and the kinetic helicity H_K (3.81). If these were exactly conserved, they would always be equal to their initial values: $E = E^{[0]}$ and $H_K = H_K^{[0]}$. Then, the probability distribution D_μ would be given by

$$D_\mu \;=\; \delta(E - E^{[0]})\,\delta(H_K - H_K^{[0]}). \tag{4.2}$$

The phase function D_μ is the *microcanonical ensemble* probability distribution (or density). Again, its use would be required if the ideal invariants were strictly conserved, although its use in the calculation of expectation values would be a great challenge, since the integration must take place on a rather complicated hypersurface in Γ (called the *invariant manifold*).

However, on a computer, invariant values are defined only to a finite level of accuracy and, as the system evolves, errors in the computed values of $\tilde{\mathbf{u}}(\mathbf{k})$ and $\tilde{\mathbf{b}}(\mathbf{k})$ will occur and cause the value of each ideal invariant to be satisfied only up to small fluctuations. This, in turn, will cause what would have been the microcanonical invariant manifold to move about during a simulation. The result is that the fluctuating phase point sweeps out a 'fuzzy' hypersurface in Γ. In this case, the distribution of phase points is best described by a smooth phase function D (but one that is highly peaked on the average position of the 'fuzzy' hypersurface). Such a phase function is called a *canonical* probability distribution or density.

Since $n \gg 1$, the 'invariant manifold' is generally nontrivial and there are many choices for its initial points $\mathbf{v}(0)$. In fact, on a digital computer, there will be a finite, though very large number, of possible $\mathbf{v}(0)$, which form the set $\mathcal{V}_0$ of all initial values of $\mathbf{v}$ at $t = 0$ consistent with the initial values of the ideal invariants and the inherent accuracy of the computer.

Again, $\mathcal{V}_0$ would be the invariant manifold for a microcanonical system, since it contains all $\mathbf{v} \in \Gamma$ that satisfy all constraints (to machine accuracy). On the other hand, a *canonical ensemble* is the set $\mathcal{V}$ of all $\mathbf{v}(t)$, as defined by numerical implementation of (4.1), following from all of the possible $\mathbf{v}(0)$. Although all $\mathbf{v}(0) \in \mathcal{V}_0$ are equally probable initial values, the points $\mathbf{v}(t) \in \mathcal{V} \sim \Gamma$ are not all equally probable, but instead have a probability determined by the canonical probability density D. Therefore $\mathcal{V}_0$ is the *initial manifold*, which broadens, due to fluctuations, into the (fuzzy) invariant manifold for a canonical system. The form of D will be determined after a discussion of Liouville's theorem.

4.3 Liouville's Theorem

The finite set $\mathcal{V}_0 \ni \mathbf{v}(0)$ can be thought of as a 'gas' of noninteracting points which move about according to (4.1). If the distribution of these points in Γ at any time t is given by D, then the number of points δn in the small volume of phase space $\delta\Gamma$ is $\delta n = D\,\delta\Gamma$. In analogy with our development of the continuity equation (2.7), we require that the δn remains constant (*i.e.*, the number of points is conserved):

$$\begin{aligned} \frac{d\,\delta n}{dt} &= \frac{d\,D\,\delta\Gamma}{dt} \\ &= \delta\Gamma\,\frac{d\,D}{dt} + D\,\frac{d\,\delta\Gamma}{dt} \\ &= 0. \end{aligned} \tag{4.3}$$

The small phase space volume $\delta\Gamma$ can be expressed as

$$\delta\Gamma = \prod_{i=1}^{n} \delta\, v_i, \tag{4.4}$$

so that

$$\begin{aligned} \frac{d\,\delta\Gamma}{dt} &= \sum_{j=1}^{n} \frac{d\,\delta\, v_j}{dt} \prod_{i\neq j} \delta\, v_i \\ &= \sum_{j=1}^{n} \delta\,\frac{d\,v_j}{dt} \prod_{i\neq j} \delta\, v_i \\ &= \sum_{j=1}^{n} \delta\,[f_j(\mathbf{v}) - \kappa_j v_j] \prod_{i\neq j} \delta v_i \\ &= \sum_{j=1}^{n} \left[\frac{\partial\, f_j(\mathbf{v})}{\partial v_j} - \kappa_j\right] \delta v_j \prod_{i\neq j} \delta v_i \\ &= -\sum_{j=1}^{n} \kappa_j\,\delta\Gamma. \end{aligned} \tag{4.5}$$

The last step follows from (4.4) and because $f_j(\mathbf{v})$ does not contain v_j (as can be seen by looking at any of the evolution equations of the last chapter), which implies

$$\frac{\partial f_j(\mathbf{v})}{\partial v_j} = 0. \tag{4.6}$$

Defining $\kappa \equiv \sum_{j=1}^{n} \kappa_j \geq 0$, it is clear that (4.5) leads to

$$\delta\Gamma = \delta\Gamma^{[0]}\, \mathrm{e}^{-\kappa t} \quad \text{and} \quad D = D^{[0]}\, \mathrm{e}^{+\kappa t}, \tag{4.7}$$

where $\delta\Gamma^{[0]}$ and $D^{[0]}$ are the values of $\delta\Gamma$ and D at $t = 0$. The relations (4.7) pertain to a phase space volume element which moves along with the points it contains, and the increase in the density of points D is balanced by the decrease in $\delta\Gamma$, so that $\delta n = D\,\delta\Gamma$ remains constant.

If $\nu = \eta = 0$, then $\kappa_j = 0 \rightarrow \kappa = 0$, and the dynamical system is conservative, so that (4.1) represents ideal homogeneous turbulent flow. In this case, equation (4.6) is a critical detail for ensuring that both D and $\delta\Gamma$ remain constant during ideal flow in phase space. The result $D =$ constant is sometimes termed a *detailed Liouville theorem*, to separate it from the Liouville theorem associated with conservative Hamiltonian systems, where Hamilton's canonical equations ensure the constancy of probability density and phase space volume.

It must be emphasized again that 'constant' for a canonical ensemble means 'constant to within small fluctuations.' Thus, the various ideal integral invariants fluctuate slightly about their average values and, for example, the expectation value of fluctuations in energy, *i.e.*, the variance of energy, is $\langle (E - \langle E \rangle)^2 \rangle \neq 0$. The expectation value $\langle Q \rangle$ of any phase function Q is defined as

$$\langle Q \rangle \equiv \int Q\, D\, d\Gamma. \tag{4.8}$$

Here, the integration is over the whole of phase space $-\infty < v_j < +\infty$ and D is normalized so that $\langle 1 \rangle = 1$. Expectation values will be more fully developed in the following sections.

4.4 Canonical Probability Density

The canonical probability density function (PDF) D is a phase function, that is, a function of the phase variables v_j in the phase space Γ. The result that D is constant (again, to within canonical fluctuations) for ideal flow means that D is itself a function of other constants of the motion, *i.e.*, the ideal invariants. Furthermore, for any system, the phase space can generally be decomposed into a Cartesian product of subspaces:

$$\begin{aligned} \Gamma &= \Gamma^{(1)} \otimes \Gamma^{(2)} \\ \mathbf{v} &= \mathbf{v}^{(1)} \otimes \mathbf{v}^{(2)}, \quad \mathbf{v} \in \Gamma,\ \mathbf{v}^{(1)} \in \Gamma^{(1)},\ \mathbf{v}^{(2)} \in \Gamma^{(2)}. \end{aligned} \tag{4.9}$$

(It is possible that $\Gamma^{(1)}$ and $\Gamma^{(2)}$ may be further decomposed, the process continuing until some maximal irreducible set of product subspaces is reached.) Each subspace $\Gamma^{(i)},\ i = 1, 2$, will then have its own statistical distribution function $D^{(i)},\ i = 1, 2$, such that

$$D \;=\; D^{(1)} D^{(2)}. \tag{4.10}$$

This relation holds whether or not the separate variables in $\Gamma^{(1)}$ and $\Gamma^{(2)}$ interact.

If the $\Gamma^{(i)},\ i = 1, 2$, did not interact with one another, the $D^{(i)},\ i = 1, 2$, will each be constant functions of ideal invariants pertaining only to their variables, *i.e.*, their inherent summations will be restricted to the smaller set of variables found in either $\Gamma^{(1)}$ or $\Gamma^{(2)}$, rather than the whole set found in Γ. However, if the $\Gamma^{(i)}$ do interact to form a quasi-closed system, this will reach equilibrium and D will be a constant function of the ideal invariants associated with the whole phase space Γ, although the $D^{(i)},\ i = 1, 2$, will individually no longer be constants of the motion.

To illustrate this point, consider 3-D Euler turbulence, where the invariants are energy $E = E_K$ (3.76) and kinetic helicity H_K (3.81). In this case, we can form the $\Gamma^{(i)},\ i = 1, 2$, by choosing two disjoint sets of wave vectors $\mathbf{k}$. Let $\mathcal{K}$ be the following set:

$$\mathcal{K} \;=\; \{\mathbf{k} \,|\, k_{min} \le k \le k_{max}\}, \tag{4.11}$$

and from this choose two subsets $\mathcal{K}^{(i)},\ i = 1, 2$, such that

$$\mathcal{K} = \mathcal{K}^{(1)} \cup \mathcal{K}^{(2)} \quad \text{and} \quad \mathcal{K}^{(1)} \cap \mathcal{K}^{(2)} = \emptyset. \tag{4.12}$$

Usually the choice $k_{min} = 1$ is made, but other values can also be chosen. (Note that $k_{min} = 1$ rather than $k_{min} = 0$ is used since all modes associated with $\mathbf{k} = 0$ do not dynamically evolve, as the results in the previous chapter show. They are always initialized with zero value and retain this value during a numerical simulation.)

As a specific example, since each $\mathbf{k}$ has integer coefficients, two subsets that tend to equal size in the limit of large k_{max} and which satisfy (4.12) are

$$\begin{aligned} \mathcal{K}^{(1)} &= \{\mathbf{k} \,|\, k_{min} \le k \le k_{max},\ k^2 \text{ is odd}\} \\ \mathcal{K}^{(2)} &= \{\mathbf{k} \,|\, k_{min} \le k \le k_{max},\ k^2 \text{ is even}\}. \end{aligned} \tag{4.13}$$

Other examples can be devised, with the only requirement being that the Fourier modes associated with a given subset may be dynamically coupled to each other, but can be dynamically decoupled from those associated with the other subset. The example embodied in (4.13) has some interesting features, as will be discussed in the next chapter.

The variables in $\Gamma^{(i)},\ i = 1, 2$, are the independent components of $\tilde{\mathbf{u}}(\mathbf{k}), \mathbf{k} \in \mathcal{K}^{(i)},\ i = 1, 2$. For 3-D Euler turbulence, the energies and helicities associated with Γ and the $\Gamma^{(i)},\ i = 1, 2$, are

$$\begin{aligned} E = E^{(1)} + E^{(2)}, \qquad & E^{(i)} = \frac{1}{2} \sum_{\mathbf{k} \in \mathcal{K}^{(i)}} |\tilde{\mathbf{u}}(\mathbf{k})|^2, \quad i = 1, 2 \\ H_K = H_K^{(1)} + H_K^{(2)}, \qquad & H_K^{(i)} = \frac{1}{2} \sum_{\mathbf{k} \in \mathcal{K}^{(i)}} \tilde{\mathbf{u}}^*(\mathbf{k}) \cdot \tilde{\boldsymbol{\omega}}(\mathbf{k}), \quad i = 1, 2. \end{aligned} \tag{4.14}$$

(All three components of $\tilde{\mathbf{u}}(\mathbf{k})$ and $\tilde{\boldsymbol{\omega}}(\mathbf{k})$ are included in the sums above, not just the independent ones.) The sets $\mathcal{K}$ and $\mathcal{K}^{(i)}$, defined by (4.11), (4.12) and (4.13), contain modes $\mathbf{k} \sim -\mathbf{k}$ which are equivalent because of the reality condition (3.14). To reduce this redundancy, define

$$\begin{aligned} \mathcal{K}' &= \{\mathbf{k} \,|\, \mathbf{k} \in \mathcal{K},\ \mathbf{k} \cdot \hat{\mathbf{x}}' \geq 0\} \\ \mathcal{K}'^{(i)} &= \left\{\mathbf{k} \,|\, \mathbf{k} \in \mathcal{K}^{(i)},\ \mathbf{k} \cdot \hat{\mathbf{x}}' \geq 0\right\},\ i = 1, 2 \\ \hat{\mathbf{x}}' &= \hat{\mathbf{x}} - (2k_{max})^{-1}(\hat{\mathbf{y}} + \hat{\mathbf{z}}). \end{aligned} \tag{4.15}$$

Thus, $\mathcal{K}'$ and $\mathcal{K}'^{(i)}$ have half the members of $\mathcal{K}$ and $\mathcal{K}^{(i)}$, respectively. Using these results, (4.14) becomes

$$E^{(i)} = \sum_{\mathbf{k} \in \mathcal{K}'^{(i)}} |\tilde{\mathbf{u}}(\mathbf{k})|^2 \quad \text{and} \quad H_K^{(i)} = \sum_{\mathbf{k} \in \mathcal{K}'^{(i)}} \tilde{\mathbf{u}}^*(\mathbf{k}) \cdot \tilde{\boldsymbol{\omega}}(\mathbf{k}), \quad i = 1, 2. \tag{4.16}$$

The factor of $\frac{1}{2}$ appears in front of the sums (4.14) because these count twice every term in the sums (4.16).

Since the canonical probability densities are functions of the ideal invariants, the only nontrivial functions which satisfy (4.10) when $\Gamma^{(1)}$ and $\Gamma^{(2)}$ are in equilibrium are

$$\begin{aligned} D &= \frac{1}{Z} \exp\left(-\alpha E - \beta H_K\right) \\ D^{(i)} &= \frac{1}{Z^{(i)}} \exp\left[-\alpha E^{(i)} - \beta H_K^{(i)}\right],\ \ i = 1, 2. \end{aligned} \tag{4.17}$$

The normalizing functions Z and $Z^{(i)}$ are called *partition functions*:

$$\begin{aligned} Z &= \int \exp\left(-\alpha E - \beta H_K\right)\, d\Gamma \\ Z^{(i)} &= \int \exp\left(-\alpha E^{(i)} - \beta H_K^{(i)}\right)\, d\Gamma^{(i)}. \end{aligned} \tag{4.18}$$

In (4.17) and (4.18) the parameters α and β are not phase functions, but instead are *undetermined multipliers*, or as they are often called, *inverse temperatures*. Terms such as $\gamma\, \mathbf{k} \cdot \tilde{\mathbf{u}}_R(\mathbf{k})$ are not included in (4.18) because these are zero to within small fluctuations. Also, the phase volume elements in (4.18) are

$$d\Gamma = \prod_i d\Gamma^{(i)}, \quad d\Gamma^{(i)} = \prod_{\mathbf{k} \in \mathcal{K}'^{(i)}} d\Gamma(\mathbf{k}), \quad d\Gamma(\mathbf{k}) = d\tilde{\mathbf{u}}_R(\mathbf{k})\, d\tilde{\mathbf{u}}_I(\mathbf{k}). \tag{4.19}$$

There are analogous expressions to (4.19) for the other five cases of ideal homogeneous turbulence. (The modal subspaces $\Gamma(\mathbf{k})$ for the different cases of ideal turbulence are explicitly identified in Table 4.2.)

If the $\Gamma^{(i)}$ are isolated from one another, then each will have different inverse temperatures $\alpha^{(i)}$ and $\beta^{(i)}$. In this case $D^{(i)}$ and $Z^{(i)}$ will have the form

$$\begin{aligned} D^{(i)} &= \frac{1}{Z^{(i)}} \exp\left[-\alpha^{(i)} E^{(i)} - \beta^{(i)} H_K^{(i)}\right], \quad i = 1, 2. \\ Z^{(i)} &= \int \exp\left(-\alpha^{(i)} E^{(i)} - \beta^{(i)} H_K^{(i)}\right) d\Gamma^{(i)}. \end{aligned} \tag{4.20}$$

Here, in general, $\alpha^{(1)} \neq \alpha^{(2)}$ and $\beta^{(1)} \neq \beta^{(2)}$. However, if the $\Gamma^{(i)}$ are dynamically connected, then they will both equilibrate to the same 'temperatures,' α and β, returning them to the forms (4.17) and (4.18).

It has been stated that the canonical invariants, such as E and H_K, fluctuate about average values and are constant only in a probabilistic sense, *i.e.*, the fluctuations are relatively small. The probability densities appearing in (4.17) (and their analogous forms for the other five cases of ideal homogeneous turbulence) provide a way to give this statement precise meaning. Canonical probability densities will, in fact, be highly peaked at the average values of the integral invariants, but it must be noted that E and H_K within the exponentials of (4.17) can take essentially unbounded values within Γ.

Also, in looking at (4.17), we see a general and very useful feature of the canonical probability densities of ideal homogeneous turbulence: They are all essentially Gaussian probability distributions, *i.e.*, the arguments of the exponentials can always be put (through coordinate transformations, if necessary) into the form of negative definite (because of the minus sign) symmetric quadratic forms. This fact makes calculation of the expectation values of moments of the variables of Γ a straightforward procedure, as will be seen presently.

4.5 Partition Functions

$$Z = \int \exp\left(-\alpha I_1 - \beta I_2 - \gamma I_3\right) d\Gamma$$

Case	B_o	I_1	I_2	I_3
2-D Euler	–	E	Ω	0
3-D Euler	–	E	H_K	0
2-D MHD	0	E	H_C	A
2-D MHD	1	E	H_C	0
3-D MHD	0	E	H_C	H_M
3-D MHD	1	E	H_C	0

Table 4.1: General form of partition functions.

In the last chapter the evolution equations and ideal invariants of the six basic cases of ideal homogeneous turbulence were presented. Here, the six cases, their ideal invariants, and the general form of their partition functions are given in Table 4.1. In order to demonstrate the evaluation of the general integral of a partition function, consider, once again, the 3-D Euler case:

$$Z = \int \exp\left(-\alpha E - \beta H_K\right) d\Gamma = \prod_{\mathbf{k}\in\mathcal{K}'} Z(\mathbf{k}), \tag{4.21}$$

where the *modal partition function* $Z(\mathbf{k})$ is

$$\begin{aligned} Z(\mathbf{k}) &= \int \exp\left[-\alpha|\tilde{\mathbf{u}}(\mathbf{k})|^2 - i\beta\tilde{\mathbf{u}}^*(\mathbf{k})\cdot\mathbf{k}\times\tilde{\mathbf{u}}(\mathbf{k})\right] d\Gamma(\mathbf{k}) \\ &= \int \exp\left[-A(\mathbf{k})\right] d\Gamma(\mathbf{k}), \end{aligned} \tag{4.22}$$

and the modal six-dimensional volume element $d\Gamma(\mathbf{k})$ is given by (4.19). Also, recall that each variable in (4.22) is evaluated from $-\infty$ to $+\infty$.

Expanding $\tilde{\mathbf{u}}(\mathbf{k})$ explicitly into real and imaginary parts and the argument $A(\mathbf{k})$ in (4.22) becomes

$$\begin{aligned} A(\mathbf{k}) &= \alpha|\tilde{\mathbf{u}}(\mathbf{k})|^2 + \beta\tilde{\mathbf{u}}^*(\mathbf{k})\cdot\tilde{\boldsymbol{\omega}}(\mathbf{k}) \\ &= \alpha\left[|\tilde{\mathbf{u}}_R(\mathbf{k})|^2 + |\tilde{\mathbf{u}}_I(\mathbf{k})|^2\right] + 2\beta\tilde{\mathbf{u}}_I(\mathbf{k})\cdot\mathbf{k}\times\tilde{\mathbf{u}}_R(\mathbf{k}). \end{aligned} \tag{4.23}$$

The integral in (4.22) can be evaluated by either the coordinate transformation

$$\tilde{\mathbf{u}}'_I(\mathbf{k}) = \tilde{\mathbf{u}}_I(\mathbf{k}) + \frac{\beta}{\alpha}\mathbf{k}\times\tilde{\mathbf{u}}_R(\mathbf{k}), \tag{4.24}$$

or the alternative one

$$\tilde{\mathbf{u}}'_R(\mathbf{k}) = \tilde{\mathbf{u}}_R(\mathbf{k}) - \frac{\beta}{\alpha}\mathbf{k}\times\tilde{\mathbf{u}}_I(\mathbf{k}). \tag{4.25}$$

Upon using the transformation (4.24) on (4.23), the integral in (4.22) becomes

$$Z(\mathbf{k}) = \int \exp\left[-\frac{\alpha^2-\beta^2k^2}{\alpha}|\tilde{\mathbf{u}}_R(\mathbf{k})|^2 - \alpha|\tilde{\mathbf{u}}'_I(\mathbf{k})|^2\right] d\Gamma'(\mathbf{k}). \tag{4.26}$$

Here, $d\Gamma'(\mathbf{k}) = d\tilde{\mathbf{u}}_R(\mathbf{k})\, d\tilde{\mathbf{u}}'_I(\mathbf{k})$. [Using (4.25) would merely have switched the subscripts $R \rightleftharpoons I$ in the $d\Gamma'(\mathbf{k})$.]

In order to evaluate (4.26), the parameters α and β must satisfy the following inequalities:

$$\alpha > 0, \qquad \alpha^2 > \beta^2 k_{max}^2. \tag{4.27}$$

Provided these inequalities are met, using the well known result

$$\mathcal{I}(a) \;=\; \int_{-\infty}^{\infty} \exp\left(-ax^2\right)\, dx \;=\; \sqrt{\frac{\pi}{a}} \tag{4.28}$$

produces

$$Z(\mathbf{k}) \;=\; \pi^3 \left(\alpha^2 - \beta^2 k^2\right)^{-3/2}. \tag{4.29}$$

Note that although we have found $Z(\mathbf{k})$, and thus Z by (4.21), the quantities α and β are still undetermined, though (4.27) limits their values. Also, note that the two coordinate transformations (4.24) and (4.25) show that D is essentially a Gaussian distribution function on the variables $\tilde{\mathbf{u}}'_R(\mathbf{k})$ and $\tilde{\mathbf{u}}'_I(\mathbf{k})$.

The modal distribution functions for the other cases of ideal homogeneous turbulence listed in Table 4.1 can be found in the same way as the 3-D Euler case just considered. The results of doing so are given in Table 4.2. In this Table, the six separate cases are listed, as well as their associated phase variables and modal distribution functions. Using these results in the next section will allow us to find various expectation values, since the $Z(\mathbf{k})$ normalize their associated canonical probability densities.

4.6 PDFs for Ideal Turbulence

The canonical probability density function D that gives the expected phase space distribution of phase points is

$$\begin{aligned} D \;&=\; \prod_{\mathbf{k}\in\mathcal{K}'} D(\mathbf{k}), \qquad I_i \;=\; \sum_{\mathbf{k}\in\mathcal{K}'} I_i(\mathbf{k}), \quad i = 1,2,3 \\ D(\mathbf{k}) \;&=\; \frac{1}{Z(\mathbf{k})} \int \exp\left[-\alpha I_1(\mathbf{k}) - \beta I_2(\mathbf{k}) - \gamma I_3(\mathbf{k})\right] d\Gamma(\mathbf{k}). \end{aligned} \tag{4.30}$$

The modal partition functions $Z(\mathbf{k})$ are given in Table 4.2 and the modal terms $I_j(\mathbf{k})$, $j = 1,2,3$, are given in Table 4.3. These will be used in the next section to determine expectation values of moments of phase space variables.

4.7 Expectation Values

Now, we move on to determining expectation values (4.8) for moments of the components of $\tilde{\mathbf{u}}_R(\mathbf{k})$, $\tilde{\mathbf{u}}_I(\mathbf{k})$, $\tilde{\mathbf{b}}_R(\mathbf{k})$ and $\tilde{\mathbf{b}}_I(\mathbf{k})$. In what follows, the expectation values apply to those components that are kinematically nonzero. To be more explicit, when $\mathbf{k}_x = k_x\hat{\mathbf{x}}$ or $\mathbf{k}_y = k_y\hat{\mathbf{y}}$ or $\mathbf{k}_z = k_z\hat{\mathbf{z}}$ (*i.e.*, only one component of $\mathbf{k}$ is nonzero), then solenoidality leads to $\tilde{u}_j(\mathbf{k}_j) = \tilde{b}_j(\mathbf{k}_j) = 0$, $j = x,y,z$ for all t. In these cases all expectation values are zero; in all other case, they are as given below.

$Z(\mathbf{k}) = f(k, \alpha, \beta, \gamma)$				
Case	B_o	$\Gamma(\mathbf{k})$	$Z(\mathbf{k})$	$\alpha,\ \beta,\ \gamma\ \left(\delta^2 = \alpha^2 - \frac{1}{4}\beta^2\right)$
2-D Euler	–	$\tilde{\omega}_{R,I}(\mathbf{k})$	$\dfrac{\pi}{\alpha/k^2 + \beta}$	$\alpha > 0,\ \beta > -\alpha/k^2_{max}$ $\alpha < 0,\ \beta > -\alpha/k^2_{min}$
3-D Euler	–	$\tilde{\mathbf{u}}_{R,I}(\mathbf{k})$	$\dfrac{\pi^3}{(\alpha^2 - \beta^2 k^2)^{\frac{3}{2}}}$	$\alpha > 0,\ \lvert\beta\rvert < \alpha/k_{max}$
2-D MHD	0	$\tilde{\omega}_{R,I}(\mathbf{k})$ $\tilde{a}_{R,I}(\mathbf{k})$	$\dfrac{\pi^2}{\delta^2 + \alpha\gamma/k^2}$	$\alpha > 0$ $\gamma > 0,\ \delta^2 > -\alpha\gamma/k^2_{max}$ $\gamma < 0,\ \delta^2 > -\alpha\gamma/k^2_{min}$
2-D MHD	1	$\tilde{\omega}_{R,I}(\mathbf{k})$ $\tilde{a}_{R,I}(\mathbf{k})$	$\dfrac{\pi^2}{\delta^2}$	$\alpha > 0,\ \delta^2 > 0$ $\gamma = 0$
3-D MHD	0	$\tilde{\mathbf{u}}_{R,I}(\mathbf{k})$ $\tilde{\mathbf{b}}_{R,I}(\mathbf{k})$	$\dfrac{\pi^6}{(\delta^4 - \alpha^2\gamma^2/k^2)^{\frac{3}{2}}}$	$\alpha > 0,\ \delta^2 > 0$ $\lvert\gamma\rvert < k_{min}\delta^2/\alpha$
3-D MHD	1	$\tilde{\mathbf{u}}_{R,I}(\mathbf{k})$ $\tilde{\mathbf{b}}_{R,I}(\mathbf{k})$	$\dfrac{\pi^6}{\delta^6}$	$\alpha > 0,\ \delta^2 > 0$ $\gamma = 0$

Table 4.2: Modal partition functions for ideal turbulence.

$$D(\mathbf{k}) = Z^{-1}(\mathbf{k}) \exp\left[-\alpha I_1(\mathbf{k}) - \beta I_2(\mathbf{k}) - \gamma I_3(\mathbf{k})\right]$$

Case	$I_1(\mathbf{k})$	$I_2(\mathbf{k})$	$I_3(\mathbf{k})$
2-D Euler	$k^{-2}\lvert\tilde{\omega}_R(\mathbf{k})\rvert^2 + k^{-2}\lvert\tilde{\omega}_I(\mathbf{k})\rvert^2$	$\lvert\tilde{\omega}_R(\mathbf{k})\rvert^2 + \lvert\tilde{\omega}_I(\mathbf{k})\rvert^2$	0
3-D Euler	$\lvert\tilde{\mathbf{u}}_R(\mathbf{k})\rvert^2 + \lvert\tilde{\mathbf{u}}_I(\mathbf{k})\rvert^2$	$2\mathbf{k} \cdot \tilde{\mathbf{u}}_R(\mathbf{k}) \times \tilde{\mathbf{u}}_I(\mathbf{k})$	0
2-D MHD†	$k^{-2}\lvert\tilde{\omega}_R(\mathbf{k})\rvert^2 + k^{-2}\lvert\tilde{\omega}_I(\mathbf{k})\rvert^2 + k^2\lvert\tilde{a}_R(\mathbf{k})\rvert^2 + k^2\lvert\tilde{a}_I(\mathbf{k})\rvert^2$	$\tilde{\omega}_R(\mathbf{k})\,\tilde{a}_R(\mathbf{k}) + \tilde{\omega}_I(\mathbf{k})\,\tilde{a}_I(\mathbf{k})$	$\lvert\tilde{a}_R(\mathbf{k})\rvert^2 + \lvert\tilde{a}_I(\mathbf{k})\rvert^2$
3-D MHD†	$\lvert\tilde{\mathbf{u}}_R(\mathbf{k})\rvert^2 + \lvert\tilde{\mathbf{u}}_I(\mathbf{k})\rvert^2 + \lvert\tilde{\mathbf{b}}_R(\mathbf{k})\rvert^2 + \lvert\tilde{\mathbf{b}}_I(\mathbf{k})\rvert^2$	$\tilde{\mathbf{u}}_R(\mathbf{k}) \cdot \tilde{\mathbf{b}}_R(\mathbf{k}) + \tilde{\mathbf{u}}_I(\mathbf{k}) \cdot \tilde{\mathbf{b}}_I(\mathbf{k})$	$2\mathbf{k} \cdot \tilde{\mathbf{a}}_R(\mathbf{k}) \times \tilde{\mathbf{a}}_I(\mathbf{k})$

†When $B_o = 1$, $\gamma \equiv 0$.

Table 4.3: Modal density functions for ideal turbulence.

First, we note that the following integrals of an odd integrand between symmetric limits are zero:

$$\mathcal{I}_{2n-1}(a) = \int_{-\infty}^{\infty} x^{2n-1} \exp\left(-ax^2\right) dx = 0, \quad n = 1, 2, 3, \ldots. \tag{4.31}$$

Similar integrals of even powers of x are nonzero, however, and can be found from (4.28):

$$\begin{aligned} \mathcal{I}_{2n}(a) &= \int_{-\infty}^{\infty} x^{2n} \exp\left(-ax^2\right) dx \\ &= \left(-\frac{d}{da}\right)^n \mathcal{I}(a) \\ &= \frac{(2n-1)!!}{(2a)^n}\mathcal{I}(a), \quad n = 1, 2, 3, \ldots. \end{aligned} \tag{4.32}$$

In terms of (4.28) and (4.32), the expectation value of an even power of a variable with a

Gaussian distribution function is

$$\left\langle x^{2n} \right\rangle = \frac{\mathcal{I}_{2n}(a)}{\mathcal{I}(a)} = \frac{(2n-1)!!}{(2a)^n}, \quad n = 1, 2, 3, \ldots. \tag{4.33}$$

In particular, for $n = 1$, (4.33) gives

$$\left\langle x^2 \right\rangle = \frac{\mathcal{I}_2(a)}{\mathcal{I}(a)} = \frac{1}{2a}, \tag{4.34}$$

while for $n > 1$, we have

$$\left\langle x^{2n} \right\rangle = (2n-1)!! \left\langle x^2 \right\rangle^n. \tag{4.35}$$

Thus, knowledge of $\langle x^2 \rangle$ gives knowledge of all the nonzero moments $\langle x^{2n} \rangle$, thereby completely determining the statistics of x, which is a well known result for Gaussian distributions.

The expectation values of powers of the phase variables can now be calculated for the six cases of ideal homogeneous turbulence using the general form

$$\begin{aligned} \langle \tilde{u}^m(\mathbf{k}) \rangle &= \int \tilde{u}^m(\mathbf{k})\, D\, d\Gamma \\ &= \int \tilde{u}^m(\mathbf{k})\, D(\mathbf{k})\, d\Gamma(\mathbf{k}), \end{aligned} \tag{4.36}$$

where the modal canonical probability densities $D(\mathbf{k})$ are defined in (4.30) and given explicitly in Table 4.3. Evaluation of expectation values for the different cases of ideal homogeneous turbulence requires the use of coordinate transformations such as (4.24) and (4.25). Since these expectation values are important, we will look at them in detail. The general form of the probability densities is

$$\begin{aligned} D(\mathbf{k}) &= \frac{1}{Z(\mathbf{k})} \exp\left[-A(\mathbf{k})\right] \\ A(\mathbf{k}) &= \alpha I_1(\mathbf{k}) + \beta I_2(\mathbf{k}) + \gamma I_3(\mathbf{k}). \end{aligned} \tag{4.37}$$

The values of $I_i(\mathbf{k})$, $i = 1, 2, 3$, for the different cases are given in Table 4.3.

4.7.1 2-D Euler

In the 2-D Euler case, the modal argument in (4.37) is summation over the real and imaginary parts of a modal variable:

$$\begin{aligned} A(\mathbf{k}) &= \sum_{S=R,I} \left[\alpha \tilde{\omega}_S^2(\mathbf{k})/k^2 + \beta \tilde{\omega}_S^2(\mathbf{k})\right] \\ &= \sum_{S=R,I} \left(\alpha/k^2 + \beta\right) \tilde{\omega}_S^2(\mathbf{k}). \end{aligned} \tag{4.38}$$

If we put the following into (4.31) and (4.34),

$$x = \tilde{\omega}_S(\mathbf{k}), \qquad a = \alpha/k^2 + \beta, \tag{4.39}$$

we easily determine

$$\langle \tilde{\omega}_S(\mathbf{k}) \rangle = 0, \qquad \left\langle \tilde{\omega}_S^2(\mathbf{k}) \right\rangle = \frac{k^2}{2\left(\alpha + \beta k^2\right)}, \qquad S = R, I. \tag{4.40}$$

Expectation values of higher even powers can be generated using (4.33).

4.7.2 3-D Euler

In the 3-D Euler case, the modal argument in (4.37) is given by (4.23), after applying the transformation (4.24):

$$\begin{aligned} A(\mathbf{k}) &= \alpha \left[|\tilde{\mathbf{u}}_R(\mathbf{k})|^2 + |\tilde{\mathbf{u}}_I(\mathbf{k})|^2 \right] + 2\beta \tilde{\mathbf{u}}_I(\mathbf{k}) \cdot \mathbf{k} \times \tilde{\mathbf{u}}_R(\mathbf{k}) \\ &= \alpha^{-1} \left(\alpha^2 - \beta^2 k^2 \right) |\tilde{\mathbf{u}}_R(\mathbf{k})|^2 + \alpha |\tilde{\mathbf{u}}_I'(\mathbf{k})|^2. \end{aligned} \tag{4.41}$$

As was noted earlier, (4.25) can be used instead of (4.24), which merely switches R and I in (4.41). Thus, using these results, along with (4.31), (4.34) and (4.37) gives

$$\begin{aligned} \langle \tilde{u}_{S,i}(\mathbf{k}) \rangle &= 0, \quad S = R, I, \quad i = x, y, z, \\ \left\langle \tilde{u}_{S,i}^2(\mathbf{k}) \right\rangle &= \frac{\alpha}{2\left(\alpha^2 - \beta^2 k^2\right)}. \end{aligned} \tag{4.42}$$

Since (4.41) also gives

$$\left\langle \tilde{u}_{I,i}'(\mathbf{k})\, \tilde{u}_{I,i}'(\mathbf{k}) \right\rangle = \frac{1}{2\alpha}, \quad i = x, y, z, \tag{4.43}$$

we can use (4.24), along with our ability to interchange R and I, to show

$$\langle \tilde{u}_{S,i}(\mathbf{k})\, \tilde{\omega}_{S,i}(\mathbf{k}) \rangle = \frac{-\beta k^2}{2\left(\alpha^2 - \beta^2 k^2\right)}, \quad S = R, I, \quad i = x, y, z. \tag{4.44}$$

4.7.3 2-D MHD

In the 2-D MHD case, the modal argument in (4.37) is

$$A(\mathbf{k}) = \sum_{S=R,I} \left\{ \alpha \left[k^{-2} \tilde{\omega}_S^2(\mathbf{k}) + k^2 \tilde{a}_S^2(\mathbf{k}) \right] + \beta \tilde{\omega}_S(\mathbf{k}) \tilde{a}_S(\mathbf{k}) + \gamma \tilde{a}_S^2(\mathbf{k}) \right\}$$

$$
\begin{aligned}
&= \sum_{S=R,I} \left[\frac{\alpha}{k^2} \tilde{\omega}_S^2(\mathbf{k}) + \beta \tilde{\omega}_S(\mathbf{k}) \tilde{a}_S(\mathbf{k}) + \left(\alpha k^2 + \gamma \right) \tilde{a}_S^2(\mathbf{k}) \right] \\
&= \sum_{S=R,I} \left[\frac{\alpha}{k^2} \tilde{\omega}_S'^2(\mathbf{k}) + \left(\frac{\delta^2}{\alpha} k^2 + \gamma \right) \tilde{a}_S^2(\mathbf{k}) \right] \\
&= \sum_{S=R,I} \left[\left(\frac{\delta^2 + \alpha\gamma/k^2}{\alpha k^2 + \gamma} \right) \tilde{\omega}_S^2(\mathbf{k}) + \left(\alpha k^2 + \gamma \right) \tilde{a}_S'^2(\mathbf{k}) \right]. \qquad (4.45)
\end{aligned}
$$

Here we have introduced $\delta^2 = \alpha^2 - \frac{1}{4}\beta^2$ for brevity. In (4.45), the two transformed variables are

$$
\begin{aligned}
\tilde{\omega}_S'(\mathbf{k}) &= \tilde{\omega}_S(\mathbf{k}) + \frac{\beta k^2}{2\alpha} \tilde{a}_S(\mathbf{k}), \quad S = R, I \\
\tilde{a}_S'(\mathbf{k}) &= \tilde{a}_S(\mathbf{k}) + \frac{\beta k^2}{2(\alpha k^2 + \gamma)} \tilde{\omega}_S(\mathbf{k}). \qquad (4.46)
\end{aligned}
$$

From these results, it is a straightforward matter to deduce the following expectation values:

$$
\begin{aligned}
\langle \tilde{\omega}_S(\mathbf{k}) \rangle &= \langle \tilde{a}_S(\mathbf{k}) \rangle = 0, \qquad S = R, I \\
\left\langle \tilde{\omega}_S^2(\mathbf{k}) \right\rangle &= \frac{\alpha k^2 + \gamma}{2\left(\delta^2 + \alpha\gamma/k^2\right)} \\
\left\langle \tilde{a}_S^2(\mathbf{k}) \right\rangle &= \frac{\alpha}{2\,k^2\left(\delta^2 + \alpha\gamma/k^2\right)} \\
\langle \tilde{\omega}_S(\mathbf{k}) \tilde{a}_S(\mathbf{k}) \rangle &= -\frac{\beta}{4\left(\delta^2 + \alpha\gamma/k^2\right)}. \qquad (4.47)
\end{aligned}
$$

Again, $\delta^2 = \alpha^2 - \frac{1}{4}\beta^2$. In the case where $B_o = 0$, we have $\gamma \neq 0$, while in the case where $B_o = 1$, we have $\gamma \equiv 0$.

4.7.4 3-D MHD

Finally, in the 3-D MHD case, the modal argument in (4.37) is

$$
\begin{aligned}
A(\mathbf{k}) &= \sum_{S=R,I} \left[\alpha |\tilde{\mathbf{u}}_S(\mathbf{k})|^2 + \alpha |\tilde{\mathbf{b}}_S(\mathbf{k})|^2 + \beta \tilde{\mathbf{u}}_S(\mathbf{k}) \cdot \tilde{\mathbf{b}}_S(\mathbf{k}) \right] \\
&\quad + 2\frac{\gamma}{k^2} \mathbf{k} \cdot \tilde{\mathbf{b}}_R(\mathbf{k}) \times \tilde{\mathbf{b}}_I(\mathbf{k}). \qquad (4.48)
\end{aligned}
$$

There are essentially two ways to transform variables in this argument. The first starts with

$$
\tilde{\mathbf{u}}_S'(\mathbf{k}) = \tilde{\mathbf{u}}_S(\mathbf{k}) + \frac{\beta}{2\alpha} \tilde{\mathbf{b}}_S(\mathbf{k}), \qquad S = R, I, \qquad (4.49)
$$

and then uses either of the following

$$\tilde{\mathbf{b}}'_I(\mathbf{k}) = \tilde{\mathbf{b}}_I(\mathbf{k}) + \frac{\alpha\gamma}{\delta^2 k^2}\mathbf{k}\times\tilde{\mathbf{b}}_R(\mathbf{k}) \tag{4.50}$$

$$\tilde{\mathbf{b}}'_R(\mathbf{k}) = \tilde{\mathbf{b}}_R(\mathbf{k}) - \frac{\alpha\gamma}{\delta^2 k^2}\mathbf{k}\times\tilde{\mathbf{b}}_I(\mathbf{k}). \tag{4.51}$$

Using (4.49) and (4.50) transforms (4.48) into

$$\begin{aligned} A(\mathbf{k}) &= \alpha|\tilde{\mathbf{u}}'_R(\mathbf{k})|^2 + \alpha|\tilde{\mathbf{u}}'_I(\mathbf{k})|^2 \\ &\quad + \frac{\delta^2 - \alpha^2\gamma^2/k^2}{\alpha\delta^2}|\tilde{\mathbf{b}}_R(\mathbf{k})|^2 + \frac{\delta^2}{\alpha}|\tilde{\mathbf{b}}'_I(\mathbf{k})|^2. \end{aligned} \tag{4.52}$$

If (4.51) had been used, R and I would be switched in (4.52).

The second approach uses

$$\tilde{\mathbf{u}}'_I(\mathbf{k}) = \tilde{\mathbf{u}}_I(\mathbf{k}) + \frac{\beta}{2\alpha}\tilde{\mathbf{b}}_R(\mathbf{k}), \tag{4.53}$$

followed by (4.50), and then

$$\tilde{\mathbf{b}}'_R(\mathbf{k}) = \tilde{\mathbf{b}}_R(\mathbf{k}) + \frac{\beta\delta^2}{2\alpha(\delta^2 - \gamma^2/k^2)}\tilde{\mathbf{u}}_R(\mathbf{k}). \tag{4.54}$$

Using these transforms (recalling $\delta^2 = \alpha^2 - \beta^2/4$) turns (4.48) into

$$\begin{aligned} A(\mathbf{k}) &= \frac{\delta^4 - \alpha^2\gamma^2/k^2}{\alpha(\delta^2 - \gamma^2/k^2)}|\tilde{\mathbf{u}}_R(\mathbf{k})|^2 + \alpha|\tilde{\mathbf{u}}'_I(\mathbf{k})|^2 \\ &\quad + \frac{\alpha(\delta^2 - \gamma^2/k^2)}{\delta^2}|\tilde{\mathbf{b}}'_R(\mathbf{k})|^2 + \frac{\delta^2}{\alpha}|\tilde{\mathbf{b}}'_I(\mathbf{k})|^2. \end{aligned} \tag{4.55}$$

A similar set of transformations would produce an equation identical to (4.55), but with R and I switched.

The expectation values for the 3-D MHD case are thus:

$$\langle\tilde{\mathbf{u}}_S(\mathbf{k})\rangle = \left\langle\tilde{\mathbf{b}}_S(\mathbf{k})\right\rangle = 0, \qquad S = R, I$$

$$\begin{aligned} \left\langle\tilde{\mathbf{u}}_S^2(\mathbf{k})\right\rangle &= \frac{3}{2}\frac{\alpha(\delta^2 - \gamma^2/k^2)}{\delta^4 - \alpha^2\gamma^2/k^2} \\ \left\langle|\tilde{\mathbf{b}}_S(\mathbf{k})|^2\right\rangle &= \frac{3}{2}\frac{\alpha\delta^2}{\delta^4 - \alpha^2\gamma^2/k^2} \\ \left\langle\tilde{\mathbf{u}}_S(\mathbf{k})\cdot\tilde{\mathbf{b}}_S(\mathbf{k})\right\rangle &= -\frac{3}{4}\frac{\beta\delta^2}{\delta^4 - \alpha^2\gamma^2/k^2} \\ \left\langle\tilde{\mathbf{a}}_S(\mathbf{k})\cdot\tilde{\mathbf{b}}_S(\mathbf{k})\right\rangle &= -\frac{3}{2}\frac{\alpha^2\gamma/k^2}{\delta^4 - \alpha^2\gamma^2/k^2}. \end{aligned} \tag{4.56}$$

Once again, $\delta^2 = \alpha^2 - \frac{1}{4}\beta^2$. In the case where $B_o = 0$, we have $\gamma \neq 0$, and in the case where $B_o = 1$, we have $\gamma = 0$. The factor of 3 appears in these results because $\tilde{\mathbf{u}}(\mathbf{k})$ and $\tilde{\mathbf{b}}(\mathbf{k})$ are 3-vectors, whose three components all add equally to (4.56).

4.8 References for Further Reading

One good reference on dynamical systems is [Verhulst 96].

Microcanonical and canonical emsembles are discussed in [Khinchin 49] and [Landau 80].

That a detailed Liouville theorem exists for ideal turbulence was discovered by [Lee 52]. Initial applications of canonical ensemble theory to the six cases of ideal turbulence were: 2-D Euler [Kraichnan 75]; 3-D Euler [Moffatt 69, Kraichnan 73]; 2-D MHD ($B_o = 0$) [Fyfe 76], ($B_o = 1$) [Shebalin 83]; and 3-D MHD ($B_o = 0$) [Frisch 75], ($B_o = 1$) [Shebalin 89, Shebalin 94]. A good review article on 2-D turbulence, including some discussion on ideal 2-D Euler and MHD turbulence ($B_o = 0$) is [Kraichnan 80].

Chapter 5

Thermodynamics

Canonical ensemble theory, as it applies to ideal homogeneous turbulence, was discussed in the previous chapter and allowed us to determine the statistical mechanics of an interacting system of Fourier modes. In fact, the independent Fourier modes, denoted by unique wave vectors $\mathbf{k} \in \mathcal{K}'$ (see eq. 4.15), form the set of 'molecules' of the interacting system, in analogy with the individually numbered real molecules of a Maxwellian gas. A gas molecule has its own set of associated variables; *e.g.*, in a polyatomic gas, each molecule has its own momentum and angular momentum, each vector having three components, for a total six variables (neglecting vibration). This defines a 6-D subspace in the phase space of the Maxwellian polyatomic gas. The modal subspaces of ideal turbulence are defined in exactly the same way, so that the modal subspaces $\Gamma(\mathbf{k})$ in the different cases of ideal turbulence have their own characteristic dimension (though not all dimensions are independent):

$$m \;=\; \dim \Gamma(\mathbf{k}). \tag{5.1}$$

For the different cases, the modal variables are listed in Table 4.2 and give, for the different cases of ideal turbulence, $m = 2$ for 2-D Euler, $m = 4$ for 2-D MHD, $m = 6$ for 3-D Euler, and $m = 12$ for 3-D MHD. Thus, each Fourier mode is a 'molecule' with m degrees of freedom.

Furthermore, knowledge of the invariant quantities for the different cases, as summarized in Table 4.1, enabled us to find the corresponding canonical probability densities and use these to determine expectation values for the moments of the modal subspace variables. This is the essential product of the statistical approach – 'microscopic' quantities, *i.e.*, modal expectation values. What we wish to do now is move on to look at 'macroscopic' quantities, such as the inverse temperatures α, β and γ (which are heretofore undetermined). These macroscopic quantities pertain to all modes and are, in fact, found by summing over all independent modes $\mathbf{k}$. This summation over all modes moves us from the realm of statistical mechanics into the realm of *thermodynamics*, where we are no longer concerned with specific modes, but instead with summations over all modes. These summations produce *thermodynamic functions* that will have specific values for the closed system of interacting Fourier modes.

Thus, in analogy with the theory of a molecular gas, we move from a statistical description to a thermodynamic one. To maintain the analogy, we must ensure that analogous 'laws of thermodynamics' are present in our model system. The first law is conservation of energy, and this is always a invariant for ideal turbulence. The second law, *i.e.*, that entropy never decreases after an interaction, will be established in this chapter for ideal turbulence. (The third law, the vanishing of entropy as temperature goes to zero, is quantum mechanical, and not applicable here.) To begin the process, we first discuss temperature (or rather *inverse* temperatures).

5.1 Inverse Temperatures

We have already encountered several thermodynamic functions, namely, the energy, enstrophy, mean square vector potential, and the various helicities. We can introduce others, as required, to facilitate our analysis. All of these thermodynamic functions will have expectation values for the system under consideration, which can be determined in the established manner. Some of these functions, in particular the invariants already identified, will have essentially constant values as the associated system evolves with time, while others, known to vary with time, will nonetheless also have specific expectation values. The difference between the invariants and the non-invariants is that we can predict the expectation values of the first group, but cannot predict those of the second. *Á priori*, then, we must treat the expectation values of non-invariants as unknown parameters, a role which will turn out, in fact, to be useful. Let us give these preliminary remarks some substance by explicitly considering the different case of ideal homogeneous turbulence.

5.1.1 2-D Euler

In this case, the two functions we have already met are the energy E and the enstrophy Ω:

$$E = \sum_{\mathbf{k}\in\mathcal{K}'} k^{-2} \, |\tilde{\omega}(\mathbf{k})|^2 \tag{5.2}$$

$$\Omega = \sum_{\mathbf{k}\in\mathcal{K}'} |\tilde{\omega}(\mathbf{k})|^2. \tag{5.3}$$

If we take the expectation values of the above, and use the modal results given in (4.40), we get

$$\langle E \rangle = \mathcal{E} = \sum_{\mathbf{k}\in\mathcal{K}'} \frac{1}{\alpha + \beta k^2} \tag{5.4}$$

$$\langle \Omega \rangle = \Omega = \sum_{\mathbf{k}\in\mathcal{K}'} \frac{k^2}{\alpha + \beta k^2}. \tag{5.5}$$

Thus, we see that the inverse temperatures α and β are implicit functions of $\mathcal{E}$ and Ω. While these two equations can be solved numerically, the procedure is somewhat problematic (and becomes more so when there are three inverse temperatures).

Instead, we will look at the expectation value of the non-invariant *mean square stream function* Ψ:

$$\Psi = \sum_{\mathbf{k}\in\mathcal{K}'} k^{-4} \, |\tilde{\omega}(\mathbf{k})|^2, \tag{5.6}$$

which is

$$\langle\Psi\rangle = \Psi = \sum_{\mathbf{k}\in\mathcal{K}'} \frac{1}{k^2 \, (\alpha + \beta k^2)}. \tag{5.7}$$

Although $\mathcal{E}$ and Ω will differ from the initial values of E and Ω only up to small fluctuations, we do not know what Ψ is, *á priori*. However, we can use Ψ to parameterize α and β by the following procedure.

First, we note that the following algebraic relations can be derived from (5.4), (5.5) and (5.7):

$$\alpha\mathcal{E} + \beta\Omega = \sum_{\mathbf{k}\in\mathcal{K}'} 1 \equiv \mathcal{N}'. \tag{5.8}$$

$$\alpha\Psi + \beta\mathcal{E} = \sum_{\mathbf{k}\in\mathcal{K}'} \frac{1}{k^2} \equiv \mathcal{L} \tag{5.9}$$

These 'thermodynamic relationships' are simultaneous linear equations and are readily solved to yield:

$$\alpha = \frac{\mathcal{L}\Omega - \mathcal{N}'\mathcal{E}}{\Omega\Psi - \mathcal{E}^2} \tag{5.10}$$

$$\beta = \frac{\mathcal{N}'\Psi - \mathcal{L}\mathcal{E}}{\Omega\Psi - \mathcal{E}^2}. \tag{5.11}$$

These have been written so that the denominators on the right sides are positive:

$$\Omega\Psi - \mathcal{E}^2 = \frac{1}{2} \sum_{\mathbf{q},\mathbf{k}\in\mathcal{K}'} \frac{(q^2 - k^2)^2}{(\alpha + \beta q^2)(\alpha + \beta k^2)} > 0. \tag{5.12}$$

The numerator in (5.10) is:

$$\mathcal{L}\Omega - \mathcal{N}'\mathcal{E} = \frac{\alpha}{2} \sum_{\mathbf{q},\mathbf{k}\in\mathcal{K}'} \frac{(q^2 - k^2)^2}{q^2 k^2 (\alpha + \beta q^2)(\alpha + \beta k^2)}. \tag{5.13}$$

The numerator in (5.11) is:

$$\mathcal{N}'\Psi - \mathcal{L}\mathcal{E} = \frac{\beta}{2} \sum_{\mathbf{q},\mathbf{k}\in\mathcal{K}'} \frac{(q^2 - k^2)^2}{q^2 k^2 (\alpha + \beta q^2)(\alpha + \beta k^2)}. \tag{5.14}$$

Placing (5.12), (5.13) and (5.14) into (5.10) and (5.11) yields a tautology.

At this point, we can allow Ψ to vary: $\Psi \to \Psi'$, which turns (5.10) and (5.11) into

$$\alpha' = \frac{\mathcal{L}\Omega - \mathcal{N}'\mathcal{E}}{\Omega\Psi' - \mathcal{E}^2} \tag{5.15}$$

$$\beta' = \frac{\mathcal{N}'\Psi' - \mathcal{L}\mathcal{E}}{\Omega\Psi' - \mathcal{E}^2}. \tag{5.16}$$

Here, $\mathcal{E}$ and Ω are constant values and Ψ' is a variable parameter, $\Psi' > \mathcal{E}^2/\Omega$, such that $\alpha' = \alpha$ and $\beta' = \beta$, when $\Psi' = \Psi$. The challenge is to find a procedure for determining when $\Psi' = \Psi$, so that α and β may be found, and the modal expectation values (4.40) exactly determined. This will be done in the next section, after we treat the other cases of ideal turbulence and develop results analogous to the above expressions.

5.1.2 3-D Euler

In this case, the two (invariant) functions are the energy E and the kinetic helicity H_K:

$$E = \sum_{\mathbf{k}\in\mathcal{K}'} |\tilde{\mathbf{u}}(\mathbf{k})|^2 \tag{5.17}$$

$$H_K = \sum_{\mathbf{k}\in\mathcal{K}'} \tilde{\mathbf{u}}(\mathbf{k}) \cdot \tilde{\boldsymbol{\omega}}(\mathbf{k}). \tag{5.18}$$

If we take the expectation values of these, and use the modal results given in (4.42) and (4.44), we get

$$\langle E \rangle = \mathcal{E} = \sum_{\mathbf{k}\in\mathcal{K}'} \frac{3\alpha}{\alpha^2 - \beta^2 k^2} \tag{5.19}$$

$$\langle H_K \rangle = \mathcal{H}_K = \sum_{\mathbf{k}\in\mathcal{K}'} \frac{-3\beta k^2}{\alpha^2 - \beta^2 k^2}. \tag{5.20}$$

We see that in the 3-D Euler case, the inverse temperatures α and β are implicit functions of $\mathcal{E}$ and $\mathcal{H}_K$.

Here, we will look at the expectation value of the enstrophy Ω, which is non-invariant for 3-D Euler turbulence. The enstrophy is

$$\Omega = \sum_{\mathbf{k}\in\mathcal{K}'} k^2 \, |\tilde{\mathbf{u}}(\mathbf{k})|^2, \tag{5.21}$$

and its expectation value, using (4.42), is

$$\langle \Omega \rangle = \Omega = \sum_{\mathbf{k}\in\mathcal{K}'} \frac{3k^2\,\alpha}{\alpha^2 - \beta^2 k^2}. \tag{5.22}$$

Both $\mathcal{E}$ and $\mathcal{H}_K$ will differ little from the initial values of E and H_K, but in this case we do not know the value of Ω, *á priori*. Here, we will use a variable Ω' to parameterize α and β, in a similar manner as before.

Using $\mathcal{N}'$ as defined in (5.8), the following algebraic relations can easily be derived from (5.19), (5.20), and (5.22):

$$\alpha\mathcal{E} + \beta\mathcal{H}_K = 3\mathcal{N}' \tag{5.23}$$

$$\alpha\mathcal{H}_K + \beta\Omega = 0. \tag{5.24}$$

These simple linear equations readily provide α and β:

$$\alpha = \frac{3\mathcal{N}'\Omega}{\mathcal{E}\Omega - \mathcal{H}_K^2} \tag{5.25}$$

$$\beta = -\frac{\mathcal{H}_K}{\Omega}\,\alpha. \tag{5.26}$$

Again, we have a thermodynamic relationship: the inverse temperatures for 3-D Euler turbulence are given explicitly in terms of the unknown value Ω. Thus, the equations

$$\alpha' = \frac{3\mathcal{N}'\Omega'}{\mathcal{E}\Omega' - \mathcal{H}_K^2} \tag{5.27}$$

$$\beta' = -\frac{\mathcal{H}_K}{\Omega'}\,\alpha' \tag{5.28}$$

produce the correct values α and β when the variable parameter Ω' is set equal to Ω, which in turn allows the modal expectations values (4.42) and (4.44) to be determined.

5.1.3 2-D MHD

Here, the (invariant) functions are the total energy E, the cross helicity H_C, and the mean square vector potential A (for $B_o = 0$):

$$E = \sum_{\mathbf{k}\in\mathcal{K}'} \left[k^{-2}\,|\tilde{\omega}(\mathbf{k})|^2 + k^2\,|\tilde{a}(\mathbf{k})|^2\right] \tag{5.29}$$

$$H_C = \sum_{\mathbf{k}\in\mathcal{K}'} \tilde{\omega}^*(\mathbf{k})\,\tilde{a}(\mathbf{k}) \tag{5.30}$$

$$A = \sum_{\mathbf{k}\in\mathcal{K}'} |\tilde{a}(\mathbf{k})|^2. \tag{5.31}$$

If we take the expectation values of these, and use the modal results given in (4.47), we arrive at

$$\langle E\rangle = \mathcal{E} = \sum_{\mathbf{k}\in\mathcal{K}'} \frac{2\alpha + \gamma/k^2}{\delta^2 + \alpha\gamma/k^2} \tag{5.32}$$

$$\langle H_C \rangle = \mathcal{H}_C = \sum_{\mathbf{k}\in\mathcal{K}'} \frac{-\beta/2}{\delta^2 + \alpha\gamma/k^2} \tag{5.33}$$

$$\langle A \rangle = \mathcal{A} = \sum_{\mathbf{k}\in\mathcal{K}'} \frac{\alpha/k^2}{\delta^2 + \alpha\gamma/k^2}. \tag{5.34}$$

Here, $\delta^2 = \alpha^2 - \frac{1}{4}\beta^2$. We see that in the 2-D MHD case, the inverse temperatures α, β, and γ are implicit functions of $\langle E \rangle$, $\langle H_C \rangle$ and $\langle A \rangle$.

In this case, we also consider the expectation value of the magnetic energy E_M, which is a non-invariant function for 2-D MHD turbulence:

$$E_M = \sum_{\mathbf{k}\in\mathcal{K}'} k^2 \, |\tilde{a}(\mathbf{k})|^2. \tag{5.35}$$

The expectation value of this, using (4.47), is

$$\langle E_M \rangle = \mathcal{E}_M = \sum_{\mathbf{k}\in\mathcal{K}'} \frac{\alpha}{\delta^2 + \alpha\gamma/k^2}. \tag{5.36}$$

Again, $\delta^2 = \alpha^2 - \frac{1}{4}\beta^2$. While $\mathcal{E}$, $\mathcal{H}_C$, and $\mathcal{A}$ are constants, the value of $\mathcal{E}_M$ will have relatively large fluctuations. Here, we will use $\mathcal{E}'_M$ to parameterize α, β, and γ.

Using $\mathcal{N}'$ as defined in (5.8), the following algebraic relations can easily be derived from the above expressions:

$$\alpha\mathcal{E} + \beta\mathcal{H}_C + \gamma\mathcal{A} = 2\mathcal{N}' \tag{5.37}$$

$$2\alpha\mathcal{H}_C + \beta\mathcal{E}_M = 0 \tag{5.38}$$

$$\alpha(\mathcal{E} - 2\mathcal{E}_M) - \gamma\mathcal{A} = 0. \tag{5.39}$$

These 'thermodynamic relations' readily provide α, β, and γ:

$$\alpha = \frac{\mathcal{N}'\mathcal{E}_M}{\mathcal{E}_M(\mathcal{E} - \mathcal{E}_M) - \mathcal{H}_C^2} \tag{5.40}$$

$$\beta = -2\frac{\mathcal{H}_C}{\mathcal{E}_M}\,\alpha \tag{5.41}$$

$$\gamma = \frac{\mathcal{E} - 2\mathcal{E}_M}{\mathcal{A}}\,\alpha. \tag{5.42}$$

The inverse temperatures for 2-D MHD turbulence are thus given explicitly in terms of the unknown value of $\mathcal{H}_M$. Here, we use a variable $\mathcal{E}'_M$ to parameterize the inverse temperatures:

$$\alpha' = \frac{\mathcal{N}'\mathcal{E}'_M}{\mathcal{E}'_M(\mathcal{E} - \mathcal{E}'_M) - \mathcal{H}_C^2} \tag{5.43}$$

$$\beta' = -2\frac{\mathcal{H}_C}{\mathcal{E}'_M}\,\alpha' \tag{5.44}$$

$$\gamma' = \frac{\mathcal{E} - 2\mathcal{E}'_M}{\mathcal{A}}\,\alpha'. \tag{5.45}$$

Again, the true value $\mathcal{E}'_M = \mathcal{E}_M$ is unknown, but once it is found, allows us to determine α, β, and γ and thus the exact values of the modal expectation values (4.47). (In the case where $B_o = 1$, we require $\gamma = \gamma' = 0$, which leads to $\mathcal{E}'_M = \frac{1}{2}\mathcal{E}$ as the correct value, without further ado.)

5.1.4 3-D MHD

Here, the (invariant) functions are the total energy E, the cross helicity H_C and the mean square vector potential H_M (for $B_o = 0$):

$$E = \sum_{\mathbf{k}\in\mathcal{K}'} \left[|\tilde{\mathbf{u}}(\mathbf{k})|^2 + |\tilde{\mathbf{b}}(\mathbf{k})|^2\right] \tag{5.46}$$

$$H_C = \sum_{\mathbf{k}\in\mathcal{K}'} \tilde{\mathbf{u}}^*(\mathbf{k}) \cdot \tilde{\mathbf{b}}(\mathbf{k}) \tag{5.47}$$

$$H_M = \sum_{\mathbf{k}\in\mathcal{K}'} \tilde{\mathbf{a}}^*(\mathbf{k}) \cdot \tilde{\mathbf{b}}(\mathbf{k}). \tag{5.48}$$

If we take the expectation values of these, and use the modal results given in (4.47), we arrive at

$$\langle E\rangle = \mathcal{E} = \sum_{\mathbf{k}\in\mathcal{K}'} \frac{3\alpha(2\delta^2 - \gamma^2/k^2)}{\delta^4 - \alpha^2\gamma^2/k^2} \tag{5.49}$$

$$\langle H_C\rangle = \mathcal{H}_C = \sum_{\mathbf{k}\in\mathcal{K}'} \frac{-3\beta\delta^2/2}{\delta^4 - \alpha^2\gamma^2/k^2} \tag{5.50}$$

$$\langle H_M\rangle = \mathcal{H}_M = \sum_{\mathbf{k}\in\mathcal{K}'} \frac{-3\alpha^2\gamma/k^2}{\delta^4 - \alpha^2\gamma^2/k^2}. \tag{5.51}$$

Here, $\delta^2 = \alpha^2 - \frac{1}{4}\beta^2$. We see that in the 3-D MHD case, the inverse temperatures α, β and γ are implicit functions of $\mathcal{E}$, $\mathcal{H}_C$, and $\mathcal{H}_M$.

As in the 2-D MHD case, we utilize the expectation value of the magnetic energy E_M, which is also a non-invariant function for 3-D MHD turbulence:

$$E_M = \sum_{\mathbf{k}\in\mathcal{K}'} k^2\,|\tilde{\mathbf{b}}(\mathbf{k})|^2. \tag{5.52}$$

The expectation value of this, using (4.47), is

$$\langle E_M\rangle = \mathcal{E}_M = \sum_{\mathbf{k}\in\mathcal{K}'} \frac{3\alpha\delta^2}{\delta^4 - \alpha^2\gamma^2/k^2}. \tag{5.53}$$

Again, $\delta^2 = \alpha^2 - \frac{1}{4}\beta^2$. While $\mathcal{E}$, $\mathcal{H}_C$, and $\mathcal{H}_M$ are constants, the value of $\mathcal{E}_M$ will have relatively large fluctuations. Here, as in the 2-D case, we use $\mathcal{E}'_M$ to parameterize α, β, and γ.

Using $\mathcal{N}'$ as defined in (5.8), the following algebraic relations follow from the above expressions:

$$\alpha\mathcal{E} + \beta\mathcal{H}_C + \gamma\mathcal{H}_M = 6\mathcal{N}' \tag{5.54}$$

$$2\alpha\mathcal{H}_C + \beta\mathcal{E}_M = 0 \tag{5.55}$$

$$\alpha(\mathcal{E} - 2\mathcal{E}_M) - \gamma\mathcal{H}_M = 0. \tag{5.56}$$

These 'thermodynamic relations' (which are the same as the 2-D MHD case if $\mathcal{N}'$ and $\mathcal{A}$ there are replaced by $3\mathcal{N}'$ and $\mathcal{H}_M$ here) immediately provide α, β, and γ:

$$\alpha = \frac{3\mathcal{N}'\mathcal{E}_M}{\mathcal{E}_M(\mathcal{E} - \mathcal{E}_M) - \mathcal{H}_C^2} \tag{5.57}$$

$$\beta = -2\frac{\mathcal{H}_C}{\mathcal{E}_M}\,\alpha \tag{5.58}$$

$$\gamma = \frac{\mathcal{E} - 2\mathcal{E}_M}{\mathcal{H}_M}\,\alpha. \tag{5.59}$$

The inverse temperatures for 3-D MHD turbulence are given explicitly in terms of the unknown value of $\mathcal{H}_M$. Using the variable $\mathcal{E}'_M$ to parameterize these gives:

$$\alpha' = \frac{3\mathcal{N}'\mathcal{E}'_M}{\mathcal{E}'_M(\mathcal{E} - \mathcal{E}'_M) - \mathcal{H}_C^2} \tag{5.60}$$

$$\beta' = -2\frac{\mathcal{H}_C}{\mathcal{E}'_M}\,\alpha' \tag{5.61}$$

$$\gamma' = \frac{\mathcal{E} - 2\mathcal{E}'_M}{\mathcal{H}_M}\,\alpha'. \tag{5.62}$$

Although the true value $\mathcal{E}'_M = \mathcal{E}_M$ is unknown, once it is found, allows us to determine α, β, and γ and thus the exact values of the modal expectation values (4.56). (In the case where $B_\mathrm{o} = 1$, we require $\gamma = \gamma' = 0$, which again leads to $\mathcal{E}'_M = \frac{1}{2}\,\mathcal{E}$ as the correct value.)

5.2 Entropy

Now that we have expressed the inverse temperatures for all cases of ideal homogeneous turbulence in terms of a variable parameter, we can move on to defining a procedure for actually determining the expectation value of the parameter. We do this by first defining the *entropy* for each of the cases of ideal turbulence, and by showing that the entropy we define in each case satisfies the second law of thermodynamics. The probability density for all cases has the form

$$D = Z^{-1}\,\exp\left(-\alpha I_1 - \beta I_2 - \gamma I_3\right) \tag{5.63}$$

$$Z = \prod_{\mathbf{k}\in\mathcal{K}'} Z(\mathbf{k}), \tag{5.64}$$

where the I_j, $j = 1, 2, 3$, are given in Table 4.1 and the $Z(\mathbf{k})$ are given in Table 4.2. The entropy is defined as

$$\begin{aligned} S &= -\langle \ln D \rangle \\ &= \alpha \langle I_1 \rangle + \beta \langle I_2 \rangle + \gamma \langle I_3 \rangle + \ln Z \\ &= c\mathcal{N}' + \sum_{\mathbf{k} \in \mathcal{K}'} \ln Z(\mathbf{k}). \end{aligned} \tag{5.65}$$

Here, $c = \frac{1}{2} m$ is the 'specific heat' of a mode, where m is defined by (5.1) as the number of degrees of freedom per mode. The term $c\mathcal{N}'$ in (5.65) arises when the expressions (5.8), (5.23), (5.37) and (5.54) are used for the different cases of ideal turbulence. Thus, $c = 1, 2, 3, 6$ for the 2-D Euler, 2-D MHD, 3-D Euler, and 3-D MHD cases, respectively.

The $Z(\mathbf{k})$ are functions of the inverse temperatures α, β, γ, and k as Table 4.2 shows. Since α, β, and γ are implicit functions of the invariants, the entropy S, as defined in (5.65), is also an implicit function of the invariants and thus is also a constant for a closed system; *i.e.*, it does not change unless the system is allowed to interact with another previously isolated system. As (5.65) shows, entropy is also a function of the number of independent modes $\mathcal{N}'$ in the set of modes $\mathcal{K}$ under consideration. (The subset of independent $\mathbf{k}$ is $\mathcal{K}'$.) The entropy has the following functionality:

$$S = \sigma(\mathcal{K}, \alpha, \beta, \gamma). \tag{5.66}$$

Using (5.65) as well as Table 4.2 allows us to list the entropy functionals $\sigma(\mathcal{K}, \alpha, \beta, \gamma)$ in Table 5.1.

Now, if we use the variable parameters Ψ', Ω', or $\mathcal{E}'_M$ to define variable inverse temperatures α', β', and γ', as we do in the previous section, then we can allow the entropy to vary from its expectation value of S to S', where

$$S' = \sigma(\mathcal{K}, \alpha', \beta', \gamma'). \tag{5.67}$$

We will now show that $\sigma(\mathcal{K}, \alpha', \beta', \gamma')$ takes a minimum value when $\alpha' = \alpha$, $\beta' = \beta$, and $\gamma' = \gamma$. This will then provide us with a procedure for finding α, β, and γ without having to solve multivariable implicit equations, and more importantly, it will enable a demonstration that entropy never decreases when two previously isolated systems are brought together into one interacting system.

5.2.1 A Global Minimum

As a specific example of the global behaviour of entropy with respect to the variable parameters that have been defined, we will examine the 2-D Euler case. Using Table 5.1, equation (5.67) becomes

$$\begin{aligned} S' &= \mathcal{N}'(1 + \ln \pi) - \sum_{\mathbf{k} \in \mathcal{K}'} \ln(\alpha'/k^2 + \beta') \\ &= \mathcal{N}'(1 + \ln \pi) + \sum_{\mathbf{k} \in \mathcal{K}'} \ln k^2 - \sum_{\mathbf{k} \in \mathcal{K}'} \ln(\alpha' + \beta' k^2). \end{aligned} \tag{5.68}$$

$\sigma(\mathcal{K},\alpha,\beta,\gamma) = c\,[\mathcal{N}'(1+\ln\pi) - \sum_{\mathcal{K}'}\ln\phi(k,\alpha,\beta,\gamma)]$		
Case	c	$\phi(k,\alpha,\beta,\gamma)$
2-D Euler	1	$\alpha/k^2+\beta$
3-D Euler	3	$(\alpha^2-\beta^2k^2)^{\frac{1}{2}}$
2-D MHD†	2	$(\delta^2+\alpha\gamma/k^2)^{\frac{1}{2}}$
3-D MHD†	6	$(\delta^4-\alpha^2\gamma^2/k^2)^{\frac{1}{4}}$

†Here, $\delta^2=\alpha^2-\frac{1}{4}\beta^2$; also, when $B_\mathrm{o}=1$, $\gamma\equiv 0$.

Table 5.1: Entropy functionals for ideal turbulence.

Using $\alpha'(\Psi')$, as given by (5.15), and $\beta'(\Psi')$, as given by (5.16), we have

$$\begin{aligned}\frac{d\alpha'}{d\Psi'} &= -\frac{\Omega\alpha'}{\Omega\Psi'-\mathcal{E}^2}\\ \frac{d\beta'}{d\Psi'} &= \frac{\mathcal{N}'-\Omega\beta'}{\Omega\Psi'-\mathcal{E}^2}.\end{aligned}\tag{5.69}$$

Using these results, the derivative of S' by Ψ' is

$$\begin{aligned}\frac{dS'}{d\Psi'} &= \frac{\partial S'}{\partial\alpha'}\frac{d\alpha'}{d\Psi'}+\frac{\partial S'}{\partial\beta'}\frac{d\beta'}{d\Psi'}\\ &= \sum_{\mathbf{k}\in\mathcal{K}'}\frac{1}{\alpha'+\beta'k^2}\,\frac{\alpha'\Omega+(\beta'\Omega-\mathcal{N}')k^2}{\Omega\Psi'-\mathcal{E}^2}\\ &= -\frac{\mathcal{N}'(\Omega'-\Omega)}{\Omega\Psi'-\mathcal{E}^2}.\end{aligned}\tag{5.70}$$

(Recall that $\Psi'>\mathcal{E}^2/\Omega$.) Here we have defined Ω' as

$$\Omega' = \sum_{\mathbf{k}\in\mathcal{K}'}\frac{k^2}{\alpha'+\beta'k^2}.\tag{5.71}$$

The result (5.70) indicates that $dS'/d\Psi' = 0$ when $\Omega' - \Omega = 0$, or

$$\begin{aligned} \Omega' - \Omega &= \sum_{\mathbf{k}\in\mathcal{K}'} \left[\frac{k^2}{\alpha' + \beta' k^2} - \frac{k^2}{\alpha + \beta k^2} \right] \\ & \sum_{\mathbf{k}\in\mathcal{K}'} \frac{(\alpha' - \alpha)k^2 + (\beta' - \beta)k^4}{(\alpha' + \beta' k^2)(\alpha + \beta k^2)}. \end{aligned} \tag{5.72}$$

Now, we can use (5.10), (5.11), (5.15), and (5.16), along with some algebraic manipulation, to show

$$\alpha' - \alpha = -(\beta' - \beta)\bar{k}^2, \quad \bar{k}^2 = \frac{\Omega}{\mathcal{E}}. \tag{5.73}$$

Placing this into (5.72) gives

$$\begin{aligned} \Omega' - \Omega &= (\beta' - \beta)F' \\ F' &= \sum_{\mathbf{k}\in\mathcal{K}'} \frac{k^2(k^2 - \bar{k}^2)}{(\alpha' + \beta' k^2)(\alpha + \beta k^2)}. \end{aligned} \tag{5.74}$$

We know from (5.70) that S' has an extremum at $\Omega' = \Omega$, and we now prove two assertions: 1) that this only occurs at $\Psi' = \Psi$, and 2) that the extremum is actually a minimum.

To prove the first assertion, we must show that $F' \neq 0$ when $\Omega' = \Omega$ (initially leaving open the possibility that $\Psi' \neq \Psi$). Using (5.10), (5.11), (5.15), and (5.16) again, along with some more algebraic manipulation, shows that

$$F = F'|_{\Omega'=\Omega} = \frac{\alpha' \mathcal{E}}{\mathcal{N}'^2} \sum_{\mathbf{k}\in\mathcal{K}'} \frac{(k^2 - \bar{k}^2)^2}{(\alpha' + \beta' k^2)(\alpha + \beta k^2)}. \tag{5.75}$$

Here we obviously have $F > 0$, so that $F \neq 0$. Using (5.11) and (5.16) gives

$$\beta' - \beta = -\frac{\mathcal{E}\alpha(\Psi' - \Psi)}{\Omega\Psi' - \mathcal{E}^2}. \tag{5.76}$$

Placing (5.76) into (5.74), as $\Omega' \to \Omega$, we also have $\Psi' \to \Psi$, so that

$$\lim_{\Omega'\to\Omega} \Omega' = \Omega - (\Psi' - \Psi)G, \tag{5.77}$$

where G, using (5.75), is defined by

$$G = \frac{\mathcal{E}^2 \alpha}{\mathcal{N}'^2(\Omega\Psi - \mathcal{E}^2)} \sum_{\mathbf{k}\in\mathcal{K}'} \frac{(k^2 - \bar{k}^2)^2}{(\alpha + \beta k^2)^2} > 0. \tag{5.78}$$

Using (5.70) and (5.77), we see that

$$\lim_{\Omega'\to\Omega} \frac{dS'}{d\Psi'} = \frac{\mathcal{N}' G}{\Omega\Psi - \mathcal{E}^2}(\Psi' - \Psi). \tag{5.79}$$

Thus, we have proven our first assertion, that an extremum occurs only at $\Psi' = \Psi$.

Next, using (5.79), we immediately see that

$$\left.\frac{d^2 S'}{d\Psi'^2}\right|_{\Psi'=\Psi} = \frac{\mathcal{N}'G}{\Omega\Psi' - \mathcal{E}^2} > 0. \tag{5.80}$$

This proves our second assertion: that $\Psi' = \Psi$ is a minimum of S', and by the results given above, it is a *global minimum*.

Although it will not be shown here, we assume that analogous results for the other cases of ideal homogeneous turbulence can be found, requiring only increasingly laborious algebraic manipulations. (These manipulations have been carried through for the 3-D Euler case, although not for the ideal MHD cases with $B_o = 0$. It is conjectured, and fully expected, that the MHD cases will follow suit.) The results, in each case, should mirror what has been shown above, that when the entropies as defined in Table 5.1, and the inverse temperatures are given a variable parameter, as described earlier in this chapter, then the entropies have a global minimum with respect to this parameter. Now, we will move from these facts and plausible conjectures to establish a 'second law of thermodynamics' for ideal homogeneous turbulence.

5.3 The Second Law

First, a heuristic look at the expansion of a restricted set of modes into a larger set will be given, and second, a general proof that entropy never decreases when two previously isolated subsystems are brought together - *The Second Law of Thermodynamics*.

5.3.1 Expansion Into a Larger Set of Modes

To begin, we define two noninteracting systems that can then be allowed to interact. We use the two disjoint sets of modes $\mathcal{K}^{(i)}$, $i = 1, 2$, defined in (4.13). Recall that both these sets consist of vectors $\mathbf{k}$, $0 \leq k \leq k_{max}$, with the difference between them being that $\mathcal{K}^{(1)}$ has only those $\mathbf{k}$ with k^2 odd, while $\mathcal{K}^{(2)}$ has only those $\mathbf{k}$ with k^2 even.

Now, k^2 is the sum of two squared integers ('squares') for 2-D flows, while it is the sum of three squares for 3-D flows. The following results from number theory are applicable here:

Sums of two squares: k^2 is the sum of two squares if and only if its (unique) prime factorization contains no odd powers of primes p, such that $p = 4m + 3$, where m is a nonnegative integer.

Sums of three squares: k^2 is the sum of three squares only if it is not of the form $4^n(8m + 7)$, where n and m are nonnegative integers.

Thus, k^2 cannot take all possible positive integer values, in either 2-D or 3-D. (There is

a well-known theorem, however, that states that sums of four squares can take all nonnegative integer values.)

The number of positive integer values that $k^2 \leq k_{max}^2$ can take out of the total number available (*i.e.*, k_{max}^2) is different for 2-D and 3-D. A simple computer program shows that, in the 2-D case, most positive integers $\leq k_{max}^2$ are not the sum of two squares (for $k_{max}^2 = 10^4$, k^2 takes 2,749 out of 10^4 possible values – about 27.5%; for $k_{max}^2 = 10^6$, k^2 takes 216,314 out of 10^6 possible values – about 21.6%). In the 3-D case, the ratio of integers that are the sum of three squares for a given k_{max}^2 to those that are not is almost exactly 5 to 1 (about 83%), as k_{max}^2 increases. However, in both the 2-D and 3-D cases, the number of individual vectors $\mathbf{k}$ in the sets $\mathcal{K}^{(i)}$, $i = 1, 2$, appears to be essentially equal, for $k_{max} > 10$.

The two sets $\mathcal{K}^{(1)}$ and $\mathcal{K}^{(2)}$ have an interesting structure: $\mathcal{K}^{(1)}$ identifies a completely noninteracting set of wave vectors, while $\mathcal{K}^{(2)}$ comprises a set of completely interacting wave vectors. To see this more clearly, we will now examine the parity (even-oddness) of the components of the vectors in $\mathcal{K}^{(1)}$ and $\mathcal{K}^{(2)}$. Let us represent even integers by 'e' and odd integers by 'o.' Adding or multiplying even and even, even and odd, or odd and odd integers yields even or odd integers in the following pattern:

$$\begin{array}{lll} e + e \sim e & o + o \sim e & e + o = o + e \sim o \\ e \cdot e \sim e & o \cdot o \sim o & e \cdot o = o \cdot e \sim e \end{array} \quad . \tag{5.81}$$

Now, remember that for $\mathbf{k} \in \mathcal{K}^{(1)}$, we have $k^2 \sim o$, while for $\mathbf{k} \in \mathcal{K}^{(2)}$, we have $k^2 \sim e$. Using the equivalences in (5.81), it is easy to see that, in 2-D, the kinds of vectors found in the two subsets $\mathcal{K}^{(1)}$ and $\mathcal{K}^{(2)}$ are

$\mathcal{K}^{(1)}$	$\mathcal{K}^{(2)}$
(e, o)	(e, e) .
(o, e)	(o, o)

(5.82)

Again using (5.81), in 3-D, the kinds of vectors found in $\mathcal{K}^{(1)}$ and $\mathcal{K}^{(2)}$ are

$\mathcal{K}^{(1)}$	$\mathcal{K}^{(2)}$
(o, o, o)	(e, e, e)
(o, e, e)	(e, o, o) .
(e, o, e)	(o, e, o)
(e, e, o)	(o, o, e)

(5.83)

Since a component can have one of two values (e or o), the total number of types of vector is $N = 2^n$, where n is the dimension of the vector space. Thus, for 2-D, $N = 4$, and all

possible types are accounted for in (5.82). Similarly, for 3-D, $N = 8$, and all possible types are accounted for in (5.83).

We can use these results to deduce the following: When two vectors $\mathbf{p}, \mathbf{q} \in \mathcal{K}^{(1)}$ are added, then $\mathbf{p} + \mathbf{q} = \mathbf{k} \notin \mathcal{K}^{(1)}$, because $\mathbf{p} + \mathbf{q} \sim e$; thus no $\mathbf{p}, \mathbf{q} \in \mathcal{K}^{(1)}$ can be added to produce another wave vector in $\mathcal{K}^{(1)}$. On the other hand, for $\mathbf{p}, \mathbf{q} \in \mathcal{K}^{(2)}$, then $\mathbf{p}+\mathbf{q} = \mathbf{k} \sim e$; if $k \leq k_{max}$, then $\mathbf{k} \in \mathcal{K}^{(2)}$. Thus, two $\mathbf{p}, \mathbf{q} \in \mathcal{K}^{(1)}$ can be added together to produce another $\mathbf{k} \in \mathcal{K}^{(2)}$. In (3.59) and (3.60) it was shown that any nonzero $\mathbf{k} \in \mathcal{K}$ could be written as the sum of two nonzero wave vectors $\mathbf{p}, \mathbf{q} \in \mathcal{K}$; looking at the details there, we see that we can also state that any nonzero $\mathbf{k} \in \mathcal{K}^{(2)}$ could be written as the sum of two nonzero wave vectors $\mathbf{p}, \mathbf{q} \in \mathcal{K}^{(2)}$, for $k_{max}^2 \geq 2$. Thus, none of the $\mathbf{k} \in \mathcal{K}^{(1)}$ are dynamically coupled, while all of the $\mathbf{k} \in \mathcal{K}^{(2)}$ are coupled.

The relevance of all this for the simulation of homogenous turbulence is that we can separate the system of Fourier modes identified by $\mathbf{k} \in \mathcal{K}$ into two mutually noninteracting sets $\mathcal{K}^{(1)}$ and $\mathcal{K}^{(2)}$, but when we do so, only the set $\mathcal{K}^{(2)}$ contains dynamically interacting modes, while the set $\mathcal{K}^{(1)}$ contains no dynamically interacting modes at all (the modes associated with $\mathcal{K}^{(1)}$ are *frozen*). By restricting the dynamically interacting modes in a finite model of homogeneous turbulence initially to $\mathbf{k} \in \mathcal{K}^{(2)}$, we can then allow the restricted system to 'expand' into a larger system by turning on the interaction between modes in $\mathcal{K}^{(1)}$ and $\mathcal{K}^{(2)}$, so that the final set of interacting modes is $\mathbf{k} \in \mathcal{K}^{(1)} \cup \mathcal{K}^{(2)} = \mathcal{K}$.

We can assign an entropy to each of the isolated systems $\mathcal{K}^{(1)}$ and $\mathcal{K}^{(2)}$, which have $\mathcal{N}^{(1)}$ and $\mathcal{N}^{(2)}$ modes, respectively, with $\mathcal{N}^{(1)} \cong \mathcal{N}^{(2)}$. The system $\mathcal{K}^{(1)}$ is actually a system of $\mathcal{N}^{(1)}$ noninteracting subsystems, each containing only one mode. Since these modes do not evolve, the number of states available to each isolated mode is $n(\mathbf{k}) = 1$; the number of states available to $\mathcal{K}^{(1)}$ is no more than the product $\prod_{\mathbf{k} \in \mathcal{K}^{(1)}} n(\mathbf{k}) = 1$. The entropy of each mode is $\ln n(\mathbf{k})$, so that the entropy $S^{(1)}$ of the whole system of modes $\mathcal{K}^{(1)}$ is zero (this is *Nernst's theorem*). However, the value of the energy (and other invariant values) locked in these frozen modes is not necessarily zero.

The entropy of $\mathcal{K}^{(2)}$ can be found using Table 5.1. Recall that the entropy is the global minimum of the entropy functional in Table 5.1 and that the summations there are now over all $\mathcal{N}^{(2)}$ interacting wave vectors $\mathbf{k} \in \mathcal{K}^{(2)}$. The entropy is

$$\begin{aligned} S^{(2)} &= \min\{\sigma(\mathcal{K}^{(2)}, \alpha, \beta, \gamma)\} \\ &= \sigma(\mathcal{K}^{(2)}, \alpha^{(2)}, \beta^{(2)}, \gamma^{(2)}), \end{aligned} \tag{5.84}$$

where

$$\begin{aligned} &\sigma(\mathcal{K}, \alpha, \beta, \gamma) = \\ &\frac{1}{2} c \left[\mathcal{N}(1 + \ln \pi) - \sum_{\mathbf{k} \in \mathcal{K}} \ln \phi(k, \alpha, \beta, \gamma) \right]. \end{aligned} \tag{5.85}$$

(Here, we have used $\mathcal{N} = 2\mathcal{N}'$.) If we add the two systems together to form $\mathcal{K} = \mathcal{K}^{(1)} \cup \mathcal{K}^{(2)}$, then the total number of $\mathbf{k} \in \mathcal{K}$ is $\mathcal{N} = \mathcal{N}^{(1)} + \mathcal{N}^{(2)}$.

Assume that the energy (and other invariant values) locked in the frozen modes $\mathcal{K}^{(1)}$ is proportional to those associated with the interacting modes $\mathcal{K}^{(2)}$; let the proportionality factor be r (*e.g.*, $E^{(1)} = rE^{(2)}$). The 'temperatures' $(\alpha^{(2)})^{-1}$, $(\beta^{(2)})^{-1}$, and $(\gamma^{(2)})^{-1}$ are given in the first section of this chapter; the pertinent expressions indicate that when expansion from $\mathcal{K}^{(2)}$ to $\mathcal{K}$ occurs, the temperatures will drop by approximately $(1 + r)/2$. Therefore, we see from Table 5.1 that

$$\phi(k, \alpha, \beta, \gamma) \cong \frac{2}{1+r}\phi(k, \alpha^{(2)}\beta^{(2)}, \gamma^{(2)}). \tag{5.86}$$

Expansion of $\mathcal{K}^{(2)}$ into $\mathcal{K}$ will thus lead to the following change in entropy:

$$S = 2S^{(2)} - \mathcal{N}^{(2)} \ln[2/(1+r)], \quad r \geq 0. \tag{5.87}$$

Clearly, if $r \geq 1$, then entropy has increased. However, for $0 \leq r < 1$, it is unclear whether or not entropy might decrease. That it never decreases can be shown in a more general argument.

5.3.2 Proof of the Second Law

Here, we extend the proof of [Khinchin 49] to the case of systems with more than one temperature. The value of the entropy for a given isolated subsystem $\mathcal{K}_j$ of modes is determined by finding the global minimum of the entropy functionals given in Table 5.1:

$$S_j = \sigma(\mathcal{K}_j, \alpha_j, \beta_j, \gamma_j). \tag{5.88}$$

Here, α_j, β_j, and γ_j are the inverse temperatures that minimize σ in (5.88), for any subsystem j. Let us now unite the subsystems $j = a$ and $j = b$ to form the larger subsystem of interacting modes $\mathcal{K}_{ab} = \mathcal{K}_a \cup \mathcal{K}_b$.

The previously isolated subsystems $\mathcal{K}_a$ and $\mathcal{K}_b$ had entropies S_a and S_b:

$$\begin{aligned} S_a &= \sigma(\mathcal{K}_a, \alpha_a, \beta_a, \gamma_a) \\ S_b &= \sigma(\mathcal{K}_b, \alpha_b, \beta_b, \gamma_b). \end{aligned} \tag{5.89}$$

This new subsystem $\mathcal{K}_{ab}$ will have its own inverse temperatures α_{ab}, β_{ab}, and γ_{ab}, and entropy S_{ab}:

$$\begin{aligned} S_{ab} &= \sigma(\mathcal{K}_{ab}, \alpha_{ab}, \beta_{ab}, \gamma_{ab}) \\ &= \sigma(\mathcal{K}_a, \alpha_{ab}, \beta_{ab}, \gamma_{ab}) + \sigma(\mathcal{K}_b, \alpha_{ab}, \beta_{ab}, \gamma_{ab}) \\ &\geq \sigma(\mathcal{K}_a, \alpha_a, \beta_a, \gamma_a) + \sigma(\mathcal{K}_b, \alpha_b, \beta_b, \gamma_b). \end{aligned} \tag{5.90}$$

The second line above occurs because σ is a sum over independent $\mathbf{k}$ and can be partitioned as desired, while the third line occurs because $\alpha_a, \beta_a, \gamma_a$ and $\alpha_b, \beta_b, \gamma_b$ minimize the entropy functionals related to $\mathcal{K}_a$ and $\mathcal{K}_b$, respectively:

$$\begin{aligned} \sigma(\mathcal{K}_a, \alpha_a, \beta_a, \gamma_a) &\leq \sigma(\mathcal{K}_a, \alpha_{ab}, \beta_{ab}, \gamma_{ab}) \\ \sigma(\mathcal{K}_b, \alpha_b, \beta_b, \gamma_b) &\leq \sigma(\mathcal{K}_b, \alpha_{ab}, \beta_{ab}, \gamma_{ab}). \end{aligned} \tag{5.91}$$

In looking at (5.89), it is evident that (5.90) becomes

$$S_{ab} \geq S_a + S_b. \tag{5.92}$$

This is a general result and applies to all the cases of ideal homogeneous fluid and magnetofluid turbulence considered in the present work.

Finally, one point that is often missed needs to be emphasized. The entropy of a closed or quasi-closed (*i.e.*, canonical) system has a fixed value, essentially $S = \ln \Gamma$, where Γ is the number of 'states' available to the system in question. The entropy of such a system does not 'increase to the largest possible value if the system is left alone,' because once the system is 'left alone,' its entropy is fixed: the entropy is a function only of the number of accessible states, not a function of the instantaneous location of the system point in phase space. Only when two previously isolated systems, each with associated entropies (*i.e.*, measures of the number of available states of each isolated system), are united into a greater system, can total entropy actually increase, as shown in (5.92) above.

5.4 References for Further Reading

Two of the best references on statistical mechanics and thermodynamics are [Khinchin 49] and [Landau 80].

An early development of the concept of entropy in computer models of ideal turbulence, similar to that presented here, was given in [Shebalin 82], and a more recent discussion is given in [Shebalin 96] (where it is shown that the entropy function of [Carnevale 81, Carnevale 82] is not generally commensurate with absolute equilibrium ensemble theory).

Chapter 6

Numerical Experiments

The basis of a statistical theory of ideal homogeneous turbulence has been given in the preceding chapters. How well this theory works requires a comparison with results drawn from numerical experiments. We must use numerical experiments, rather than physical experiments, because ideal homogeneous turbulence is not physically realizable – no physical fluid or magnetofluid experiment has zero dissipation throughout its experimental sample. However, ideal turbulence is a model system whose equations differ from real ones only in the absence of a linear dissipative term (there is still a linear term in ideal MHD when a nonzero mean magnetic field is present). Although this linear dissipative term is critical, the remaining nonlinear terms are identical for real and ideal sets of equations. This motivates our desire for a comparison: A robust statistical theory of ideal turbulence may shed some light on how to obtain a corresponding theory for real turbulence, which has thus far been elusive.

Here we will present numerical results concerning all of the various cases of ideal homogeneous turbulence: Euler and ideal MHD turbulence, for both 2-D and 3-D. These numerical simulations were done on various supercomputers, and the total central processing unit (cpu) time used to generate the results to be described here was about 560 hours. This is a substantial investment and calls for a clear presentation of the methods of research, the results obtained, and the conclusions deduced; this is a prime motivator for this publication. Numerical results will be presented in this chapter, and an explanation of the somewhat surprising results will be given in the next chapter.

6.1 Numerical Method

The equations of motion to be solved are (3.44) and (3.45) for 2-D, and (3.15) and (3.16) for 3-D. The general technique used to numerically solve these equations is called a 'Fourier spectral transform method.' ('Spectral' refers to the coefficients, or 'spectrum,' of a Fourier expansion.)

The modal equations of motion have the form

$$\frac{d\,\tilde{U}(\mathbf{k},t)}{dt} \;=\; \tilde{F}(\tilde{U}(t);\mathbf{k}). \tag{6.1}$$

The term $\tilde{F}(\tilde{U};\mathbf{k})$ on the right side is nonlinear (except for a linear part that occurs in the MHD cases for $B_o \neq 0$). In what follows, when $\tilde{U}$ or $\tilde{U}(t)$ is used without a wave vector $\mathbf{k}$ in the argument, it signifies the set of coefficients $\tilde{U}(\mathbf{k},t)$.

As an example, for the 2-D Euler case, we have $\tilde{U}(\mathbf{k},t) = \tilde{\omega}(\mathbf{k},t)$ and

$$\tilde{F}(\tilde{\omega}(t);\mathbf{k}) \;=\; i \sum_{\mathbf{k},\,\mathbf{p},\,\mathbf{q}\,\in\mathcal{S}}^{\mathbf{p}+\mathbf{q}=\mathbf{k}} \hat{\mathbf{z}}\cdot\mathbf{p}\times\mathbf{q}\left[\tilde{\psi}(\mathbf{p},t)\,\tilde{\omega}(\mathbf{q},t)\right]. \tag{6.2}$$

Evaluating terms such as this in k-space takes an inordinate amount of time – there are $O(N^2)$ coefficients $\tilde{\omega}(\mathbf{k})$ and each summation has $O(N^4)$ terms, so that the total floating point operation count is $O(N^6)$. Instead, the quantities $i\mathbf{p}\tilde{\psi}(\mathbf{p})$ and $i\mathbf{q}\tilde{\omega}(\mathbf{q})$ are first transformed by a fast Fourier transform (FFT) into the x-space quantities $\nabla\psi(\mathbf{x})$ and $\nabla\omega(\mathbf{x})$, then the product $\mathbf{v}(\mathbf{x}) = \nabla\psi(\mathbf{x})\times\nabla\omega(\mathbf{x})$ is formed. Then we transform back by FFT to k-space: $\mathbf{v}(\mathbf{x}) \rightarrow \tilde{\mathbf{v}}(\mathbf{k})$ and form the result $\tilde{F}(\tilde{U};\mathbf{k}) = i\mathbf{k}\cdot\tilde{\mathbf{v}}(\mathbf{k})$.

In 2-D, the FFTs take $O[(N\ln N)^2]$ operations and the x-space nonlinear product takes $O(N^2)$ operations, so that the whole transform method takes $O[(N^2\ln N)^2]$ operations (where N is the number of grid points in each dimension). The comparative efficiency between working solely in k-space and using a transform technique is thus $O(N^6)$ versus $O[(N^2\ln N)^2]$: using FFTs reduces the number of floating point operations by $O[(N^{-1}\ln N)^2]$. (The reduction is $O[(N^{-1}\ln N)^3]$ in the 3-D cases.) Thus, while a direct evaluation of the (convolution) sum (6.2) may be impractical for a numerical simulation, the transform method is not, and in fact makes such simulations possible [Orszag 72].

The nonlinearity of (6.2) can introduce aliasing errors if care is not taken. Here, de-aliased nonlinear terms were produced using the Patterson-Orszag shifted-grid method [Patterson 71], which entails doing twice as many FFTs and setting $k_{max} = \sqrt{2}N/3$ (this value of k_{max} removes all but the single-aliasing errors). Specifically, for the 2-D Euler example,

$$\begin{aligned}
\tilde{\mathbf{v}}(\mathbf{p},\mathbf{a}) &= i\mathbf{p}\tilde{\psi}(\mathbf{p},t)e^{\mathbf{a}\cdot\mathbf{p}} \\
\tilde{\mathbf{w}}(\mathbf{q},\mathbf{a}) &= i\mathbf{q}\tilde{\omega}(\mathbf{q},t)e^{\mathbf{a}\cdot\mathbf{q}} \\
\tilde{\mathbf{v}}(\mathbf{p},\mathbf{a}) &- FFT \rightarrow \mathbf{v}(\mathbf{x},\mathbf{a}) \\
\tilde{\mathbf{w}}(\mathbf{p},\mathbf{a}) &- FFT \rightarrow \mathbf{w}(\mathbf{x},\mathbf{a}) \\
\tilde{\mathbf{G}}(\tilde{U};\mathbf{k},\mathbf{a}) &\leftarrow FFT - \mathbf{v}(\mathbf{x},\mathbf{a})\times\mathbf{w}(\mathbf{x},\mathbf{a}).
\end{aligned} \tag{6.3}$$

The transform cycle in (6.3) is done twice, with $\mathbf{a} = \mathbf{0}$ and $\mathbf{a} = \mathbf{h} = (\pi/N)(1,1,1)$. The de-aliased nonlinear product is then found by:

$$\begin{aligned}
\tilde{F}(\tilde{U};\mathbf{k}) &= -\frac{i}{2}\hat{\mathbf{z}}\cdot\left[\tilde{\mathbf{G}}(\tilde{U};\mathbf{k},\mathbf{0}) + e^{-i\mathbf{h}\cdot\mathbf{k}}\,\tilde{\mathbf{G}}(\tilde{U};\mathbf{k},\mathbf{h})\right] W(\mathbf{k}) \\
W(\mathbf{k}) &= \begin{array}{l} 1,\ k \le k_{max} \\ 0,\ k > k_{max} \end{array}.
\end{aligned} \tag{6.4}$$

which removes the remaining single-aliasing errors. (The function $W(\mathbf{k})$ ensures that the values of all coefficients with $k > k_{max}$ remain zero during the simulation.)

There is another method, called the '2/3' method, that requires only a single transform cycle by setting $k_{max} = N/3$. However, the number of de-aliased modes retained for a given N in the Patterson-Orszag method is twice as many as in the '2/3' method for 2-D and $2\sqrt{2} \cong 2.83$ as much for 3-D simulations. Although the Patterson-Orzsag method requires that two FFT tramsform cycles be done, which doubles the time needed to determine the nonlinear terms (6.2), it makes up for this by allowing at least twice as many modes to be retained in the simulation for a given value of N.

In general, the greatest portion of time in the numerical integration from one time-step to another goes into the evaluation of the nonlinear terms such as (6.2). In this regard, a time-stepping method was chosen so that the number of evaluations of (6.2) was minimized per time-step. For ease of coding and to minimize required core memory, lower-order time-integration schemes were also used.

The two time-integration methods used to solve the modal equations (6.1) were a second-order Runge-Kutta method (RK2) [Potter 73] and a third-order 'partially corrected' Adams-Bashforth method [Gadzag 76]. Time-step size Δt was fixed, so that after n time-steps, $t = t_n = n\Delta t$; also, $t_{n+1} = t_n + \Delta t$ and $t_{n+1/2} = t_n + \Delta t/2$. In addition, let us use the notation $\tilde{u}_n = \tilde{U}(\mathbf{k}, t_n)$, $\tilde{f}_n = \tilde{F}(\tilde{U}(t_n); \mathbf{k})$, $u_{n+1/2} = U(\mathbf{k}, t_{n+1/2})$, and $\tilde{f}_{n+1/2} = \tilde{F}(\tilde{U}(t_{n+1/2}); \mathbf{k})$. The RK2 method is

$$\begin{aligned} \tilde{u}_{n+1/2} &= \tilde{u}_n + \frac{\Delta t}{2}\tilde{f}_n \\ \tilde{u}_{n+1} &= \tilde{u}_n + \Delta t \tilde{f}_{n+1/2}. \end{aligned} \tag{6.5}$$

The RK2 method was used in the 2-D simulations and in a minority of 3-D simulations to be described shortly. The RK2 method is 'self starting,' *i.e.*, the necessary nonlinear terms $\tilde{f}_n$ and $\tilde{f}_{n+1/2}$ are computed at each time-step.

The AB3 method used has two parts: The first is an Adams-Bashforth predictor:

$$\bar{u}_{n+1} = \tilde{u}_n + \frac{\Delta t}{12}\left[23\tilde{f}_n - 16\tilde{f}_{n-1} + 5\tilde{f}_{n-2}\right]. \tag{6.6}$$

The second part is an Adams-Moulton corrector:

$$\begin{aligned} \tilde{f}_{n+1} &= \tilde{F}(\bar{u}_{n+1}; \mathbf{k}) \\ \tilde{u}_{n+1} &= \tilde{u}_n + \frac{\Delta t}{12}\left[5\tilde{f}_{n+1} + 8\tilde{f}_n - \tilde{f}_{n-1}\right]. \end{aligned} \tag{6.7}$$

Here, the $\tilde{f}_{n+1}$ are determined from the predicted coefficients $\bar{u}_{n+1}$, found in (6.6), in exactly the same way that the nonlinear terms $\tilde{f}_{n+1/2}$ are determined from the coefficients $\tilde{u}_{n+1/2}$ in RK2: by using (6.3) and (6.4). The AB3 method is started at $t = 0$ by assigning

$$\tilde{f}_{-2} = \tilde{f}_{-1} = \tilde{f}_0 = \tilde{F}(\tilde{u}_0; \mathbf{k}). \tag{6.8}$$

Thus, AB3 is effectively started with a forward Euler method.

The time-step size was chosen for both the 2-D ($N = 32$) and 3-D ($N = 16$) runs to be $\Delta t = 0.001$. Initial checks of the 2-D and 3-D codes were performed by explicitly checking the values of a few selected coefficients for several time-steps, and the long-term behavior of the codes was confirmed by the constancy of the integral invariants (to within canonical fluctuations). A comparison between ensemble prediction and numerical determination of the means and variances of the Fourier coefficients was thought to be another good test of code viability, but this had the implicit assumption that ideal homogeneous turbulence was ergodic. As the following discussion of results will show, this assumption was not correct.

6.2 2-D Simulations

We begin with 2-D simulations, run either on a Control Data Corporation Cyber 205 at NASA Langley or on one of the Cray 2 supercomputers then at NASA Ames [Shebalin 89]. These simulations were performed on a 32^2 grid, with $k_{min} = 1$ and $k_{max} = 15.08$; again, de-aliased nonlinear terms were produced using a shifted-grid method [Patterson 71]. Since $k_{max} = 15.08$, there are 227 independent modes for a 2-D Euler simulation, while there are twice this, 454 modes, for a 2-D ideal MHD simulation. Thus, the phase space for these 2-D Euler runs has 227 dimensions and for the 2-D ideal MHD runs has 454 dimensions.

The modal spectra for the various runs were initialized so that $E_K = E_M = 0.5$. The modes were assigned random initial phase and satisfied

$$|\tilde{\mathbf{u}}(\mathbf{k})|^2 \quad = \quad |\tilde{\mathbf{b}}(\mathbf{k})|^2 \quad \sim \quad k^4 \exp(-2k^2/k_{\mathrm{O}}^2). \tag{6.9}$$

Here, $k_{\mathrm{O}} = 2$ was used, although the exact value of k_{O} did not matter, as the system quickly evolved to 'thermodynamic equilibrium.'

Time-integration was performed with the RK2 method given in (6.5) and time-step size was $\Delta t = 0.001$. (The Euler runs were approximately 0.13 seconds/Δt, while the MHD runs were approximately 0.38 seconds/Δt.) A number of short runs were done, from $t = 0$ to $t = 10$ (10^4 time-steps), for preliminary analysis and to allow transients to subside. After this, three runs were continued from $t = 10$ to $t = 510$ (5×10^5 time-steps): NSP (an Euler run), CAI (ideal MHD, $B_{\mathrm{o}} = 0$), and CBK (ideal MHD, $\mathbf{B}_{\mathrm{o}} = B_{\mathrm{o}}\hat{\mathbf{x}}$, with $B_{\mathrm{o}} = 1$).

In order to determine expectation values for the modal spectra of two of these runs, the entropy functionals defined in Table 5.1 were minimized with respect to a variable parameter (Ψ' for run NSP and $\mathcal{E}'_M$ for CAI). At the minimum, $\Psi' = \Psi = \langle \Psi \rangle$ and $\mathcal{E}'_M = \mathcal{E}_M = \langle E_M \rangle$. Finding Ψ for run NSP allowed the inverse temperatures α and β to be found through (5.10) and (5.11), respectively; in turn, finding $\mathcal{E}_M$ for run CAI allowed α, β, and γ to be found through (5.40), (5.41) and (5.42), respectively. In the case of run CBK, no minimization is required because $\mathcal{E}_M = \mathcal{E}/2 = \langle E \rangle /2$, leading to $\gamma = 0$, as is known beforehand. In Figure 6.1 we show the entropy functionals $\sigma(\Psi)$ and $\sigma(R)$, corresponding to NSP and CAI, respectively, where $R = \mathcal{E}_M/(\mathcal{E} - \mathcal{E}_M)$. In this Figure, we have reduced the number of variables in the arguments of the functionals to display only the essential parameter. The

minima are $\Psi = 0.057397$ and $R = 1.0758$ ($\mathcal{E}_M = 0.52178$), for NSP and CAI, respectively, while *á priori* we know $R = 1$ for CBK.

The 'invariants' for these runs are: $\mathcal{E}$ and Ω for NSP; $\mathcal{E}$, $\mathcal{H}_C$, and $\mathcal{A}$ for CAI; $\mathcal{E}$ and $\mathcal{H}_C$ for CBK. The means and standard deviations (std. dev.) with respect to time for the various quantities are shown in Table 6.1.

NSP	$\mathcal{E}$	Ω	Ψ
Mean	0.50003	29.335	0.060871
Std. dev.	0.00001	0.0020	0.012804

CAI	$\mathcal{E}$	$\mathcal{H}_C$	$\mathcal{A}$	R
Mean	1.0068	0.23996	0.50000	1.0865
Std. dev.	0.0043	0.00002	0.00000	0.0677

CBK	$\mathcal{E}$	$\mathcal{H}_C$	$\mathcal{A}$	R
Mean	1.0015	0.0040135	0.013076	1.0025
Std. dev.	0.0009	0.0000045	0.001757	0.0736

Table 6.1: Parameters for 2-D runs, from $t = 10$ to $t = 510$. The predicted values are $\Psi = 0.057397$ for NSP, $R = 1.0758$ for CAI and $R = 1$ for CBK.

It is clear from this Table that the 'invariants' are invariant to within small fluctuations, while the noninvariant quantities in each case fluctuate considerably (percent fluctuation $\equiv$ 100%×std. dev./mean). In particular, the invariants fluctuate less than about 0.1%, while Ψ and R fluctuate about 20% and 7%, respectively. Also, $\mathcal{A}$ has 0% fluctuation for CAI, while it fluctuates about 13% for run CBK, where it is not an invariant.

We next compare the modal kinetic and magnetic energies determined by numerical simulation with their canonical ensemble predictions. To accomplish this, the time-averages and standard deviations of all modes in the runs NSP, CAI, and CBK were determined from $t_1 = 10$ up to $t_2 = 510$, for a maximum period of $\tau = t_2 - t_1 = 500$. In these 2-D runs, the primary modes were those of scalar vorticity $\tilde{\omega}(\mathbf{k})$ and magnetic scalar potential $\tilde{a}(\mathbf{k})$.

Over a period of time τ, the averages $\langle\tilde{\omega}(\mathbf{k})\rangle_{avg,\tau}$ and standard deviations $\langle\tilde{\omega}(\mathbf{k})\rangle_{std,\tau}$ of the vorticity coefficients are

$$\langle\tilde{\omega}(\mathbf{k})\rangle_{avg,\tau} \equiv \frac{1}{\tau}\int_{t_1}^{t_2}\tilde{\omega}(\mathbf{k})\,dt \tag{6.10}$$

$$\langle\tilde{\omega}(\mathbf{k})\rangle^2_{std,\tau} \equiv \frac{1}{\tau}\int_{t_1}^{t_2}\left|\tilde{\omega}(\mathbf{k}) - \langle\tilde{\omega}(\mathbf{k})\rangle_{avg,\tau}\right|^2 dt. \tag{6.11}$$

Similarly, the averages $\langle\tilde{a}(\mathbf{k})\rangle_{avg,\tau}$ and standard deviations $\langle\tilde{a}(\mathbf{k})\rangle_{std,\tau}$ with respect to time

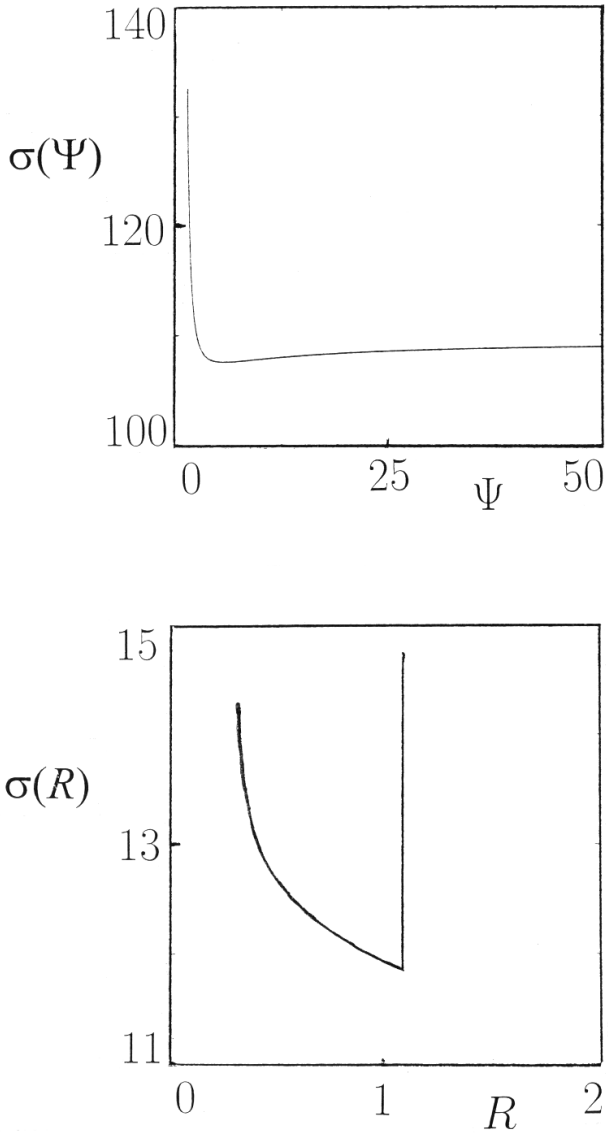

Figure 6.1: Entropy functionals – top: NSP, bottom: CAI; the minima are $\Psi = 0.057397$ and $R = 1.0758$ for NSP and CAI, respectively.

of the magnetic potential coefficients are

$$\langle \tilde{a}(\mathbf{k}) \rangle_{avg,\tau} \equiv \frac{1}{\tau} \int_{t_1}^{t_2} \tilde{a}(\mathbf{k})\, dt \tag{6.12}$$

$$\langle \tilde{a}(\mathbf{k}) \rangle_{std,\tau}^2 \equiv \frac{1}{\tau} \int_{t_1}^{t_2} \left| \tilde{a}(\mathbf{k}) - \langle \tilde{a}(\mathbf{k}) \rangle_{avg,\tau} \right|^2 dt. \tag{6.13}$$

Note also that the averages and standard deviations (squared) defined here for each coefficient can obviously be split into averages and standard deviations (squared) of the real and imaginary parts of the coefficients individually, if so desired.

The average $E_K^{avg,\tau}(\mathbf{k})$, random $E_K^{ran}(\mathbf{k})$, and total $E_K^{tot}(\mathbf{k})$ kinetic energies associated with each mode over a given period of time τ are

$$E_K^{avg,\tau}(\mathbf{k}) = k^{-2} |\, \langle \tilde{\omega}(\mathbf{k}) \rangle_{avg,\tau} \,|^2 \tag{6.14}$$

$$E_K^{ran,\tau}(\mathbf{k}) = k^{-2} \langle \tilde{\omega}(\mathbf{k}) \rangle_{std,\tau}^2 \tag{6.15}$$

$$E_K^{tot,\tau}(\mathbf{k}) = E_K^{avg,\tau}(\mathbf{k}) + E_K^{ran,\tau}(\mathbf{k}). \tag{6.16}$$

Similarly, the average (or *coherent*) $E_M^{avg,\tau}(\mathbf{k})$, random $E_M^{ran}(\mathbf{k})$, and total $E_M^{tot}(\mathbf{k})$ magnetic energies associated with each mode over a period τ are

$$E_M^{avg,\tau}(\mathbf{k}) = k^2 |\, \langle \tilde{a}(\mathbf{k}) \rangle_{avg,\tau} \,|^2 \tag{6.17}$$

$$E_M^{ran,\tau}(\mathbf{k}) = k^2 \langle \tilde{a}(\mathbf{k}) \rangle_{std,\tau,\tau}^2 \tag{6.18}$$

$$E_M^{tot,\tau}(\mathbf{k}) = E_M^{avg,\tau}(\mathbf{k}) + E_M^{ran,\tau}(\mathbf{k}). \tag{6.19}$$

Adding the kinetic and magnetic parts gives the modal total energy:

$$E^{avg,\tau}(\mathbf{k}) = E_K^{avg,\tau}(\mathbf{k}) + E_M^{avg,\tau}(\mathbf{k}) \tag{6.20}$$

$$E^{ran,\tau}(\mathbf{k}) = E_K^{ran,\tau}(\mathbf{k}) + E_M^{ran,\tau}(\mathbf{k}) \tag{6.21}$$

$$E^{tot,\tau}(\mathbf{k}) = E_K^{tot,\tau}(\mathbf{k}) + E_M^{tot,\tau}(\mathbf{k}). \tag{6.22}$$

(Here we have used the relations $\langle \tilde{\omega}(\mathbf{k}) \rangle_{std,\tau} = |\, \langle \tilde{\omega}(\mathbf{k}) \rangle_{std,\tau} \,|$ and $\langle \tilde{a}(\mathbf{k}) \rangle_{std,\tau} = |\, \langle \tilde{a}(\mathbf{k}) \rangle_{std,\tau} \,|$.)

We can now plot these time-averaged modal energies versus the 2-D vector $\mathbf{k}$ and compare them to each other and to canonical ensemble predictions. This is done in Figures 6.2, 6.3, 6.4, and 6.5. Figure 6.2 consists of modal total energies (6.20), (6.21), and (6.22) averaged from $t_1 = 10$ to $t_2 = 60$ ($\tau = 50$) for runs NSP, CAI, and CBK. Figure 6.3 consists of modal

total (*i.e.*, kinetic) energies for run NSP averaged from $t_1 = 10$ to $t_2 = 510$ ($\tau = 500$). Figures 6.2 and 6.3 have four parts: The first three represent numerical simulation results: 1) $E^{avg,\tau}(\mathbf{k})$, 2) $E^{ran,\tau}(\mathbf{k})$, and 3) $E^{tot,\tau}(\mathbf{k})$. Number 4 is the ensemble prediction for modal total energy $E^{tot,\tau}(\mathbf{k})$; this is purely random, since according to canonical ensemble theory $E^{avg,\tau}(\mathbf{k}) = 0$, so that $E^{tot,\tau}(\mathbf{k}) = E^{ran,\tau}(\mathbf{k})$.

In Figure 6.2 ($\tau = 50$), some of the modal average energies seem rather large. In looking at Figure 6.3 ($\tau = 500$), we see that, for run NSP at least, those modal average energies which appeared large at $\tau = 50$ have become considerably smaller. Also, Figure 6.2 ($\tau = 50$) clearly shows that for run CBK ($B_\mathrm{o} = 1$) it is only those modes with $k_x = 0$ that have appreciable modal average energies. This is due to the presence of Alfvén waves, which make the phase φ of the Fourier coefficients continually sweep through all possible values $0 \leq \varphi < 2\pi$ with the Alfvén frequency $k^x B_\mathrm{o} = k_x$ for each mode corresponding to $\mathbf{k}$. (Alfvén waves are discussed in subsection 3.2.3.)

Figures 6.4 and 6.5 consist of modal kinetic and magnetic energies averaged from $t_1 = 10$ to $t_2 = 510$ ($\tau = 500$) for runs CAI and CBK. Figures 6.4 and 6.5 have four parts. The first three represent numerical simulation results: 1) $E_K^{avg,\tau}(\mathbf{k})$ or $E_M^{avg,\tau}(\mathbf{k})$; 2) $E_K^{ran,\tau}(\mathbf{k})$ or $E_M^{ran,\tau}(\mathbf{k})$; and 3) $E_K^{tot,\tau}(\mathbf{k})$ or $E_M^{tot,\tau}(\mathbf{k})$. Number 4 is the ensemble prediction for $E_M^{ran,\tau}(\mathbf{k})$ $= E_K^{tot,\tau}(\mathbf{k})$; again, this is purely random according to canonical ensemble theory.

In looking at Figure 6.3 (run NSP, $\tau = 500$), we see that the time average part of the Fourier coefficients has become much smaller than what they were in Figure 6.2 (run NSP, $\tau = 50$). In Figure 6.3 (run NSP, $\tau = 500$), it is also clear that the random part produced by the numerical experiment is quite similar to the ensemble prediction. However, in looking at Figures 6.4 and 6.5, corresponding to the two ideal MHD runs CAI and CBK, respectively, we see that there is a significant amount of energy in $E_K^{avg,\tau}(\mathbf{k})$ and $E_M^{avg,\tau}(\mathbf{k})$, particularly at the lower $|\mathbf{k}|$ values. In fact, these have not changed much from Figure 6.2 (runs CAI and CBK, $\tau = 50$). Since the canonical ensemble prediction is that $E_K^{avg,\tau}(\mathbf{k})$ and $E_M^{avg,\tau}(\mathbf{k})$ are identically zero, something is amiss.

It may be asked whether or not the time allowed for the numerical simulations to run was long enough. To answer this question, we look at the evolution of the total *coherent energy*:

$$E_K^C(\tau) = \sum_{\mathbf{k}\in\mathcal{K}'} E_K^{avg,\tau}(\mathbf{k}) \tag{6.23}$$

$$E_M^C(\tau) = \sum_{\mathbf{k}\in\mathcal{K}'} E_M^{avg,\tau}(\mathbf{k}). \tag{6.24}$$

For runs NSP, CAI, and CBK, the coherent energies, $E_K^C(\tau)$ and $E_M^C(\tau)$, have been averaged from $\tau = 50$ to $\tau = 500$, in steps of $\delta\tau = 50$. If these running averages do not appear to be converging to some constant value, then we have not run the simulations long enough; if they do appear to converge to some constant value, then we may believe that we have averaged long enough. The running averages of the coherent energies $E_K^C(\tau)$ and $E_M^C(\tau)$, with respect to averaging time τ, is shown in Figure 6.6.

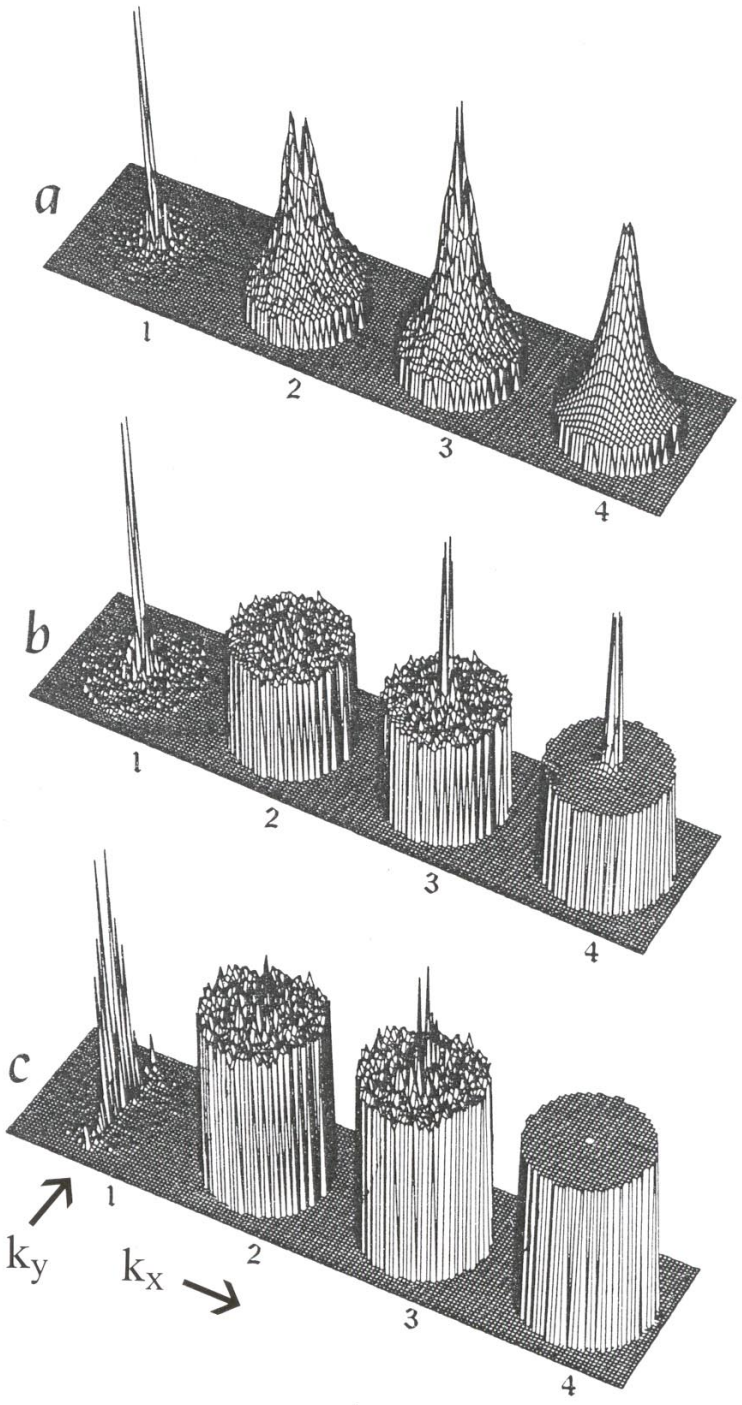

Figure 6.2: Runs NSP, CAI, and CBK – 2-D time-averaged modal energies: **1** average, **2** random, **3** total; number **4** is the ensemble prediction, which is purely random; averaging time: $\tau = 50$.

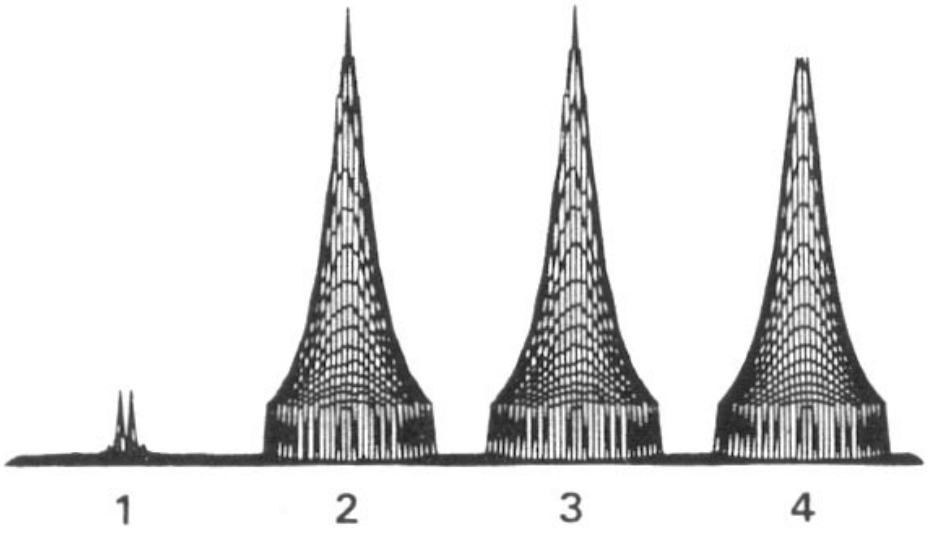

Figure 6.3: Run NSP – 2-D Euler time-averaged modal kinetic energies: **1** average, **2** random, **3** total; number **4** is the ensemble prediction, which is purely random; averaging time: $\tau = 500$.

It is clear in Figure 6.6 that simulations NSP, CAI, and CBK have been run long enough so that the stationary values of the coherent energies are apparent. In the case of run NSP, the coherent energy $E_K^C(\tau)$ appears to be converging monotonically to zero. In this 2-D Euler simulation, time-averages appear to match the ensemble prediction. However, in both of the runs CAI and CBK, the coherent energies $E_K^C(\tau)$ and $E_M^C(\tau)$ are not converging to zero, but instead to some significantly nonzero values. Thus, for runs CAI and CBK, numerical time averages do not appear to match the ensemble prediction. In these 2-D ideal MHD simulations, we must therefore conclude that we have evidence for *nonergodicity* in ideal homogeneous, MHD turbulence.

To study the implications of this more closely, we can examine the behavior of single Fourier coefficients. A Fourier coefficient has a real and an imaginary part, and we can plot one versus the other from $t_1 = 10$ to $t_2 = 510$; this produces a 'random walk' on a 2-D phase surface. In the case of run NSP, the resulting plot is a projection of the 227-dimensional phase trajectory onto a 2-D plane, while for runs CAI and CBK, the resulting plot is a projection of the 454-dimensional phase trajectory onto a 2-D plane. Here, we will look at only the ideal MHD runs CAI and CBK, since it is in these runs that nonergodicity appears to be manifested.

For run CAI, Figure 6.7 shows the evolution of the real versus the imaginary parts of $\tilde{\omega}(\mathbf{k})$ for $\mathbf{k} = (1,0)$ and $\mathbf{k} = (0,1)$, while Figure 6.8 shows the evolution the real versus the imaginary parts of $\tilde{j}(\mathbf{k}) = \tilde{a}(\mathbf{k})$, also for $\mathbf{k} = (1,0)$ and $\mathbf{k} = (0,1)$. Analogous plots for run CBK are given in Figures 6.9 and 6.10. (Absolute scales in these Figures are omitted as

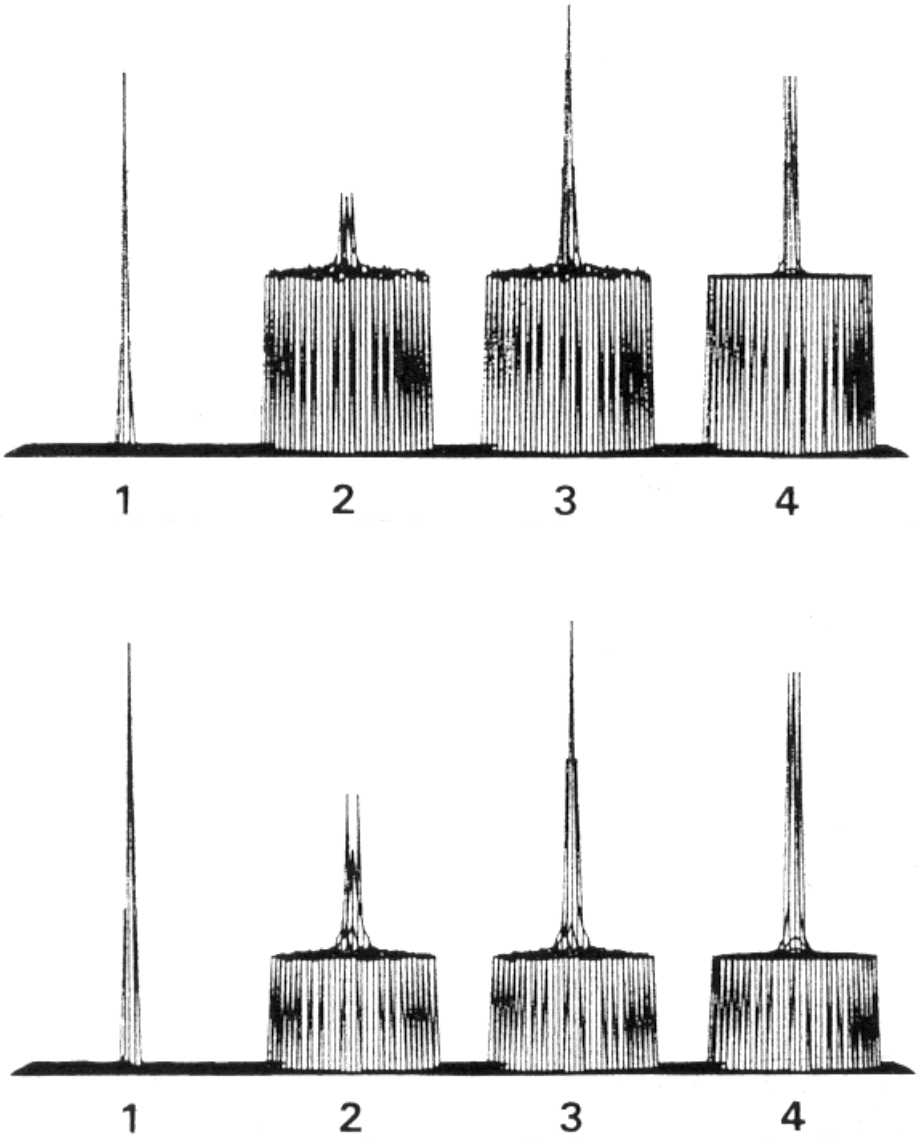

Figure 6.4: Run CAI – 2-D ideal MHD ($B_o = 0$) time-averaged energies: **1** average, **2** random, **3** total; number **4** is the ensemble prediction, which is purely random; top: kinetic, bottom: magnetic; the scale is different between top and bottom; averaging time: $\tau = 500$.

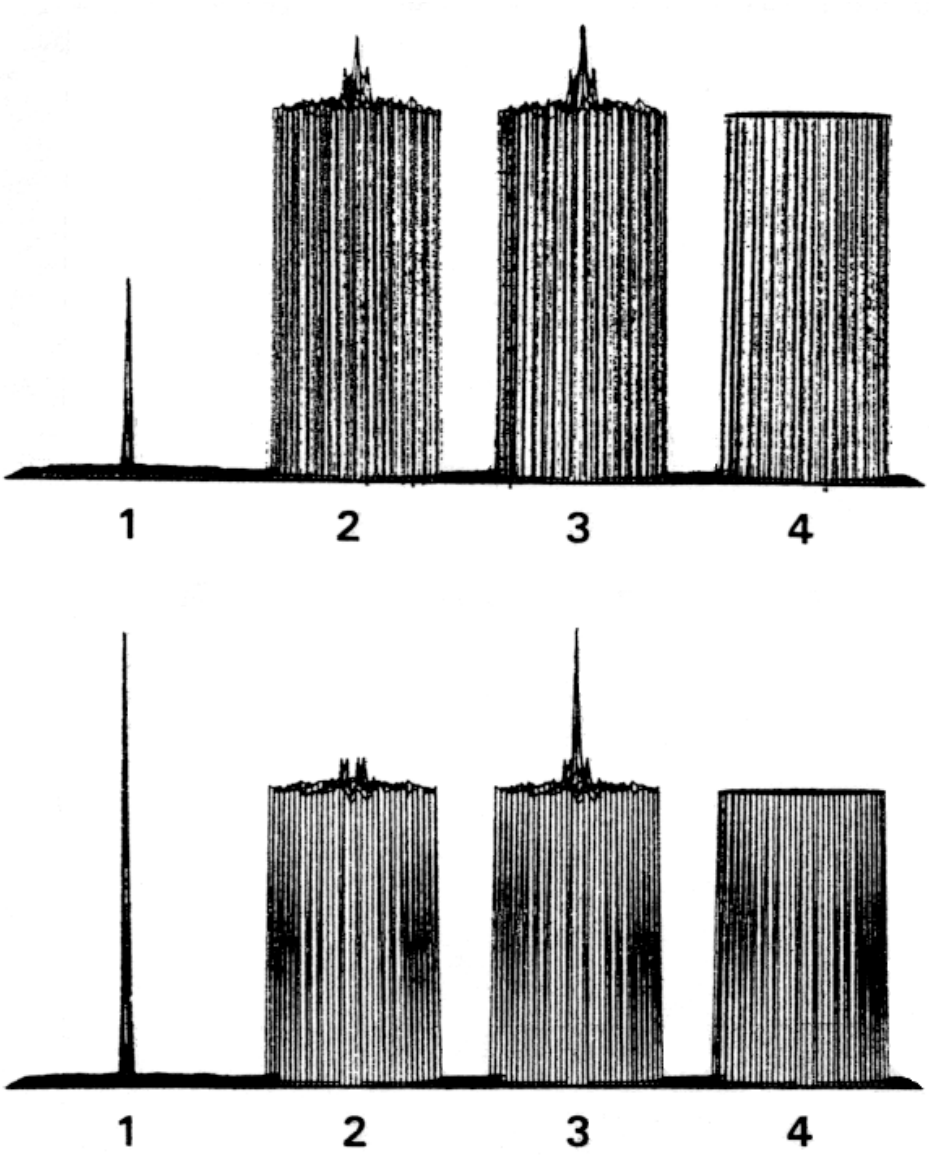

Figure 6.5: Run CBK – 2-D ideal MHD ($B_o = 1$) time-averaged energies: **1** average, **2** random, **3** total; number **4** is the ensemble prediction, which is purely random; top: kinetic, bottom: magnetic; the scale is different between top and bottom; averaging time: $\tau = 500$.

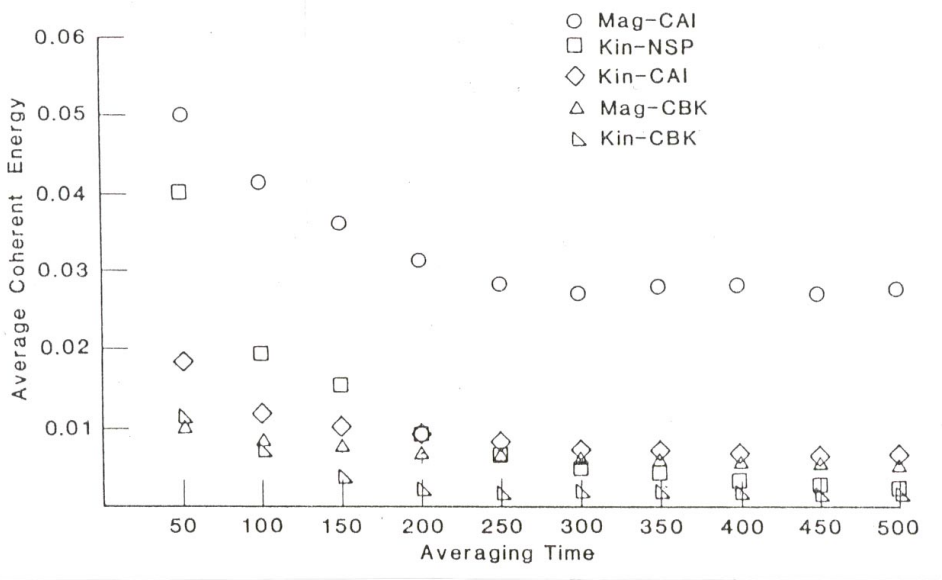

Figure 6.6: Coherent energies for three cases of 2-D ideal turbulence: NSP (Euler), CAI (MHD, $B_o = 0$), and CBK (MHD, $B_o = 1$) – Kin: kinetic; Mag: magnetic.

being unimportant to the discussion at hand.) These four Figures clearly show that the phase trajectories for ideal MHD, with either $B_m = 0$ or $B_m = 1$, are not centered on the origin in phase space, as predicted by canonical ensemble theory. This gives further concrete evidence for nonergodicity in 2-D ideal MHD turbulence.

The main difference between runs CAI and CBK is that CAI has no mean magnetic field present ($B_o = 0$), while CBK does have a mean field ($B_o = 1$). In the discussion in subsection 3.2.3, it was shown that if $\mathbf{B}_o = B_o\hat{\mathbf{x}}$, with $B_o \neq 0$, then Alfvén waves are present for those modes with $k_x \neq 0$. In the limit of large B_o, equation (3.54) describes the modal dynamics and the appearance of the trajectories in Figures 6.9 and 6.10 would be purely circular. For moderate values of B_o, we would expect that nonlinear modal interactions would modulate the amplitude of the Alfvén waves, and that is what we see in Figures 6.9 and 6.10, for those modes with $B_o \neq 0$. These 'nonlinear Alfvén waves' appear for all modes with $k_x \neq 0$ when $B_o \neq 0$, and not in those modes with $k_x = 0$, as indicated by Figures 6.9 and 6.10.

The presence of nonlinear Alfvén waves means that the associated modal averages will be zero. This explains the series of spikes for run CBK along the k_y axis in Part 1 of Figure 6.2, which gives the average modal energies for $\tau = 50$. In looking at Figure 6.5, it is clear that these spikes are still there along the k_y axis, and nowhere else. (The perspective of Figure 6.5 is essentially down the k_y axis; the perspective in Figure 6.2 more clearly shows the 'fence of spikes' along the k_y axis.)

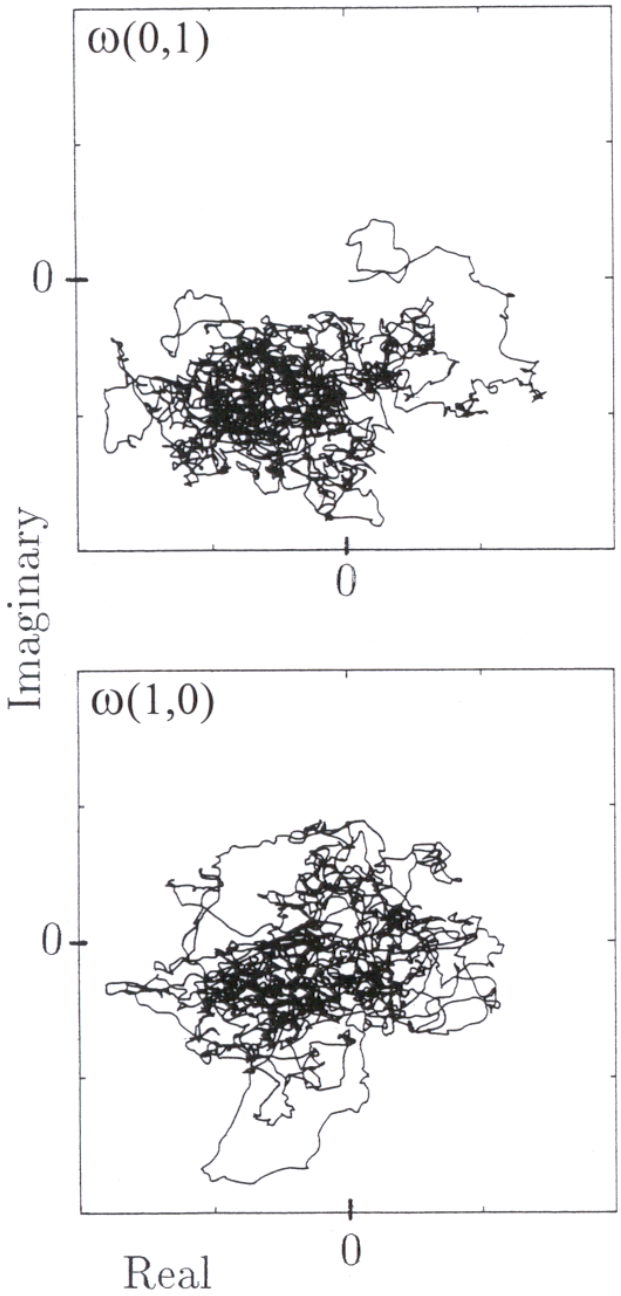

Figure 6.7: Run CAI: 2-D ideal MHD ($B_o = 0$), projection of phase trajectory; top: $\tilde{\omega}_R(0,1)$ vs $\tilde{\omega}_I(0,1)$, bottom: $\tilde{\omega}_R(1,0)$ vs $\tilde{\omega}_I(1,0)$.

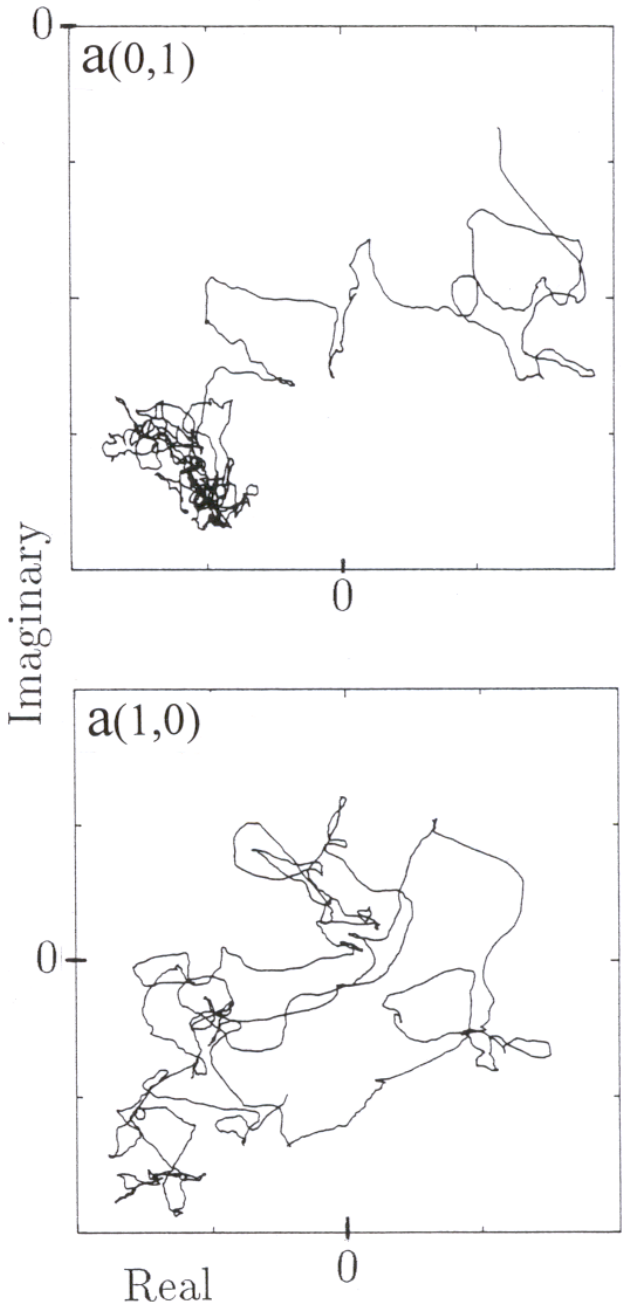

Figure 6.8: Run CAI: 2-D ideal MHD ($B_o = 0$), projection of phase trajectory; top: $\tilde{a}_R(0,1)$ vs $\tilde{a}_I(0,1)$, bottom: $\tilde{a}_R(1,0)$ vs $\tilde{a}_I(1,0)$.

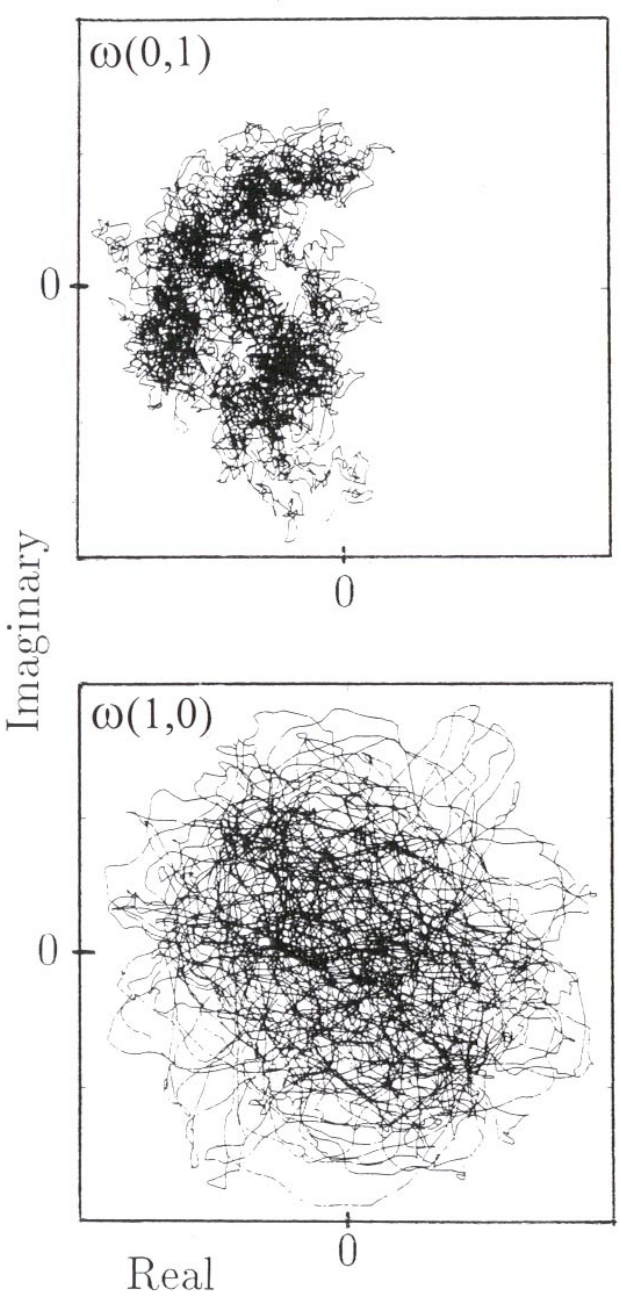

Figure 6.9: Run CBK: 2-D ideal MHD ($B_o = 1$); projection of the phase trajectory; top: $\tilde{\omega}_R(0,1)$ vs $\tilde{\omega}_I(0,1)$, bottom: $\tilde{\omega}_R(1,0)$ vs $\tilde{\omega}_I(1,0)$.

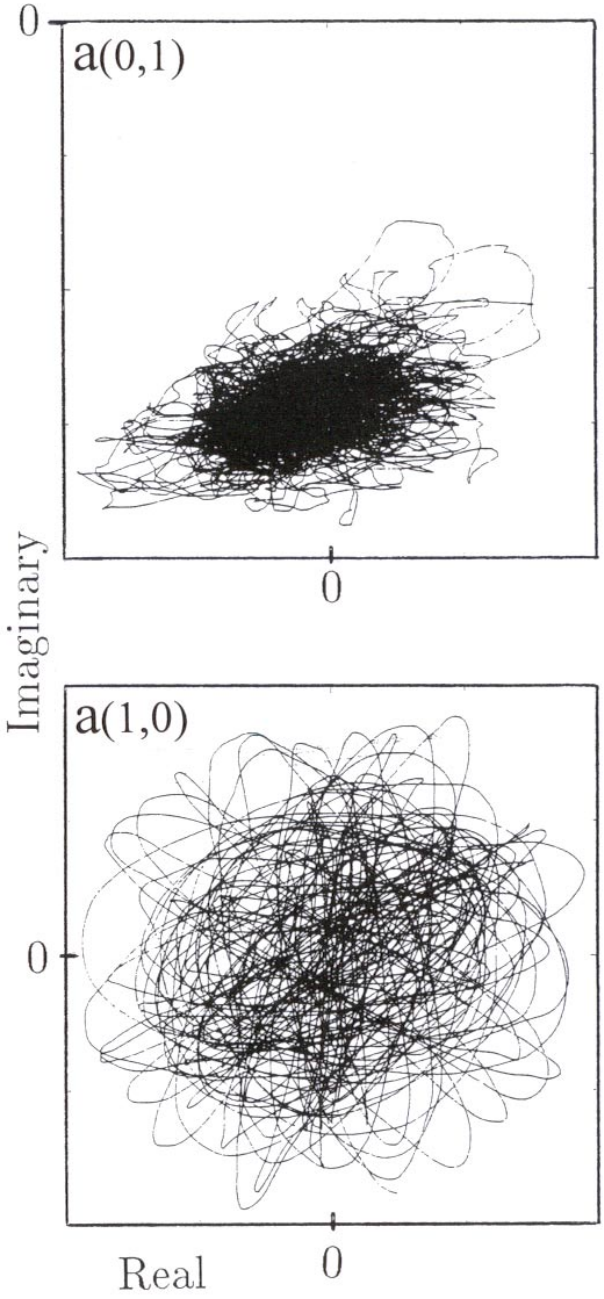

Figure 6.10: Run CBK: 2-D ideal MHD ($B_o = 1$); projection of the phase trajectory; top: $\tilde{a}_R(0,1)$ vs $\tilde{a}_I(0,1)$, bottom: $\tilde{a}_R(1,0)$ vs $\tilde{a}_I(1,0)$.

6.3 3-D Simulations

A series of 3-D simulations was also undertaken, run on a Cray YMP at NASA Langley [Shebalin 94]. These simulations were performed on a 16^3 grid, with $k_{min} = 1$ and $k_{max} = 7.542$; de-aliased nonlinear terms were again produced using a shifted-grid method [Patterson 71]. Since $k_{max} = 7.542$, there are 428 independent modes for a 3-D Euler simulation, while there are twice this, 856 modes, for a 3-D ideal MHD simulation. The phase space for 3-D Euler runs thus has 428 dimensions and for 3-D ideal MHD runs has 856 dimensions. The initial condition were as described by (6.9).

Time-integration was performed with the AB3 method, given in (6.6) and (6.7), and time-step size was $\Delta t = 0.001$; a few cases were rerun with the RK2 method (6.5), also with $\Delta t = 0.001$; the results were essentially the same. Although AB3 required slightly more run-time memory than RK2, the computer execution time per Δt was about half as long for AB3 as for RK2: 0.12 sec/Δt vs. 0.25 sec/Δt for the Euler runs, and 0.35 sec/Δt vs. 0.71 sec/Δt for the ideal MHD runs. Overall, AB3 seems to be the more efficient method.

Four 'short' runs were done, from $t = 0$ to $t = 250$ (2.5×10^5 time-steps), and four 'long' runs from $t = 0$ to at least $t = 750$ (7.5×10^5 time-steps). The runs are as follows (at the end of the run identifiers, 'A' and 'R' stand for AB3 and RK2, respectively). The short runs, which will not be discussed in much detail here, were: E1A (Euler, $H_K \approx 0$), E2R (Euler), M1R (ideal MHD, $B_o = 0$), and M3A (ideal MHD, $B_o = 0$, $k_{min} = 2$). The long runs were: E2A (Euler), M1A (ideal MHD, $B_o = 0$), M2A (ideal MHD, $B_o = 0$, small H_M), and M4A (ideal MHD, $\mathbf{B}_o = B_o\hat{\mathbf{x}}$, with $B_o = 1$). The characteristics of these runs are shown in Table 6.2. The time-step size ($\Delta t = 0.001$) was sufficiently small so that the integral invariant values listed in Table 6.2 varied only by a few parts per million during any of the runs.

Run	k_{min}^2	B_o	Time	$\mathcal{E}$	$\mathcal{H}_K$	$\mathcal{H}_C$	$\mathcal{H}_M$
E1A	1	···	250	0.5000	−0.04443	···	···
E2A	1	···	750	0.5000	3.142	···	···
E2R	1	···	250	0.5000	3.142	···	···
M1A	1	0	1000	1.0000	···	0.1326	0.2129
M1R	1	0	250	1.0000	···	0.1326	0.2129
M2A	1	0	750	1.0000	···	0.1326	0.09973
M3A	2	0	250	0.9983	···	0.1258	0.09899
M4A	1	1	750	1.0000	···	0.1326	···

Table 6.2: Parameters for the 3-D runs.

In Table 6.2, E2A and E2R had the same initial conditions, as did runs M1A and M1R; these pairs of runs were done to compare the two different numerical integration methods, AB3 and RK2. As will be seen ahead in Tables 6.3 and 6.5, the two different methods produce essentially the same results (AB3 being twice as fast per time-step as RK2). Runs

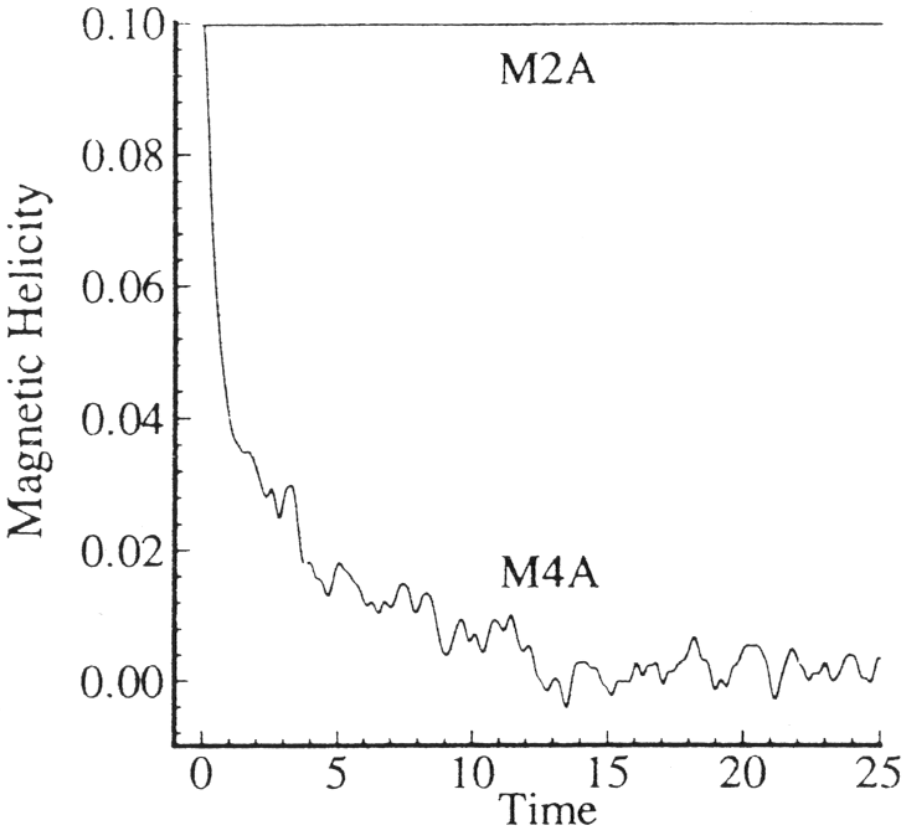

Figure 6.11: Time evolution of magnetic helicity for 3-D ideal MHD runs M2A ($B_o = 0$) and M4A ($B_o = 1$).

M2A, M3A, and M4A had the same initial conditions, except that Run M3A had the k^2 =1 coefficients set to zero; since M3A had $k^2_{min} = 2$, the k^2 =1 coefficients did not evolve with time. Run M3A was used to test the effect of raising k_{min} from 1 to 2; as is evident in Tables 6.3 and 6.5, there were some slight effects, but no major ones.

Although runs M2A and M4A had the same initial conditions, run M4A had a mean magnetic field present ($B_o = 1$), while run M2A did not ($B_o = 0$). The expectation, from canonical ensemble theory, was that the magnetic helicity H_M would be invariant for M2A but not for M4A. This prediction was borne out, as is clearly seen in Figure 6.11.

In Table 6.3 we show the inverse temperatures α, β, and γ associated with each of the runs in Table 6.2. The inverse temperatures are parameterized by Ω, for 3-D Euler turbulence, and by $\mathcal{E}_M$, or equivalently by $R = \mathcal{E}_M/\mathcal{E}_K$, for 3-D ideal MHD turbulence, as detailed in Section 5.1. Ensemble predictions and time averages were seen to be qualitatively different in the 2-D runs just discussed, and, as will be seen shortly, they are also qualitatively different

in the 3-D runs.

In the 3-D runs, the inverse temperatures α, β and γ were determined by minimizing the root-mean-square (RMS) difference between ensemble and simulation modal energies: for the Euler runs, Ω was varied to find a value Ω_{RMS} which produce minimization, and for the ideal MHD runs, R was varied to find the value R_{RMS} which provided minimization. These values of Ω_{RMS} and R_{RMS} are given, along with the corresponding inverse temperatures α, β and γ, for each of the runs in Table 6.3.

Run	Ω_{RMS}	R_{RMS}	α	β	γ
E1A	17.08	$\cdots$	2.624	0.006825	$\cdots$
E2A	23.74	$\cdots$	15.58	-2.062	$\cdots$
E2R	23.79	$\cdots$	15.41	-2.035	$\cdots$
M1A	$\cdots$	1.506	1.774	-0.7825	-1.682
M1R	$\cdots$	1.506	1.773	-0.7824	-1.681
M2A	$\cdots$	1.206	1.547	-0.7142	-1.451
M3A	$\cdots$	1.301	1.616	-0.7205	-2.131
M4A	$\cdots$	1.000	1.401	-0.7075	$\cdots$

Table 6.3: Inverse temperatures for the 3-D runs.

Although the full 3-D spectra are not easily displayed as the full 2-D spectra (see Figures 6.2, 6.3, 6.4, and 6.5) we can still get a crude measure of how well canonical predictions and numerical averages compare. This is done by defining 'directionally averaged' power spectra as follows:

$$E_k(k) \equiv \frac{1}{2n_k} \sum_{|\mathbf{k}|=k} \left\langle |\tilde{\mathbf{u}}(\mathbf{k})|^2 \right\rangle_{avg} \tag{6.25}$$

$$E_m(k) \equiv \frac{1}{2n_k} \sum_{|\mathbf{k}|=k} \left\langle |\tilde{\mathbf{b}}(\mathbf{k})|^2 \right\rangle_{avg} . \tag{6.26}$$

The quantity n_k is the number of kinematically nonzero modes with $|\mathbf{k}| = k$ and the averaging time is the total simulation time for the run in question. Figure 6.12 shows the directionally averaged power spectra for runs M2A and M3A. Here we see two things: First, the value of k_{min} is not critical ($k_{min} = 1$ for M2A and $k_{min} = \sqrt{2}$ for M3A). Second, there is a small but nonnegligible difference between canonical predictions and numerical averages, which bears further investigation. (In fact, it was the persistence of such differences in early 2-D MHD simulations [Shebalin 82, Shebalin 83] which first indicated the need for a closer look.)

At this point, we again study the behavior of single Fourier coefficients with respect to time. In Figure 6.13, we plot real versus imaginary parts for each of the coefficients $\tilde{\omega}_y(1,0,0)$, $\tilde{\omega}_z(1,0,0)$, $\tilde{b}_y(1,0,0)$ and $\tilde{b}_z(1,0,0)$, from $t_1 = 1$ to $t_2 = 1000$ for run M1A. This is an MHD run, so the phase space has a dimension of 856. It is clear from Figure 6.13 that nonergodicity

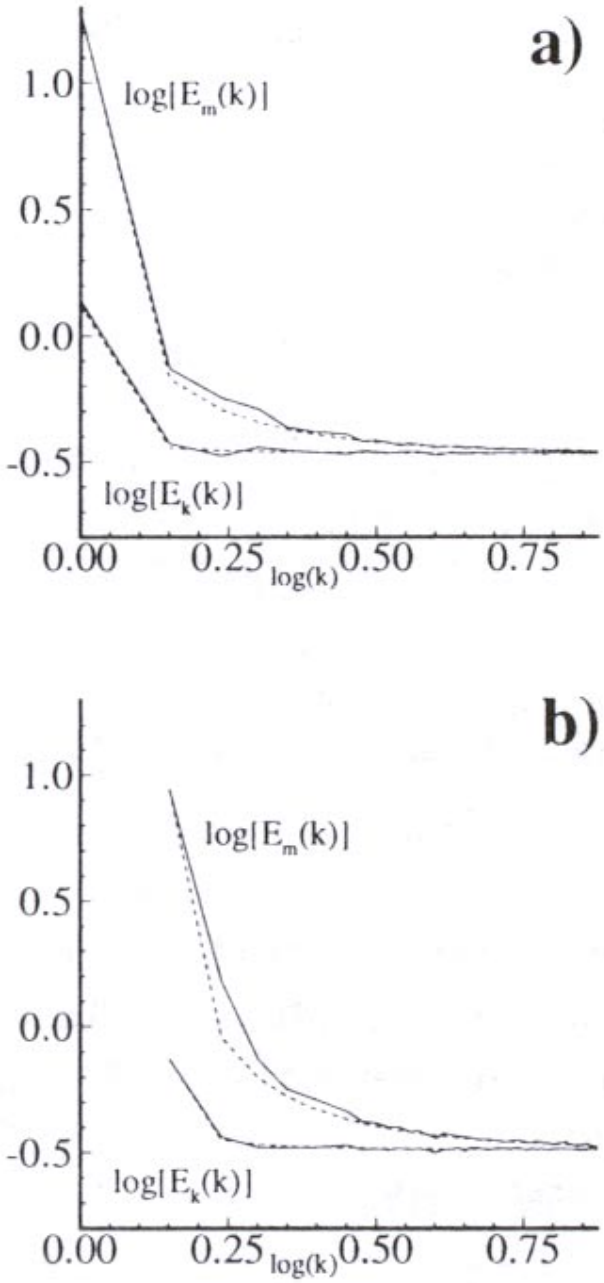

Figure 6.12: Directionally-averaged spectra for a)M2A and b)M3A (MHD, $B_o = 0$), theoretical: dashed line, numerical: solid line ($\log \equiv \log_{10}$).

is again present, as significant mean-values (in comparison with the standard deviations) are apparent. Also, in Figure 6.13, the coefficients appear to have the relationships

$$\begin{aligned} \tilde{\omega}_y(1,0,0) &\cong -i\tilde{\omega}_z(1,0,0) \\ \tilde{b}_y(1,0,0) &\cong -i\tilde{b}_z(1,0,0). \end{aligned} \tag{6.27}$$

We also have the approximate similarity

$$\begin{aligned} \tilde{\omega}_y(1,0,0) &\sim \tilde{b}_y(1,0,0) \\ \tilde{\omega}_z(1,0,0) &\sim \tilde{b}_z(1,0,0). \end{aligned} \tag{6.28}$$

In fact, all coefficients with $k^2 = 1$ in runs M1A and M2A ($B_o = 0$) have this strong relationship. A quantitative measure of the strength of these apparent relationships can be achieved by finding the average modal correlation, defined as

$$C(\mathbf{v}, \mathbf{w}; k^2) = \frac{1}{n(k^2)} \sum_{|\mathbf{k}|^2 = k^2} \frac{1}{\tau} \int_0^\tau \frac{\tilde{\mathbf{v}}(\mathbf{k}, t) \cdot \tilde{\mathbf{w}}^*(\mathbf{k}, t)}{|\tilde{\mathbf{v}}(\mathbf{k}, t)|\, |\tilde{\mathbf{w}}^*(\mathbf{k}, t)|} dt. \tag{6.29}$$

Here, $n(k^2)$ is the number of coefficients with a set value of k^2, and τ is the averaging time. We draw $\mathbf{v}$ and $\mathbf{w}$ from the set $\mathbf{b}$, $\mathbf{j}$, $\mathbf{u}$ and $\boldsymbol{\omega}$; the average modal correlations, as defined by (6.29), for the first three values of k^2 are given in Table 6.4.

Run	B_o	τ	k^2	$C(\mathbf{j}, \mathbf{b}; k^2)$	$C(\mathbf{u}, \mathbf{b}; k^2)$	$C(\mathbf{u}, \boldsymbol{\omega}; k^2)$
M1A	0	1000	1	0.990	0.896	0.769
			2	0.558	0.283	0.0497
			3	0.439	0.236	0.0258
M2A	0	750	1	0.954	0.776	0.581
			2	0.535	0.269	0.0417
			3	0.427	0.231	0.0208
M4A	1	750	1	0.0180	0.239	0.0745
			2	0.00456	0.215	−0.00322
			3	−0.0154	0.211	−0.0195

Table 6.4: Average modal correlations versus k^2 for three 3-D ideal MHD runs.

It is clear in looking at Table 6.4 that the k^2 =1 modes are strongly correlated for $B_o = 0$, but not for $B_o = 1$. The average modal correlations between $\mathbf{j}$ and $\mathbf{b}$ and between $\mathbf{u}$ and $\mathbf{b}$ for $k^2 = 2, 3$ are decreasing but still substantial for $B_o = 0$; this is a reflection that H_M and H_C are invariants for $B_o = 0$. In contrast, the correlation for $k^2 = 2, 3$ between $\mathbf{u}$ and $\boldsymbol{\omega}$ for $B_o = 0$ is negligible (a reflection that H_K is not an invariant for ideal MHD). In the $B_o = 1$ case, only $\mathbf{u}$ and $\mathbf{b}$ appear correlated, and then only moderately; for $B_o = 1$, H_C is invariant but H_M and H_K are not. These results suggest that $\mathbf{u} \sim \nabla \times \mathbf{u}$ and $\mathbf{b} \sim \nabla \times \mathbf{b}$,

i.e., the fields **u** and **b** are tending toward *force-free* configurations, but only for $B_o = 0$ and only for the lowest values of k^2. We thus have a 'low-k^2, quasi-force-free flow' as a long-term state of an ideal magnetofluid with no mean field. (Data allowing similar conclusions for the Euler runs were not gathered.)

Run	E_K^C	E_M^C	H_K^C	H_C^C	H_M^C
E1A	0.00301	$\cdots$	-0.00110	$\cdots$	$\cdots$
E2A	0.0416	$\cdots$	0.305	$\cdots$	$\cdots$
E2R	0.0413	$\cdots$	0.303	$\cdots$	$\cdots$
M1A	0.0880	0.179	$\cdots$	0.0364	0.177
M1R	0.0919	0.172	$\cdots$	0.0365	0.170
M2A	0.00562	0.0656	$\cdots$	0.0158	0.0635
M3A	0.00464	0.0542	$\cdots$	0.0126	0.0368
M4A	0.00146	0.00148	$\cdots$	0.000421	0.0000955

Table 6.5: Coherency for 3-D runs for $\tau = 250$.

Coherent energies for the 3-D runs can be defined in exactly the same way as for the 2-D runs, *i.e.*, by (6.23) and (6.24). Furthermore, coherent helicities can be similarly defined, by using the time-averaged values of the Fourier coefficients in their calculation. Table 6.5 presents the coherent energy and helicity values for an averaging time of $\tau = 250$. Runs M1A and M1R, in particular, appear to have a substantial amount of coherency – about 27% in both energy and cross helicity, and 83% in coherent magnetic helicity!

The high levels of coherent energy at $\tau = 250$, however, may decrease as the simulations are allowed to run longer in time. Figure 6.14 shows values of the coherent energies for the runs which ran to at least $t = 750$. In this Figure, the coherency in runs M1A and M2A appears to have reached a stationary value, while the coherency of runs E2A and M4A appears to be on the verge of reaching asymptotic steady values. In the case of run E2A, the behavior of the coherent energy during the time covered by Figure 6.14 is approximately fit by the following formula:

$$E_K^C \approx 0.012 + 0.033\, e^{-t/237}. \tag{6.30}$$

Thus, the coherent energy for run E2A seems to be asymptotically approaching $E_K^C \approx 0.012$, or 2.4% of the total energy of run E2A, as $t \to \infty$.

6.4 Discussion of Numerical Results

Combining these results with 2-D results, it is clear that ideal turbulence has, in most cases, a significant amount of 'coherent energy' (a statistically stationary nonzero value is significant

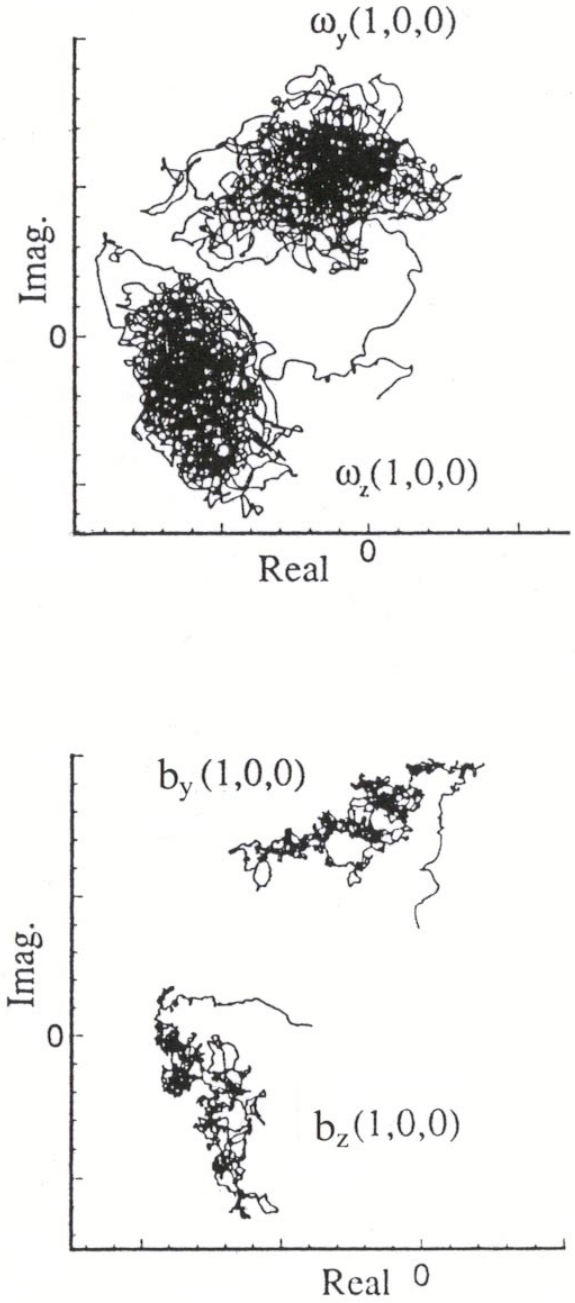

Figure 6.13: Run M1A: 3-D ideal MHD ($B_o = 0$), projection of the phase trajectory; top: real vs imaginary parts of $\tilde{\omega}_y(1,0,0)$ and $\tilde{\omega}_z(1,0,0)$; bottom: real vs imaginary parts of $\tilde{b}_y(1,0,0)$ and $\tilde{b}_z(1,0,0)$.

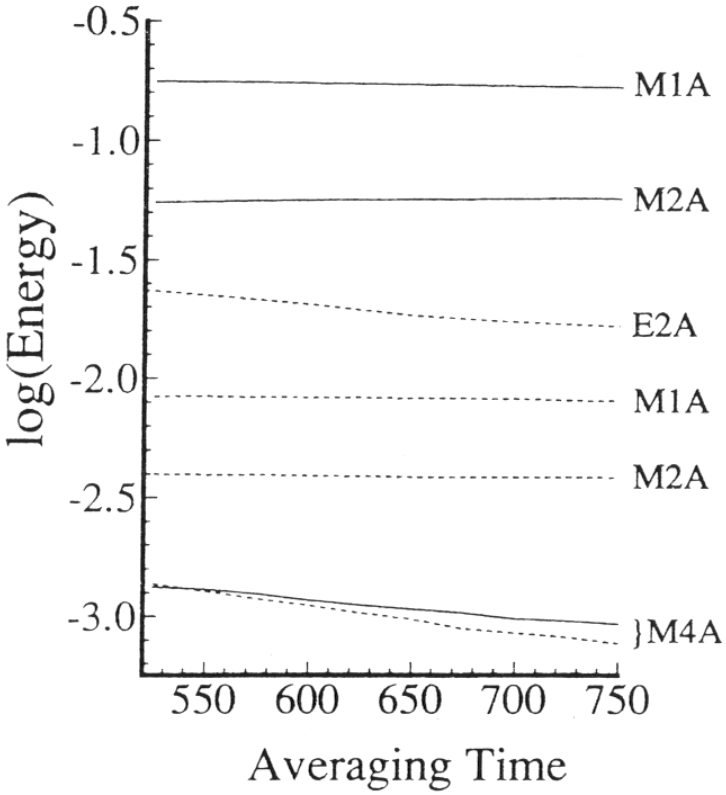

Figure 6.14: Coherent energies for four cases of 3-D ideal turbulence: E2A (Euler), M1A and M2A (MHD, $B_o = 0$), and M4A (MHD, $B_o = 1$); kinetic: dashed line; magnetic: solid line ($\log \equiv \log_{10}$).

because canonical ensemble theory predicts that the value is identically zero). In other words, there appear to be *coherent structures* present in ideal homogeneous turbulence. There is an apparent correlation between coherent energy and the absolute value of the other invariants in a given run. For example, as Table 6.2 shows, runs M1A and M2A share the same values of E and H_C, but different values of H_M. Run M1A has the higher value of H_M, and also more coherent energy, as Figure 6.14 shows.

Furthermore, although run M4A has the same values of E and H_C as runs M1A and M2A, it has essentially zero magnetic helicity H_M, as shown in Figure 6.11. It also has the lowest amount of coherent energy of the 3-D runs, as indicated by Figure 6.14. However, the coherent energy of run M4A can only be locked into the $k_x = 0$ coefficients, since all other coefficients can be thought of as combinations of nonlinear Alfvén waves, and their averages naturally tend to zero. (That 3-D run M4A is tending to a nonzero value of coherent energy is supported by Figure 6.6, in which the analogous 2-D run, CBK, clearly has reached a low, but nonzero stationary value of coherent energy.)

In all of these cases, 2-D and 3-D, the anomaly is not the run that has nonzero coherent energy, but rather the run that has (or is clearly headed toward) a value of zero. There is only one case in which canonical predictions and numerical averages appear equal and it is the 2-D Euler case, represented here by run NSP. In looking at Figure 6.6, we see that the value of coherent energy for run NSP is heading monotonically to zero. This reversal of expectations is the central and surprising result of the numerical work detailed in this chapter. The question then arises: Why are the canonical ensemble predictions not the same as the time averages for all cases of ideal turbulence, except for 2-D Euler turbulence? In other words, how does nonergodicity arise in ideal homogeneous turbulence?

The answer to this question is given in the next chapter.

6.5 References for Further Reading

The numerical results cited in this chapter are drawn from [Shebalin 82], [Shebalin 83], [Shebalin 89], and [Shebalin 94] (primarily from the latter two references). Independent work on ideal 3-D MHD turbulence was done by [Stribling 90], although the $B_o = 1$ case was not discussed and time averages were not taken.

A discussion of spectral methods is given in [Gottlieb 77], [Canuto 88], and [Boyd 01], while general discussions on numerical integration of differential equations can be found in many sources, including [Potter 73] and [Iserles 96].

Chapter 7

Broken Ergodicity

The statistical theory and computational study of ideal homogeneous turbulence has been laid out in the preceding chapters. The comparison of theoretical predictions with numerical results presented in the last chapter indicates that there is a significant mismatch between the two, which challenges the assumption of ergodicity implicit in the statistical theory. In the current chapter, we will see why this implicit assumption is generally incorrect. In what follows, we will demonstrate that ideal homogeneous turbulence is *non-ergodic*, except in the 2-D Euler case, and that this situation is caused by dynamically *broken symmetry*. Thus, ideal homogeneous turbulence has, inherent in its dynamics, a *broken ergodicity*.

7.1 Symmetry Under P, C, T

The classical symmetries are *parity*, or space reflection, P: $\mathbf{x} \to -\mathbf{x}$; *charge reversal* C: $q \to -q$; and *time reversal* T: $t \to -t$. (In addition, we can include the identity operation I.) The effect of P, C and T on $\mathbf{u}$, $\boldsymbol{\omega}$, $\mathbf{b}$ and $\mathbf{j}$, as well as on the helicities $H_K = (\mathbf{u}, \boldsymbol{\omega})/2$, $H_C = (\mathbf{u}, \mathbf{b})/2$ and $H_M = (\mathbf{a}, \mathbf{b})/2$, is given in Table 7.1. In Table 7.1, '$-$' or '$+$' signs indicate that the quantity in question does or does not, respectively, change sign under P, C, or T.

The energies $E_K = (\mathbf{u}, \mathbf{u})/2$ and $E_M = (\mathbf{b}, \mathbf{b})/2$, the enstrophy $\Omega = (\boldsymbol{\omega}, \boldsymbol{\omega})/2$, and the mean-squared magnetic potential $A = (\mathbf{a}, \mathbf{a})/2$ are all positive-definite quantities and thus unaffected by P, C, and T: E_K, E_M (and thus $E = E_K + E_M$), Ω, and A behave like scalars under P, C or T. Since it will be pertinent shortly, the inverse temperatures α associated with E in all cases of ideal turbulence are also scalars under P, C, or T, as can be seen in examining the relationships (5.10), (5.25) and (5.57). Similarly, examining (5.11) and (5.42) reveals that the inverse temperatures β – associated with Ω in the 2-D Euler case – and γ – associated with A in the 2-D ideal MHD case – are also scalars under the classical symmetry transformations.

The helicities, however, behave differently. As Table 7.1 shows, the helicities H_i ($i = K, C, M$) behave like *pseudoscalars* under P; H_C also transforms like a pseudoscalar under C. Thus the *helical invariants* H_K, H_C, and H_M of ideal homogeneous turbulence are

	I	P	C	T
$\mathbf{u}$	$+$	$-$	$+$	$-$
$\boldsymbol{\omega}$	$+$	$+$	$+$	$-$
$\mathbf{b}$	$+$	$+$	$-$	$-$
$\mathbf{j}$, $\mathbf{a}$	$+$	$-$	$-$	$-$
H_K	$+$	$-$	$+$	$+$
H_C	$+$	$-$	$-$	$+$
H_M	$+$	$-$	$+$	$+$

Table 7.1: Effect of the classical symmetry transformations P, C, and T on the signs of various quantities.

pseudoscalars under at least one of the classical symmetry transformations. If we look at the inverse temperatures associated with the various helical invariants, we see that they, too, are pseudoscalars:

$$\begin{aligned}
\underline{\text{3-D Euler}}\text{, eq. (5.26):} \qquad & \beta = -\frac{\mathcal{H}_K}{\Omega}\,\alpha \\
\underline{\text{2-D MHD}}\text{, eq. (5.41):} \qquad & \beta = -2\frac{\mathcal{H}_C}{\mathcal{E}_M}\,\alpha \\
\underline{\text{3-D MHD}}\text{, eq. (5.58):} \qquad & \beta = -2\frac{\mathcal{H}_C}{\mathcal{E}_M}\,\alpha \\
\text{eq. (5.59):} \qquad & \gamma = \frac{\mathcal{E} - 2\mathcal{E}_M}{\mathcal{H}_M}\,\alpha
\end{aligned} \tag{7.1}$$

The pseudoscalar nature of the inverse temperatures, on the left sides of the equations in (7.1), follows because, on the right sides, the inverse temperatures α (associated with total energy), as well as the energies and the enstrophy, are all scalars under P, C, or T, while the helicities are pseudoscalars. The net result is that βH_K, βH_C, and γH_M are all scalars. Thus, P, C, and T do not affect the canonical probability densities (4.30).

An equivalent statement is that, in forming an expectation value (see Section 4.7), all of phase space is averaged over, *i.e.*, regions of phase space associated with both signs of a given helicity are to be found in the domain of integration. This guarantees that the canonical ensemble theory of ideal homogeneous turbulence is invariant under the classical symmetries P, C, and T.

7.2 Broken Symmetry

It can readily be shown that P, C, and T do not affect the form of the evolution equations of ideal turbulence:

$$\begin{aligned} \frac{\partial \boldsymbol{\omega}}{\partial t} &= \nabla \times (\mathbf{u} \times \boldsymbol{\omega} + \mathbf{j} \times \mathbf{B}) \\ \frac{\partial \mathbf{B}}{\partial t} &= \nabla \times (\mathbf{u} \times \mathbf{B}) \,. \end{aligned} \tag{7.2}$$

Thus, the evolution equations (7.2) of ideal turbulence, as well as the canonical probability functions, are unaffected by P, C, or T.

However, this theoretical symmetry is not duplicated in any realization of ideal homogeneous turbulence containing a helical invariant. Once the system, as represented by a numerical model, is given an initial condition, it is also given a fixed sign of the corresponding helical invariant. The evolving system maintains the values of all associated invariants *and their signs* to within canonical fluctuations. The symmetry in the theory is not exhibited dynamically, and is thus called a *broken symmetry.*

In phase space, this broken symmetry is manifested in the presence of effectively *disjoint components.* Although canonical probability densities give finite probabilities to the appearance of the system point *anywhere* in phase space, if the invariant helicity has a magnitude large compared to canonical fluctuations, the probability that the system point will travel from a component with positive helicity to one with negative helicity is effectively zero. (In other words, the components are not *fuzzy* enough to have statistically significant overlap.)

In those cases of ideal homogeneous turbulence that possess a helical invariant, we can define a set-theoretic *characteristic function*, which indicates disjointness. Let $h_i = H_i/|H_i|$, $i = K, C, M$, for $H_i \neq 0$, and $h_i = 0$, $i = K, C, M$, for $H_i = 0$; then define

$$\begin{aligned} \chi_i^+ &= \frac{1}{2}\,(1 + h_i) \\ \chi_i^- &= \frac{1}{2}\,(1 - h_i). \end{aligned} \tag{7.3}$$

Thus, $\chi_i^+ = 1$ if the system point is on the positive helicity component and 0 if it is not. Similarly, $\chi_i^- = 1$ if the system point is on the negative helicity component and 0 if it is not. If $h_i = 0$, then $\chi_i^+ = \chi_i^+$, and in all cases we have $\chi_i^+ + \chi_i^+ = 1$.

For every invariant helicity $H_i \neq 0$, the characteristic functions (7.3) tell us that the disjointness of phase space increases by a factor of two. The number D of disjoint components is therefore $D = 2^N$, where N is the number of nonzero helical invariants present. The phase space structures of the different cases of ideal homogeneous turbulence are given in Table 7.2.

Table 7.2 now helps explain the high levels of coherent energy seen in Table 6.5 and Figure 6.14. The highest levels are in the 3-D ideal MHD runs, such as M1A and M2A, whose phase spaces have four disjoint components: M1A, in particular, has a stationary

Case	B_o	Invariants	D
2-D Euler	–	E, Ω	1
3-D Euler	–	E, H_K	2
2-D MHD	0	E, H_C, A	2
2-D MHD	1	E, H_C	2
3-D MHD	0	E, H_C, H_M	4
3-D MHD	1	E, H_C	2

Table 7.2: Phase space structure in ideal homogeneous turbulence ($H_i \neq 0$, $i = K, C, M$); D is the number of disjoint components.

coherent energy that is about 19% of the total energy, as indicated in Figure 6.14. Run M2A has a coherent energy that is about 6% of the total available energy, as also seen in Figure 6.14. In Table 6.2, we see that the major difference between the two runs is that M1A has a value of H_M that is more than twice that of run M2A. Although M1A and M2A have phase spaces with four disjoint components, the components in M1A may be thought of as being 'further apart.'

7.3 Coherent Structure

Classical ergodic theory ([Khinchin 49, pp. 19-38], [Sinai 94]) states that a statistical system is ergodic if and only if it its phase space does not consist of disjoint components (this is *Birkhoff's theorem*). In ideal homogeneous turbulence with helical invariants, phase space has, as we have just seen, either two or four disjoint components. Thus, ideal homogeneous turbulence with helical invariants is *nonergodic*. The symmetry of the governing theory, as we have also seen, is dynamically broken by the presence of helical invariants. The concepts of broken symmetry and nonergodicity are combined when ideal homogeneous turbulence with helical invariants is said to display *broken ergodicity*, a term first used by [Palmer 82].

When a system has broken ergodicity, there is an underlying structure of disjoint components in phase space. If the system point is allowed to range over all components (as it does in an ensemble prediction), then modal ensemble averages are, by construction, automatically zero. However, in a dynamical time-average, as found by numerical simulation, the system point can range over only one component, and modal time-averages are not required to be zero. This leads to nonzero coherent energy; combined with the otherwise chaotic behavior of the Fourier modes, this indicates that these modes are random variables with *nonzero means*. The structure in either k-space or x-space associated with these nonzero modal means may be thought of as a *coherent structure*.

Therefore, broken ergodicity is equivalent to coherent structure in ideal homogeneous turbulence with helical invariants.

7.4 References for Further Reading

A mathematical presentation of symmetry and invariance in nonlinear dynamical systems can be found in [Golubitsky 88].

Chapter 8

Epilog

The primary purpose of this work has been to present the statistical theory of ideal homogeneous turbulence. This has been done in the preceding chapters; the principal quantitative result found was that ideal turbulence with a helical invariant exhibits broken ergodicity. Thus, the assumption of ergodicity implicit in canonical ensemble theory is incorrect, and any predictions of this theory are only approximate. Full correctness could be restored if ensemble predictions were made by integrating only over those parts of phase space that had a definite sign to a given helical invariant. How to do this is not clear (it may not even be possible) because ensemble predictions are made at the level of a mode, and modal helicity appears unrestricted in sign, as opposed to the sum of all modal helicities, which has a fixed sign.

Nevertheless, the discovery of broken ergodicity, and its corollary, coherent structure, is the significant result in the theory of ideal homogeneous turbulence. The question arises: Is broken ergodicity manifested in real, homogeneous turbulence?

8.1 Ideal Versus Real

In ideal turbulence, there is no physically imposed length scale, so that numerical simulations on a relatively small number of grid points are sufficient, as long as there are enough modes to ensure statistical behavior. This is equivalent to stating that the ratio $\rho = k_{max}/k_{min}$ need only be moderate. If we take $k_{min} = 1$, then ensemble predictions of modal values can be renormalized so that any reference to explicit grid size disappears.

As an example, consider (4.40), the 2-D Euler prediction for modal vorticity. If we define $\hat{\mathbf{k}} = \mathbf{k}/k_{max}$, $\hat{\alpha} = \alpha/k_{max}$ and $\hat{\beta} = \beta$, the expectation value of modal vorticity can be rewritten as

$$\left\langle |\tilde{\omega}(\mathbf{k})|^2 \right\rangle = \frac{\hat{k}^2}{\hat{\alpha} + \hat{\beta}\hat{k}^2}. \tag{8.1}$$

All other modal ensemble predictions can be renormalized in the same way. The result is that we always have $0 < \hat{k} \leq 1$; increasing k_{max} only adds more points between 0 and 1, but

does not change the shape of the curve (8.1).

In real homogeneous turbulence, the situation is completely different, because the dissipation coefficients ν and η (viscosity and resistivity, respectively) set the size of the smallest length-scales. Consider Navier-Stokes turbulence (Euler turbulence with a 'switched-on' viscosity, $\nu > 0$). If it is stationary and dissipative, there is a balance between energy input at the largest scales and dissipated at the smallest scales; as is customary, let us call the energy being dissipated per unit density and unit time ε. If there is no energy input, then the turbulence merely decays from some initial state, and $\varepsilon = |dE/dt|$. As is well known, there is a *dissipation wave number* $k_D \sim (\varepsilon/\nu^3)^{1/4}$; since $|dE/dt| = 2\nu\Omega = \varepsilon$, as (3.75) shows, then $k_D \sim (\Omega/\nu^2)^{1/4}$. It was shown in [Kolmogorov 41] that, for low viscosity, at length scales intermediate to the largest and the smallest scales of a flow, the energy spectra integrated over direction in k-space was $E(k) \sim \varepsilon^{2/3} k^{-5/3}$. Although many physical experiments have borne this law out, none of the energy spectra for ideal homogeneous turbulence is commensurate with it.

8.2 Real Simulations

In any simulation of real, homogeneous turbulence, care must be taken that $k_{max} \simeq k_D$; this effectively sets the size of ν. In general, the smaller ν is, the larger k_D is, but for a realistic simulation k_D cannot be larger than about $N/2$, the largest value of k along any coordinate axis. Therefore, in order to reduce dissipation as much as possible in a realistic simulation, the grid size must be made as large as practical. However, computers are finite machines and at any given time, there is always a limit on the number of grid points N along a coordinate axis.

Currently 3-D simulations with $N = 2^{10} \cong 10^3$ or 2-D simulations with $N = 2^{15} \cong 3 \times 10^3$ are possible. These require long run times and in the 3-D case only achieve a moderate value of dissipation wave number, $k_D \approx 2^9 = 512$. In the 2-D case, however, we have $k_D \approx 2^{14} = 16,384$. Matching k_D with k_{max} in any simulation is done by trying a value of ν, running the code for a short time and seeing what Ω and ε are, then adjusting ν and rerunning, etc., for a few iterations, until ν is set so that $k_{max} \simeq k_D$. Many simulations of real turbulence have been done and we will not attempt to review them all here, particularly since they give no evidence as to ergodicity or nonergodicity.

However, let us mention the one set of preliminary numerical results we know of that is pertinent to the search for broken ergodicity in real homogeneous turbulence. These results come from a set of runs that followed the 2-D ideal turbulence simulations presented earlier. The initial conditions of the 2-D ideal runs CAI and CBK, which were detailed in Chapter 6, were used to initiate the dissipative runs CAID and CBKD, respectively. The runs CAID and CBKD had the same grid and time step sizes as CAI and CBK, but the viscosity ν and resistivity η were 'switched on' and the terms $-\nu k^2 \tilde{\omega}(\mathbf{k})$ in (3.44) and $-\eta k^2 \tilde{a}(\mathbf{k})$ in (3.45) were retained in the simulations. (We used $\nu = \eta = 0.01$.)

The numerical procedure was extended by treating the dissipative terms implicitly: once

the iterations in (6.6) and (6.7) were performed, an additional operation was done:

$$\begin{aligned} (1+\mu k^2\Delta t)^{-1}\bar{u}_{n+1}(\mathbf{k}) &\rightarrow \bar{u}_{n+1}(\mathbf{k}) \\ (1+\mu k^2\Delta t)^{-1}\tilde{u}_{n+1}(\mathbf{k}) &\rightarrow \tilde{u}_{n+1}(\mathbf{k}). \end{aligned} \tag{8.2}$$

Here, μ is either ν or η, as appropriate.

The dissipative simulations CAID and CBKD were run for 200 simulation times each, and the maximum Kolmogorov dissipation wave number k_D (for a short time during the beginning of each run) peaked at between 26 and 46. The energy fell rapidly, as it was dissipated at the higher wave numbers. However, an examination of the evolution of the lowest wave number coefficients $\tilde{\omega}(0,1)$, $\tilde{\omega}(1,0)$, $\tilde{a}(0,1)$ and $\tilde{a}(1,0)$ with respect to time shows some very interesting behavior. In Figure 8.1, the evolution of $\tilde{\omega}(0,1)$ and $\tilde{\omega}(1,0)$ for run CAID is shown (compare this with Figure 6.7 for run CAI). In Figure 8.2, the evolution of $\tilde{a}(0,1)$ and $\tilde{a}(1,0)$ for run CAID is shown (compare this with Figure 6.8 for run CAI). In Figure 8.3, the evolution of $\tilde{\omega}(0,1)$ and $\tilde{\omega}(1,0)$ for run CBKD is shown (compare this with Figure 6.9 for run CBK). In Figure 8.4, the evolution of $\tilde{a}(0,1)$ and $\tilde{a}(1,0)$ for run CBKD is shown (compare this with Figure 6.10 for run CBK).

In general, the range of the values of $\tilde{\omega}(0,1)$, $\tilde{\omega}(1,0)$, $\tilde{a}(0,1)$ and $\tilde{a}(1,0)$ in Figures 8.1, 8.2, 8.3 and 8.4 are about one half the range for the same coefficients in Figures 6.7, 6.8, 6.9 and 6.10 (see [Shebalin 89] for more detail). Qualitatively, the figures indicate that, except for the Alfvén wave behavior of $\tilde{\omega}(1,0)$ and $\tilde{a}(1,0)$ shown in Figures 8.3 and 8.4, the phase trajectories of these 2-D simulations of real homogeneous appear nonergodic. However, the dissipation coefficients are relatively large and the appearance of nonergodicity is suggestive, rather than conclusive.

8.3 Some Future Directions

Although 2-D Navier-Stokes turbulence contains no ideal helical invariants, 2-D MHD does, and it should prove very interesting if a realistic 2-D MHD simulation similar to the simulation of [Matthaeus 91], 'Decaying, two-dimensional, Navier-Stokes turbulence at very long times,' produced some interesting results in 2-D real turbulence. This work followed 2-D Navier-Stokes turbulence, simulated for a relatively long time – over several hundred 'eddy turnover times' – on a 512^2 grid with a maximum $k_D \cong 230$. The initial flow was small-scale and highly chaotic, and the novel result was that only two large vortices of opposite sign remained at the end of the simulation.

In the simulation of [Matthaeus 91], relaxation to a large-scale coherent structure was observed. In the case of 2-D MHD, the existence of an ideal helical invariant may or may not have an effect on the outcome – this is an open question. At the least, running on a large grid size (with smaller values of ν and η) would shed some more light on the apparent nonergodicity in real homogeneous MHD turbulence seen in Figures 8.1, 8.2, 8.3 and 8.4 (produced

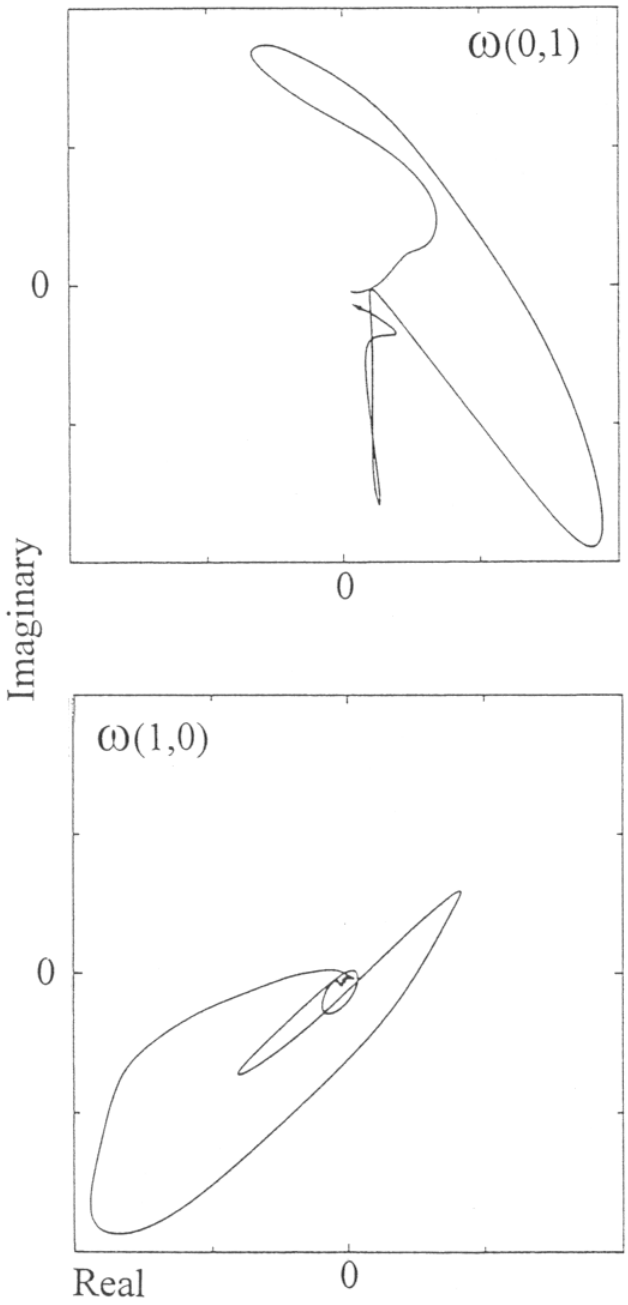

Figure 8.1: Run CAID: 2-D real MHD ($B_o = 0$), projection of phase trajectory; top: $\tilde{\omega}_R(0,1)$ vs $\tilde{\omega}_I(0,1)$, bottom: $\tilde{\omega}_R(1,0)$ vs $\tilde{\omega}_I(1,0)$.

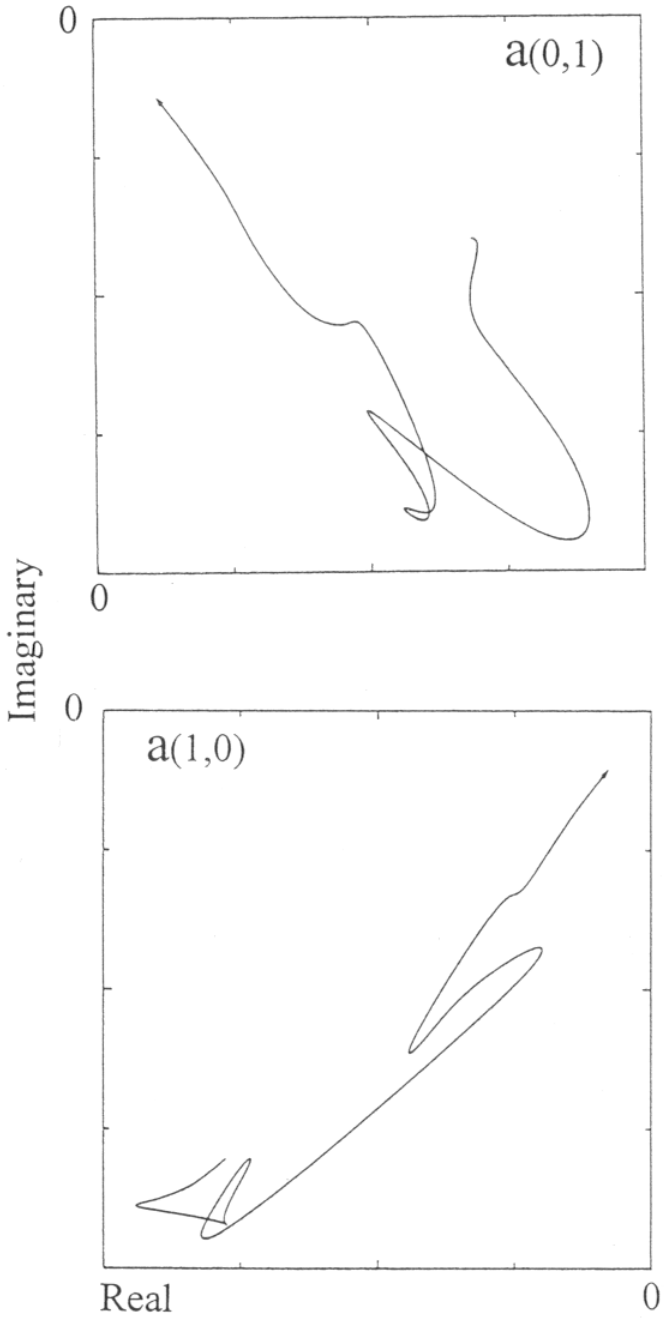

Figure 8.2: Run CAID: 2-D real MHD ($B_o = 0$), projection of phase trajectory; top: $\tilde{a}_R(0,1)$ vs $\tilde{a}_I(0,1)$, bottom: $\tilde{a}_R(1,0)$ vs $\tilde{a}_I(1,0)$.

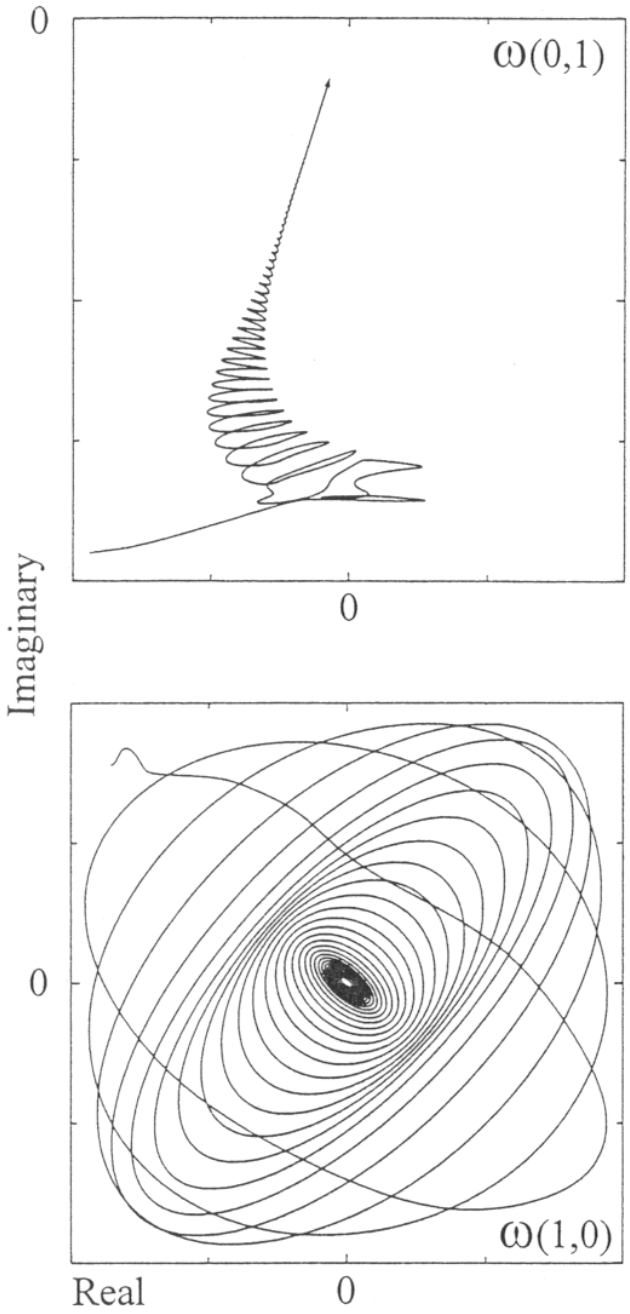

Figure 8.3: Run CBKD: 2-D real MHD ($B_o = 1$), projection of the phase trajectory; top: $\tilde{\omega}_R(0,1)$ vs $\tilde{\omega}_I(0,1)$, bottom: $\tilde{\omega}_R(1,0)$ vs $\tilde{\omega}_I(1,0)$.

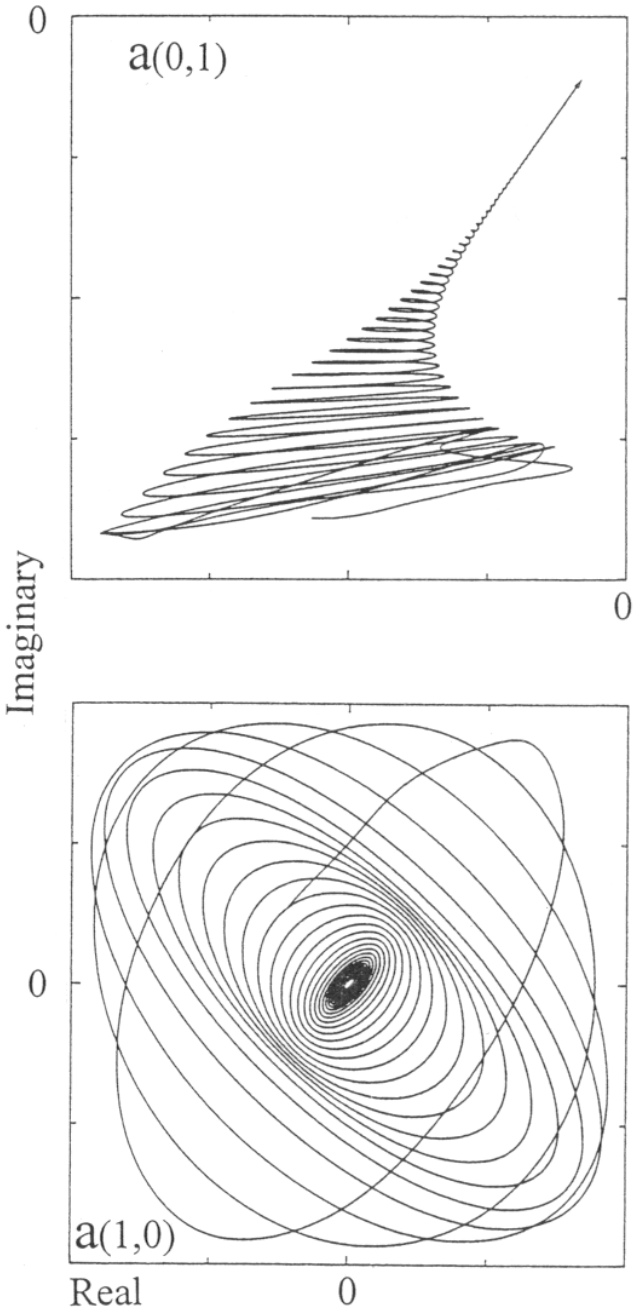

Figure 8.4: Run CBKD: 2-D real MHD ($B_o = 1$), projection of the phase trajectory; top: $\tilde{a}_R(0,1)$ vs $\tilde{a}_I(0,1)$, bottom: $\tilde{a}_R(1,0)$ vs $\tilde{a}_I(1,0)$.

by relatively large values of ν and η). A 2-D real MHD simulation is also interesting for another reason: 3-D Navier-Stokes has an ideal helical invariant, while 2-D Navier-Stokes does not; since 2-D MHD turbulence possesses helical invariants, 3-D Navier-Stokes turbulence is closer, in this sense, to the 2-D real MHD case than to the 2-D Navier-Stokes case.

Another direction for future investigation begins with the Navier-Stokes modal equations (3.15) with $\mathbf{B} \equiv \mathbf{0}$:

$$\frac{d\,\tilde{\boldsymbol{\omega}}(\mathbf{k})}{dt} \;=\; \tilde{\mathbf{S}}(\tilde{\mathbf{u}}, \tilde{\boldsymbol{\omega}}; \mathbf{k}) - \nu k^2 \tilde{\boldsymbol{\omega}}(\mathbf{k}). \tag{8.3}$$

In this equation, replace $\tilde{\mathbf{u}}(\mathbf{k})$ and $\tilde{\boldsymbol{\omega}}(\mathbf{k})$ with

$$\tilde{\mathbf{v}}(\mathbf{k}) = e^{\nu k^2 t}\, \tilde{\mathbf{u}}(\mathbf{k}), \qquad \tilde{\mathbf{w}}(\mathbf{k}) = e^{\nu k^2 t}\, \tilde{\boldsymbol{\omega}}(\mathbf{k}). \tag{8.4}$$

The result is

$$\frac{d\,\tilde{\mathbf{w}}(\mathbf{k})}{dt} \;=\; \hat{\mathbf{S}}(\tilde{\mathbf{v}}, \tilde{\mathbf{w}}; \mathbf{k}). \tag{8.5}$$

Here, the nonlinear term denoted by $\hat{\mathbf{S}}$ is the vector convolution:

$$\hat{\mathbf{S}}(\tilde{\mathbf{v}}, \tilde{\mathbf{w}}; \mathbf{k}) \;\equiv\; i\mathbf{k} \times \sum_{\substack{\mathbf{p}+\mathbf{q}=\mathbf{k} \\ \mathbf{k},\,\mathbf{p},\,\mathbf{q} \in \mathcal{S}}} \left[e^{-2i\nu \mathbf{p}\cdot\mathbf{q}\, t}\, \tilde{\mathbf{v}}(\mathbf{p}) \times \tilde{\mathbf{w}}(\mathbf{q}) \right]. \tag{8.6}$$

The nonlinear term would look like the one for Euler flow, except for the presence of the factor $\exp(-2i\nu \mathbf{p}\cdot\mathbf{q}\, t)$ within the summation (8.6). It can easily be seen that (8.5) satisfies a Liouville equation because $\partial \hat{\mathbf{S}}(\mathbf{k}) / \partial \tilde{\mathbf{v}}(\mathbf{k}) = 0$. However, it is an open question as to whether (8.5) possesses any invariants; if it did, then a canonical theory could be built for Navier-Stokes turbulence, just as one was built for Euler turbulence. (This would be a first step toward a theory of real MHD turbulence.)

8.4 Summary

Geometrically, an ideal invariant defines a hypersurface in phase space; the intersection of these hypersurfaces contains those regions in phase space where the phase point will be found (to within statistical fluctuations). In the presence of helical invariants, the regions of intersection are disjoint – each region corresponds to one sign of the helicity (as we have seen, canonical ensemble theory is invariant with respect to the sign of a helical invariant, and so integrates over both to produce an ensemble average). Again, this is the cause of nonergodicity: disjoint components in phase space (Birkhoff's theorem). The ensemble average thus does not match the time average (as the numerical results examined in Chapter 6 show).

If dissipation is turned on, these hypersurfaces start collapsing; the smaller the viscosity and resistivity, the slower the collapse. However, the speed of the collapse is higher at larger

magnitudes of the wave number k. If a simulation can be done with the largest k_{max} and k_D possible, then presumably the collapse will be the slowest possible. If, during this collapse, the components in phase space are able to maintain their disjointness fairly well, then the phase point may be effectively stuck on the component where it started, even if it has enough time, dynamically speaking, to have moved a considerable distance in phase space.

The manifestation of nonergodicity lies in significantly nonzero average values for the Fourier coefficients. (Significant can be defined as a large ratio between the absolute value of the average and the standard deviation of a Fourier mode.) Thus, rather than seeing Fourier mode values exhibiting a sequence of decreasing oscillations through zero, they may oscillate about some nonzero value which is itself slowly decreasing to zero. Hints of this have been seen in 2-D real MHD simulations on small grid sizes (32^2) [Shebalin 89]. It should prove interesting to run some large grid size/low dissipation numerical experiments in 2-D real MHD homogeneous turbulence.

8.5 Conclusion

The major portion of this work has been to describe the statistical mechanics and thermodynamics of ideal homogeneous turbulence. Furthermore, this was restricted to the incompressible flow of fluids and magnetofluids; *i.e.*, Euler and ideal MHD turbulence. Numerical experiments exposed what the canonical theory had hidden: a broken ergodicity. Although the governing equations are symmetric under the classical symmetry transformations, this symmetry must be dynamically broken, because a system whose motion conserves helicity with a positive sign cannot also conserve it with a negative sign, and vice versa. Furthermore, a few preliminary 2-D dissipative MHD runs have suggested that nonergodicity may also be a factor in real homogeneous turbulence.

Ideal homogeneous turbulence serves as a model system for real turbulence, where, however, dissipation is critical. The model is somewhat remote from reality, however, since ideal ensemble predictions produce a spectrum that is qualitatively different from that of the Kolmogorov $k^{-5/3}$ spectrum [Kolmogorov 41], a spectrum which has been verified in physical experiments. Nevertheless, by teaching us that some models of turbulence contain broken ergodicity and coherent structure, perhaps ideal homogeneous turbulence has taught us something that will ultimately be useful in our attempt to understand real turbulence, as well as other nonlinear physical systems.

8.6 References for Further Reading

The text [Landau 87, pp. 129-135] discusses the Kolmogorov theory (as well as other classical and modern results in turbulence theory).

Bibliography

[Arfken 00] G. B. Arfken & H. J. Weber, *Mathematical Methods for Physicists*, 5th Ed., Academic Press, New York, 2000.

[Batchelor 53] G. K. Batchelor, *The Theory of Homogeneous Turbulence*, Cambridge U. P., Cambridge, UK, 1953.

[Betchov 61] R. Betchov, *Phys. Fluids* **4**, 925 (1961).

[Boyd 01] J. P. Boyd, *Chebyshev and Fourier Spectral Methods*, 2nd Ed., Dover, Mineola, NY, 2001.

[Bracewell 86] R. N Bracewell, *The Fourier Transform and its Applications*, 2nd Ed., McGraw-Hill, New York, 1986.

[Canuto 88] C. Canuto, M. Y. Hussaini, A. Quateroni, & T. A. Zang, *Spectral Methods in Fluid Dynamics*, Springer-Verlag, New York, 1988.

[Carnevale 81] G. F. Carnevale, U. Frisch, & R. Salmon, *J. Phys. A: Math. Gen.* **14**, 1701 (1981).

[Carnevale 82] G. F. Carnevale, *J. Fluid Mech.* **122**, 143 (1982).

[Elsässer 56] W. M. Elsässer, *Rev. Mod. Phys.* **28**, 135 (1956).

[Ferraro 61] V. C. A. Ferraro & C. Plumpton, *An Introduction to Magneto-Fluid Mechanics*, Oxford U. P., London, 1961.

[Frisch 75] U. Frisch, A. Pouquet, J. Leorat, & A. Mazure, *J. Fluid Mech.* **68**, 769 (1975).

[Frisch 95] Uriel Frisch, *Turbulence*, Cambridge U. P., Cambridge, UK, 1995.

[Gadzag 76] J. Gadzag, *J. Comp. Phys.* **20**, 196 (1976).

[Golubitsky 88] M. Golubitsky, I. Stewart, & D. G. Schaeffer, *Singularities and Groups in Bifurcation Theory, Vol. II*, Springer-Verlag, New York, 1988.

[Gottlieb 77] D. Gottlieb & S. A. Orszag, *Numerical Analysis of Spectral Methods: Theory and Applications*, SIAM, Philadelphia, 1977.

[Fyfe 76] D. Fyfe & D. Montgomery, *J. Plasma Phys.* **16**, 181 (1976).

[Hamming 86] R. W. Hamming, *Numerical Methods for Scientists and Engineers*, Dover, New York, 1986.

[Iserles 96] A. Iserles, *A First Course in the Numerical Analysis of Differential Equations*, Cambridge U. P., Cambridge, UK, 1996.

[Jackson 75] J. D. Jackson, *Classical Electrodynamics*, 2nd Ed., pp. 17-22, Wiley, New York, 1975.

[Khinchin 49] A. I. Khinchin, *Mathematical Foundations of Statistical Mechanics*, pp. 137-145, Dover, New York, 1949.

[Kolmogorov 41] A. N. Kolmogorov, *Dokl. Akad. Nauk SSSR* **30**, 9 (1941).

[Kraichnan 73] R. H. Kraichnan, *J. Fluid Mech.* **59**, 745 (1973).

[Kraichnan 75] R. H. Kraichnan, *J. Fluid Mech.* **67**, 155 (1975).

[Kraichnan 80] R. H. Kraichnan & D. Montgomery, *Rep. Prog. Phys.* **43**, 547 (1980).

[Landau 80] L. D. Landau & E. M. Lifshitz, *Statistical Physics*, 3rd Ed., Pergamon, New York, 1980.

[Landau 84] L. D. Landau & E. M. Lifshitz, *Electrodynamics of Continuous Media*, 2nd Ed., Pergamon, New York, 1984.

[Landau 87] L. D. Landau & E. M. Lifshitz, *Fluid Mechanics*, 2nd Ed., Pergamon, New York, 1987.

[Lee 52] T. D. Lee, *Q. Appl. Math.* **10**, 69 (1952).

[Matthaeus 91] W. H. Matthaeus, W. T. Stribling, D. Martinez, S. Oughton, & D. Montgomery, *Physica D* **51**, 531 (1991).

[McComb 95] W. D. McComb, *The Physics of Fluid Turbulence*, Clarendon Press, Oxford, UK, 1995.

[Moffatt 69] H. K. Moffatt, *J. Fluid Mech.* **35**, 117 (1969).

[Montgomery 76] D. Montgomery, *Phys. Fluids* **19**, 802 (1976).

[Nicholson 83] D. R. Nicholson, *Introduction to Plasma Theory*, John Wiley, New York, 1983.

[Orszag 72] S. A. Orszag & G. S. Patterson *Phys. Rev. Lett.* **28**, 76 (1972).

[Palmer 82] R. G. Palmer, *Adv. Phys.* **31**, 669 (1982).

[Patterson 71] G. S. Patterson & S. A. Orszag, *Phys. Fluids* **14**, 2538 (1971).

[Potter 73] D. Potter, *Computational Physics*, pp. 34-36, Wiley, New York, 1973.

[Shebalin 82] J. V. Shebalin, *Anisotropy in MHD turbulence due to a mean magnetic field*, Ph.D. Dissertation, College of William and Mary (1982).

[Shebalin 83] J. V. Shebalin, W. H. Matthaeus, & D. Montgomery, *J. Plasma Phys.* **29**, 525 (1983).

[Shebalin 89] J. V. Shebalin, *Physica D* **37**, 173 (1989).

[Shebalin 94] J. V. Shebalin, *Phys. Plasmas* **1**, 541 (1994).

[Shebalin 96] J. V. Shebalin, *J. Plasma Phys.* **56**, 541 (1996).

[Shebalin 98] J. V. Shebalin, *Phys. Lett. A* **250**, 319 (1998).

[Sinai 94] Ya. G. Sinai, *Topics in Ergodic Theory*, p. 19, Princeton U. P., Princeton, 1994.

[Stribling 90] T. Stribling & W. H. Matthaeus, *Phys. Fluids B* **2**, 1979 (1990).

[Verhulst 96] F. F. Verhulst, *Nonlinear differential equations and dynamical systems*, 2nd Ed, Springer-Verlag, New York, 1996.

[Woltjer 58] L. Woltjer, *Proc. Nat. Acad. Sci. USA* **44**, 833 (1958).

Index

REPORT DOCUMENTATION PAGE

Form Approved
OMB No. 0704-0188

1. AGENCY USE ONLY *(Leave Blank)*	2. REPORT DATE	3. REPORT TYPE AND DATES COVERED
	May 2002	NASA Technical Paper

4. TITLE AND SUBTITLE
The Statistical Mechanics of Ideal Homogeneous Turbulence

5. FUNDING NUMBERS

6. AUTHOR(S)
John V. Shebalin

7. PERFORMING ORGANIZATION NAME(S) AND ADDRESS(ES)

Lyndon B. Johnson Space Center
Houston, Texas 77058

8. PERFORMING ORGANIZATION REPORT NUMBERS
S-893

9. SPONSORING/MONITORING AGENCY NAME(S) AND ADDRESS(ES)

National Aeronautics and Space Administration
Washington, DC 20546-0001

10. SPONSORING/MONITORING AGENCY REPORT NUMBER
TP-2002-210783

11. SUPPLEMENTARY NOTES

12a. DISTRIBUTION/AVAILABILITY STATEMENT

Available from the NASA Center for AeroSpace Information (CASI)
7121 Standard
Hanover, MD 21076-1320 Subject Category: 75

12b. DISTRIBUTION CODE

13. ABSTRACT *(Maximum 200 words)*

Plasmas, such as those found in the space environment or in plasma confinement devices, are often modeled as electrically conducting fluids. When fluids and plasmas are energetically stirred, regions of highly nonlinear, chaotic behavior known as turbulence arise. Understanding the fundamental nature of turbulence is a long-standing theoretical challenge.

The present work describes a statistical theory concerning a certain class of nonlinear, finite dimensional, dynamical models of turbulence. These models arise when the partial differential equations describing incompressible, ideal (i.e., non-dissipative) homogeneous fluid and magnetofluid (i.e., plasma) turbulence are Fourier transformed into a very large set of ordinary differential equations. These equations define a divergenceless flow in a high-dimensional phase space, which allows for the existence of a Liouville theorem, guaranteeing a distribution function based on constants of the motion (integral invariants). The novelty of these particular dynamical systems is that there are integral invariants other than the energy, and that some of these invariants behave like pseudoscalars under two of the discrete symmetry transformations of physics, parity and charge conjugation.

In this work the "rugged invariants" of ideal homogeneous turbulence are shown to be the only significant scalar and pseudoscalar invariants. The discovery that pseudoscalar invariants cause symmetries of the original equations to be dynamically broken and induce a nonergodic structure on the associated phase space is the primary result presented here. Applicability of this result to dissipative turbulence is also discussed.

14. SUBJECT TERMS	15. NUMBER OF PAGES	16. PRICE CODE
plasma control; magnetohydrodynamics; plasma turbulence; plasmas (physics); Fourier transformation; Liouville theorem; pseudoscalars; ergodic process	145	

17. SECURITY CLASSIFICATION OF REPORT	18. SECURITY CLASSIFICATION OF THIS PAGE	19. SECURITY CLASSIFICATION OF ABSTRACT	20. LIMITATION OF ABSTRACT
Unclassified	Unclassified	Unclassified	Unlimited